Photoinhibition superresolution lithography

by

Darren Lawrence Forman

B.S., University of New Mexico, 2004

A thesis submitted to the

Faculty of the Graduate School of the

University of Colorado in partial fulfillment

of the requirements for the degree of

Doctor of Philosophy

Department of Electrical, Computer and Energy Engineering

2014

This thesis entitled:
Photoinhibition superresolution lithography
written by Darren Lawrence Forman
has been approved for the Department of Electrical, Computer and Energy Engineering

Robert McLeod

Sean Shaheen

Date _____

The final copy of this thesis has been examined by the signatories, and we find that both the content and the form meet acceptable presentation standards of scholarly work in the above mentioned discipline.

Forman, Darren Lawrence (Ph.D., Electrical Engineering)

Photoinhibition superresolution lithography

Thesis directed by Prof. Robert McLeod

While the prospect of nanoscale manufacturing has generated tremendous excitement, arbitrary patterning at nanometer length scales cannot be brought about with current photolithography – the technology that for decades has driven electronics miniaturization and enabled mass production of digital logic, memory, MEMS and flat-panel displays. This is due to the relatively long wavelength of light and diffraction, which imposes a physical not technological limit on the resolution of a far-field optical pattern. Photoinhibited superresolution (PInSR) lithography is a new scheme designed to beat the diffraction limit through two-color confinement of photopolymerization and, via efficient single-photon absorption kinetics, also be high-throughput capable.

This thesis describes development of an integrated optical and materials system for investigating spatiotemporal dynamics of photoinhibited superresolution lithography, with a demonstrated 3× superresolution beyond the diffraction limit. The two-color response, arising from orthogonal photogeneration of species that participate in competing reactions, is shown to be highly complex. This is both a direct and indirect consequence of mobility. Interesting trade-offs arise: thin-film resins (necessitated by single-photon absorption kinetics) require high viscosity for film stability, but the photoinhibition effect is suppressed in viscous resins. Despite this apparent suppression, which can be overcome with high excitation of the photoinhibition system, the low mobility afforded by viscous materials is beneficial for confinement of active species. Diffusion-induced blurring of patterned photoinhibition is problematic in a resin with viscosity η = 1,000 cP, and overcome in a resin with viscosity η = 500,000 cP. Superresolution of factor 3x beyond the diffraction limit is demonstrated at 0.2 NA, with additional results indicating superresolution ability at 1.2 NA.

Investigating the effect of diminished photoinhibition efficacy with increased resin viscosity, analysis shows that it is an inevitable side-effect of reduction of the diffusion-limited termination rate constant. Further analysis confirms the experimental result that the viscosity effect may be overcome, with photogeneration of a large concentration of inhibiting radicals. Elevated radical concentration is also shown to be necessary for reducing diffusion-lengths, owing to the bimolecular nature of radical termination. The quantitative kinetics of photoinitiation, photoinhibition and chain polymerization are individually developed, validated and finally incorporated into a unified model. Finally, taking into account the complex, highly-coupled nature of PInSR requirements and operation, an alternate superresolution scheme is presented. In particular, the scheme is aimed at achieving deep-subwavelength superresolution with a single monochromatic source and multiple exposures. It utilizes a surface-tethered photochemistry that requires no films or gas-management, and essentially eliminates diffusion of active species. Preliminary, single-exposure results are shown.

For my family.

Acknowledgements

This work was made possible by generous funding from these sources:

- DOD-NDSEG and NSF-IGERT Fellowships to the author
- NSF-CAREER Award #0954202 to Prof. McLeod
- Oracle Corp. gift to the University of Colorado

In addition, I would like to acknowledge Kim Urness and Tim Scott for their substantial contributions to this project, and thank several others for their help and interest: past and present members of the McLeod and Bowman research groups, Mark Watson (Oracle), Thomas Lynn, Bob Cormack, the CNL team, Michael Cole and Prof. Chris Bowman. Finally, I would like to thank Prof. Bob McLeod for his endless enthusiasm, ideas and support throughout this effort.

Contents

Chapter

Figures

Figure

Chapter 1

Introduction

In a 1959 lecture that has since become the foundational myth of nanotechnology [69, 219], Richard Feynman challenged his fellow physicists to go small. In that talk, he proposed feats of what must have seemed like outlandish miniaturization: heart surgery performed by tiny remote-controlled manipulators, a face-recognition computer built from submicron transistors, the 24-volume Encyclopaedia Britannica written on the head of a pin and molecular synthesis performed not in solution, but by physically placing atoms one next to the other.

Fifty-five years later we have the benefit of undergoing laparoscopic heart surgery, and our own faces can be recognized by the phones we carry in our pockets. Our digitized tax-returns and photos are stored on cheap magnetic media, with bit domain spacing nearing the cited 25,000× reduction from the half-tone dot on a printed page. And with the advent of the scanning tunneling microscope (STM), it is possible to position single atoms on a substrate. But unlike these other wonders, the spatial manipulation of individual atoms and molecules has not had a direct impact much beyond the condensed-matter research community. This is arguably due not to a lack of applications, but to a lack of scalability.

Devices, small or large, can change the way we live only to the degree that they are economical to make. Despite decades of advancements with STM and its cousin the atomic-force microscope (AFM), probe-based instruments able to image and manipulate on the atomic scale remain slow and delicate. Electron-beam and ion-beam lithography can

address features more quickly, but only marginally so.

Working at somewhat coarser resolutions, semiconductor manufacturers are able to sell chips with millions and billions of tiny transistors because device unit-cost is extremely small - thanks to huge economies of scale. The high price-tag of precision tools used for circuit patterning is offset by tremendous throughput, enabled by projection lithography. Optical patterning has been the technology of choice for high volume chip making not just due to the excellent resolution and low distortion possible across wide fields with well-designed projection lenses, but also because of the sensitivity and high fidelity of the photoresists.

Projected light can only be focused so tightly, however, and it turns out that at the shortest deep-ultraviolet wavelengths (where generation, propagation and refraction is difficult but still manageable), light can be focused to ∼40 nm spots and no smaller; this represents the finest pattern dimension possible at production scale with so-called top-down manufacturing. But even this limit can only be reached at production volumes by advanced chip manufacturers, whose capital-equipment costs have forced consolidation on a global scale. For non-IC manufacturing and many research labs, the ∼0.5 μm pattern resolution achieved with contact and laser-direct-write lithography is more typical.

Nanoimprint lithography (NIL) is a technology developed to address the shortcomings of optical and e-beam lithography: the blurring effects of diffraction and diffusion are avoided by using a surface-relief template to mechanically "stamp" patterns onto a substrate. In the arena of next-generation lithography, NIL has the advantage of simplicity. Apart from template wear-and-tear, the main production challenges are in overlay alignment and defect reduction – typical of any patterning technology. More significant, perhaps, are the challenges in high-resolution patterning of the template itself. Unlike photolithographic masks which are significantly demagnified by the projection lens, NIL templates must be fabricated at 1:1 scaling. As pattern resolution approaches 10 nm and below, the required e-beam and focused ion-beam (FIB) writing processes become very slow.

Bottom-up molecular synthesis, by contrast, takes advantage of specific chemical re-

actions to achieve structuring at dimensions ranging from a 0.5 nm crystal lattice constant to the 5 nm radius-of-gyration of a folded protein. While synthetic chemists regularly manipulate materials at molecular scales, their control does not typically extend beyond the dimensions of large molecules. Directed self-assembly, which I will address later, combines the so-called top-down and bottom-up approaches with the use of macromolecular materials that spontaneously form sublithographic patterns on conventionally-patterned templates. The benefits of DSA, however, are limited to applications involving fine periodic structures. More arbitrary and complex self-assembled patterns are possible with nascent techniques such as DNA-origami, although it is unclear whether they will be suitable for manufacturing.

So, in the so-called mesoscale (roughly 5 - 500 nm) where features are longer than typical large molecules but shorter than the wavelength of light, arbitrary dense patterning remains demanding and often impractical. It seems, therefore, that a significant opportunity now exists for new approaches. This thesis describes a technique called photoinhibited super-resolution lithography, which combines optics and materials science to address the challenge of high-throughput patterning at scales finer than traditionally allowed by diffraction.

Chapter 2

Optical lithography, the diffraction limit and throughput

Optical lithography has many potential and realized applications in fine patterning. This chapter provides a brief overview of current technology and its variations. Specific configurations and applications for conventional patterning are mentioned, with discussion of throughput and resolution performance. The Abbe diffraction limit is introduced, which sets the fundamental resolution that can be achieved with conventional optical patterning technologies. Inspired by STED microscopy, several strategies – including the topic of this thesis – have recently emerged to break the diffraction limit. The various feature-size reduction mechanisms are discussed, along with inherent trade-offs affecting resolution and throughput.

2.1 Photolithographic technology

Precision optical patterning may be broadly classified into two categories: parallel and serial. Serial technologies include direct laser write (DLW), electron beam and optical near-field writing. In DLW lithography, a laser beam is focused and scanned to write a computer-defined pattern into a photosensitive material. For large-area, planar applications such as the manufacturing of flat-panel displays, DLW tools expose substrates coated with photoresist to focused laser beams operating in the violet or ultraviolet. The patterned optical exposure forms a latent image in the resist. Pattern transfer is completed when the resist is developed and the exposed (positive-tone) or unexposed (negative-tone) resist is

removed. Absorption is single-photon, so the process can be relatively fast and there is no intensity threshold effect.

In contrast, two-photon-polymerization (TPP) lithography uses a suppressed response to out-of-focus light to write tiny 3D patterns of crosslinked polymer into a single droplet of resin. A post-exposure solvent rinse clears away unexposed resin, leaving a physical 3D structure attached to the substrate. The main challenge in these systems is two-photon absorption cross-section, which is several order of magnitude smaller than single-photon absorption. Although great strides have been made (see [54], for example), the typical $\sim$TW$\cdot$cm^{-2} excitation intensities required by TPP can only be met by focusing a laser beam, often from an ultrafast Ti:sapphire oscillator, to a single scanning spot. This results in slow writing speeds, limiting applications to research in materials, optics and electromagnetics.

Probe-based techniques such as near-field scanning (NSOM) lithography can be used for optical patterning with 20 nm resolution [167]. The diffraction limit does not apply because near-field evanescent coupling is used. To do this, an optical fiber is coated with metal except for a $\sim$100 nm hole at the tip. The probe is then lowered onto a light-sensitive surface, which is scanned in synchronization with modulated light from the subwavelength aperture. While NSOM is scientifically valuable for microscopy, frequent breakage of probe tips and inherently slow scanning over large areas limits its usefulness for patterning.

Although not strictly an optical technique, electron beam (e-beam) lithography achieves fine patterning by combining optical microscopy principles with the extremely small de Broglie wavelength of accelerated electrons. Despite slow write speeds and reliability problems, as well as so-called proximity effect limitations at nanometer scales, e-beam patterning is a powerful technology with broad research applications in physics, chemistry, materials and engineering.

Parallel (or area) optical patterning technology mostly consists of contact and projection lithography. In typical contact lithography, a resist-coated surface is placed against a (typically chrome) mask with opaque and transparent regions. Flood exposing through the

mask selectively exposes the transparent regions, and a latent image is formed in the resist. The advantage of contact lithography is simplicity; only uniform UV illumination is needed. But the requirement of mechanical contact to avoid large diffraction effect means that the mask is inevitably damaged, defects accumulating with each use. Scaling is also difficult, both for the problem of rapidly bringing the mask in and away from contact with the sample and for the problem of exposing multiple areas on a large substrate. Projection lithography was developed to address these issues, and is now used for virtually all logic and memory manufacturing.

Projection lithography is at the heart of chip manufacturing, and has been the primary driver for the observed exponential scaling in transistor count since the advent of the integrated circuit. In ongoing efforts to improve the minimum patterned feature size, or critical dimension (CD) that is set by the Abbe diffraction limit $CD = k_1\lambda \ / \ NA$, lithographers have been steadily reducing wavelength (λ), increasing numerical aperture (NA) and eliminating aberrations and other factors detrimental to resolution (k_1). Projection scanners are built around the most sophisticated lenses in the world (see Fig. 2.1), and have burdensome price-tags with single-tool costs comparable to 0.5% of total factory cost[1] .

Since reaching the fundamental resolution limits of deep ultraviolet immersion lithography in the latter part of the last decade, massive efforts have been made to extend projection patterning into the extreme ultraviolet (EUV). However, formidable challenges in source brightness and reliability, reflective optics for 13.5 nm (100 eV) and resist stability in high vacuum, to name a few, have translated into extreme cost and limited performance, so far thwarting use in a production environment. While disappointing, the lack of a clear path forward also provides an opportunity to explore new approaches.

Despite the alternatives available during the last half-century of microelectronics manufacturing, optical lithography has been the patterning technology of choice. While this preference is somewhat self-reinforcing after significant market penetration has occurred,

[1] based on US$45M ASML TwinScan 193i, US$10B Foundry [113] (2006 figures)

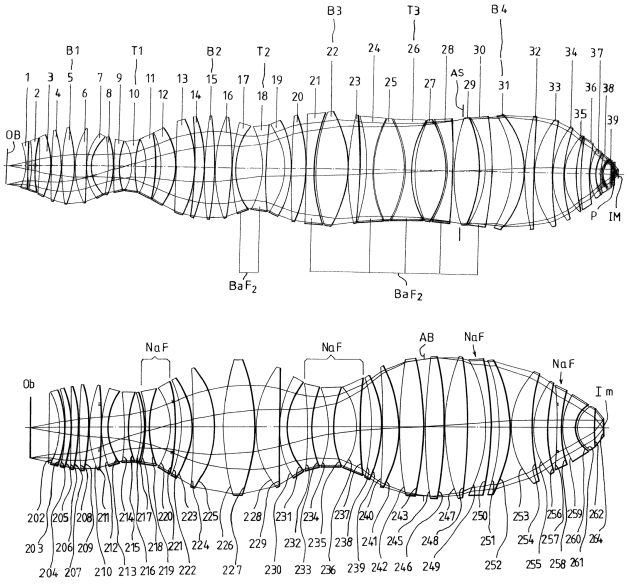

Figure 2.1: Zeiss patent: projection lens for deep ultraviolet lithography [200].

sustained popularity suggests inherently superior technological advantages. Photons are exceptionally clean and well-behaved: they do not charge or diffuse, cannot become contaminated, and will typically only cause damage at very high fluences given the appropriate materials. Scattering and diffraction present a challenge, as we shall see, but the combination of excimer laser technology and advanced electromagnetic theory with centuries of refinement in glass, optical design and photochemistry has yielded unparalleled capability in pattern-transfer fidelity and throughput.

2.2 The diffraction limit to resolution

Diffraction is resolution-limiting for all the above techniques apart from e-beam, which is instead typically diffusion-limited. As pointed-out by Abbe more than a century ago, the best resolution achieved by a good optical microscope is subject to limits that are not technological, but physical. Specifically, Abbe showed that an optical microscope could not

possibly resolve features spaced more closely than

$$d = \frac{\lambda_0}{2n\sin\theta} = \frac{\lambda_0}{2(NA)}, \tag{2.1}$$

where θ is the angular extent of the clear aperture.

We may re-derive this limit by analyzing wave interference. As shown in Fig. 2.2, two plane waves propagating along vectors $\mathbf{k_1}$ and $\mathbf{k_2}$ interfere at an angle 2θ to produce a fringe pattern with period Λ. The plane wave vector magnitudes are equal and scaled by wavelength, such that

$$|\mathbf{k_1}| = |\mathbf{k_2}| = \frac{2\pi}{\lambda}, \tag{2.2}$$

and using basic trigonometry we see that

$$\sin\theta = \frac{\pi/\Lambda}{|\mathbf{k_1}|}. \tag{2.3}$$

Refractive index is accounted for by

$$\lambda = \frac{\lambda_0}{n}, \tag{2.4}$$

which can be substituted into Eq. 2.1 and rearranged to give the familiar Abbe resolution limit

$$d = \Lambda = \frac{\lambda}{(2n\sin\theta)}. \tag{2.5}$$

Fourier-pair uncertainty analysis is another, less common approach to the diffraction limit that can be adapted to a variety of optical designs. Here I will review the method used by Grill and Stelzer [92] and compare the results with the Abbe limit. To begin, probabilistic moment

$$m_{n,j} = \int_{-\pi}^{\pi} [p_j(\alpha)]^n D_p(\alpha) d\alpha \wedge j \in \{x, y, z\}, \tag{2.6}$$

where D_p is the aperture function and p_j is the momentum component along a given vector direction j. The standard deviation of the angular distribution of momenta may be calculated from moments $n = 0, 1, 2$ with

$$\Delta p_j = \left[\frac{m_{2,j}}{m_{0,j}} - \left(\frac{m_{1,j}}{m_{0,j}}\right)^2\right]^{1/2} \wedge j \in \{x, y, z\}. \tag{2.7}$$

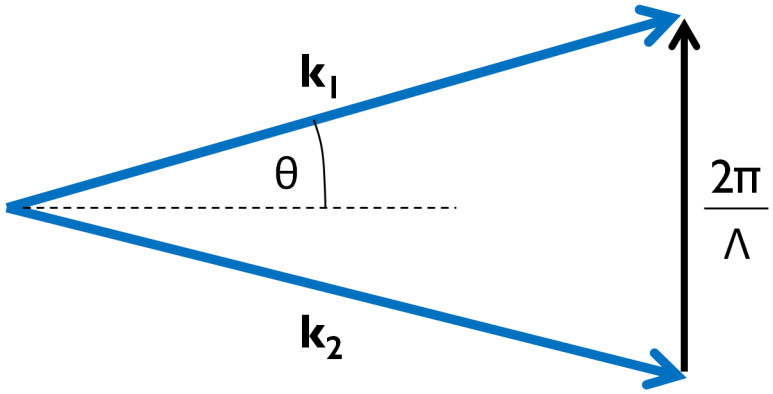

Figure 2.2: Plane waves defined by $\mathbf{k_1}$ and $\mathbf{k_2}$ interfere to generate fringes with period Λ. In an optical microscope with a clear aperture extending from the optical axis to θ, the Abbe resolution limit $\mathrm{d} = \Lambda$.

Using the uncertainty-principle inequality

$$\Delta p_j \Delta j \geq \frac{\hbar}{2} \wedge j \in \{x, y, z\}, \tag{2.8}$$

the spatial standard deviation of photon impingement is

$$\Delta j \geq \frac{\hbar}{2\left[\dfrac{m_{2,j}}{m_{0,j}} - \left(\dfrac{m_{1,j}}{m_{0,j}}\right)^2\right]^{1/2}} \wedge j \in \{x, y, z\}. \tag{2.9}$$

For comparison to the interference of two plane-waves, I will evaluate Δj for the two-dimensional case of a converging cylindrical wave. Angular momentum components are then

$$p_x = |\mathbf{p}| \sin\alpha, \;\; p_z = |\mathbf{p}| \cos\alpha. \tag{2.10}$$

An arbitrary binary aperture function D_p is chosen to mask the converging wave and evaluate the width of the resulting focused spot. As shown in Fig. 2.3, a double-slit aperture with a central obscuration can provide illumination similar to the case of interfering plane waves. The aperture function is

$$D_\mathrm{p}^\mathrm{DS}(\alpha) = H(\alpha + \alpha_\mathrm{max}) - H(\alpha - \alpha_\mathrm{max}) - H(\alpha + \epsilon\alpha_\mathrm{max}) - H(\alpha - \epsilon\alpha_\mathrm{max}), \tag{2.11}$$

where $\alpha_{\max}$ is the outer extent of the aperture, ϵ is the central obscuration parameter and H is the Heaviside step-function. With $D_{\mathrm{p}} = D_{\mathrm{p}}^{\mathrm{DS}}$, Eq. 2.8 has the minimum value

$$\Delta x_{DS,2D} = \frac{[(1-\epsilon)\alpha_{\max}]^{1/2}\lambda}{2\pi[2\alpha_{\max}(1-\epsilon) - \sin 2\alpha_{\max} + \sin 2\epsilon\alpha_{\max}]^{1/2}}. \tag{2.12}$$

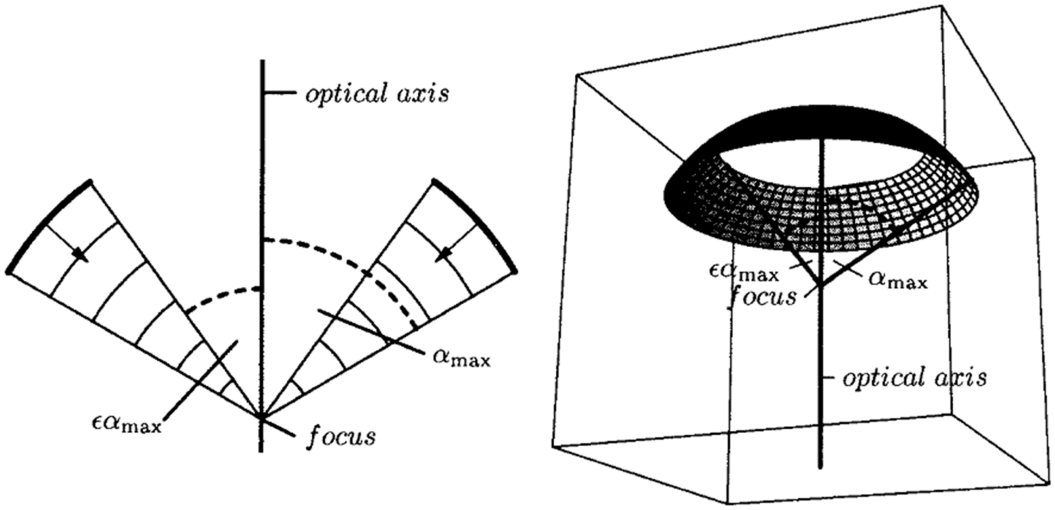

Figure 2.3: From [92]. On the left, a two dimensional double-slit aperture with outer angular extent $\alpha_{\max}$ and central obscuration parameter ϵ. On the right, the same configuration in three dimensions (annular-illumination).

To compare the limits given by Eq. 2.1 and 2.12, one must be able to convert between different threshold-level definitions. Since the minimum spot size in Eq. 2.12 is given in terms of standard deviation, I will attempt to find the standard deviation of a single fringe period generated by interfering plane waves. A unit-amplitude sinusoid centered on the origin, representing the normalized electric field amplitude from interfering plane waves, is given by

$$U(x) = \frac{1}{2}(\cos x + 1), \tag{2.13}$$

with intensity (or photon flux) given by

$$I(x) = U^2(x). \tag{2.14}$$

Integrating over a single period,

$$\int_{-\pi}^{\pi} I(x)dx = 2.356, \tag{2.15}$$

so the normalized probability density function (PDF) $I'(x)$ for photon impingement within that period is

$$I'(x) = \frac{I(x)}{2.356}. \tag{2.16}$$

Variance of a PDF f(x) is

$$\sigma^2 = \int_a^b (x-\mu)^2 f(x)dx, \tag{2.17}$$

where μ is the mean, so with $\mu = 0$

$$\sigma^2 = \int_{-\pi}^{\pi} x^2 I'(x)dx \approx 0.7899 \tag{2.18}$$

and

$$\sigma \approx 0.889. \tag{2.19}$$

The full-pitch of a fringe period is π, so relating resolution (d) to half-pitch (CD) to standard deviation ($\Delta j = \sigma$),

$$\frac{d}{2} = CD \approx \frac{\pi}{0.889}\Delta j. \tag{2.20}$$

Figure 2.4 compares Eq. 2.1 and 2.12 ($\epsilon = 0.99$), evaluated in terms of numerical aperture (NA). The somewhat ($\sim$13%) wider focal spot predicted by Eq. 2.12 is unexpected, but may be related to the curvature of the cylindrical waves.

The focal spot generated by a three-dimensional, converging spherical wave may also be calculated using Grill and Stelzer's method. Moments are redefined in spherical coordinates, so that

$$m_{n,j} = \int_0^{2\pi}\int_0^{\pi} [p_j(\alpha,\phi)]^n D_p(\alpha,\phi) \times \sin\alpha \; d\alpha d\phi \wedge j \in \{x,y,z\}. \tag{2.21}$$

$$p_x = |\mathbf{p}|\sin\alpha\cos\phi, \;\; p_z = |\mathbf{p}|\cos\alpha. \tag{2.22}$$

For a circular clear aperture, the angular distribution of momenta is ϕ-invariant and defined by

$$D_p^{cc}(\alpha,\phi) = H(\alpha) - H(\alpha - \alpha_{max}). \tag{2.23}$$

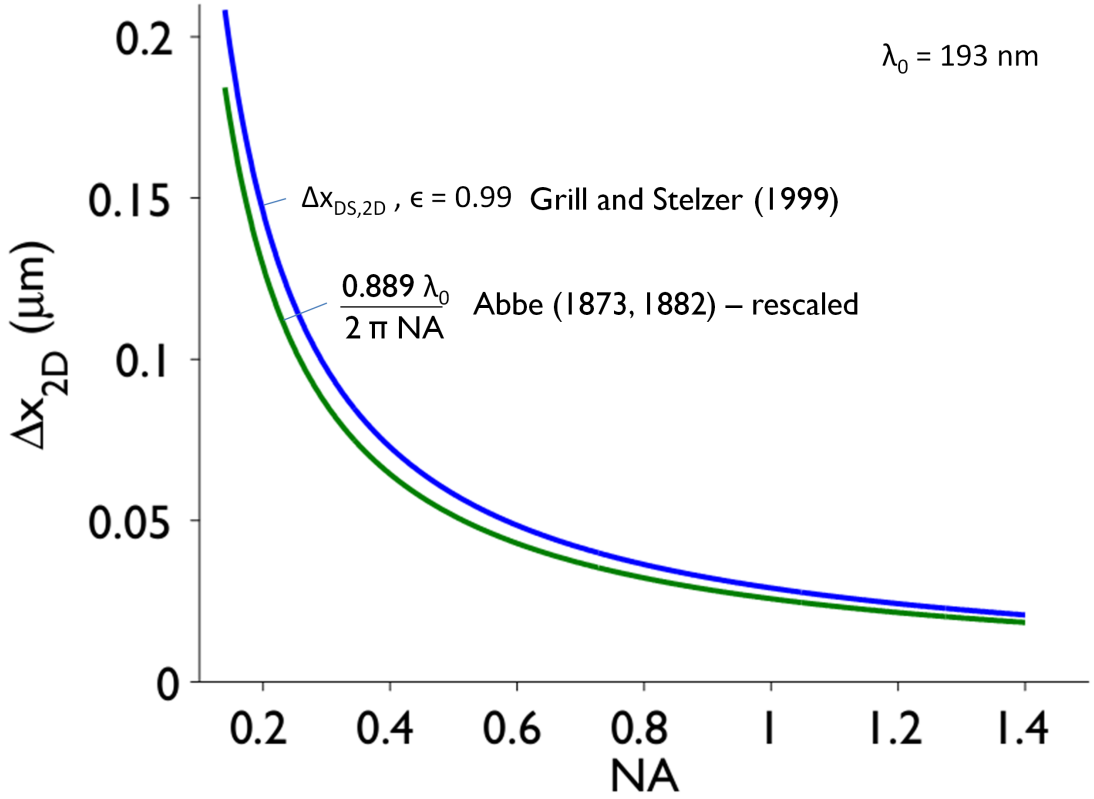

Figure 2.4: Evaluation and comparison of two approaches to the diffraction limit. Equation 2.5 (Abbe limit, green) is scaled by 2.20 and Eq. 2.12 (position uncertainty through a double slit aperture, blue) is unscaled.

The minimum standard deviation of intensity is then

$$\Delta x_{CC} = \frac{\sqrt{3}\lambda}{2\pi(3 - 2\cos\theta - \cos 2\theta)^{1/2}}. \tag{2.24}$$

2.3 Resolution enhancement techniques

Due to the light contribution from near the optical axis, masking the central part of the converging wavefront with an annular aperture (see Fig. 2.3, right) can improve spot width. As with the others, this aperture can be defined with a binary aperture function

$$D_{\mathrm{p}}^{\mathrm{AA}}(\alpha, \phi) = H(\alpha - \epsilon\alpha_{\max}) - H(\alpha - \alpha_{\max}). \tag{2.25}$$

With Eq. 2.21, 2.22 and 2.25, the minimum from 2.8 evaluates to

$$\Delta x_{AA} = \frac{\sqrt{3}\lambda}{2\pi[4 - \cos 2\alpha_{\max} - \cos 2\epsilon\alpha_{\max} - \cos(\alpha_{\max} - \epsilon\alpha_{\max}) - \cos(\alpha_{max} + \epsilon\alpha_{max})]^{1/2}}. \tag{2.26}$$

In Fig. 2.5, minimum clear aperture standard deviation is compared against annular apertures with moderate and high obscuration parameters ϵ. For converging waves that do not exceed 2π steradians, increased ϵ improves the minimum spot size. If, in practice, the obscuration is opaque, improved resolution may need to be balanced against reduced efficiency and throughput.

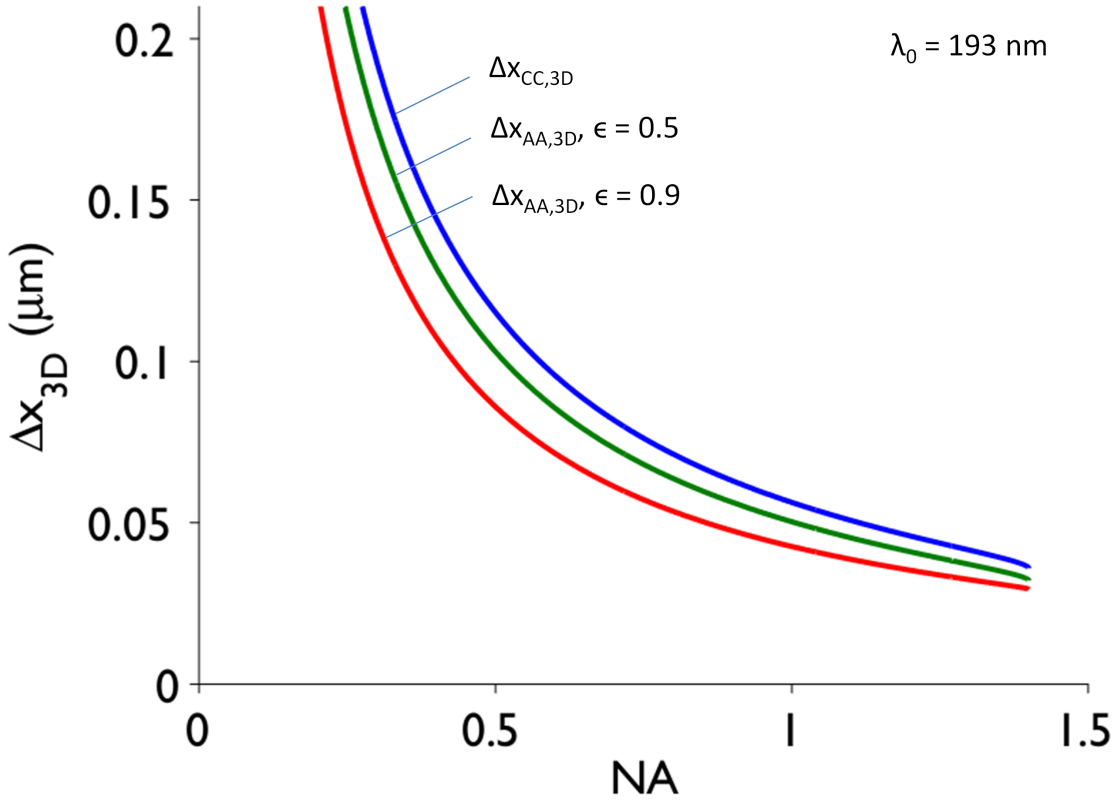

Figure 2.5: Spot width comparison with clear and annular apertures. Increasing the central obscuration of an annular aperture can improve spot width, at the potential cost of efficiency and throughput. Resolution enhancement technologies (RET) such as annular apertures can improve resolution up to, but not beyond, the Abbe limit.

Other off-axis illumination schemes are used as well, especially the dipole and quadrupole

configurations. These are chosen in conjunction with the particular spatial frequencies in the image to be projected. For example, horizontally-oriented dipole illumination is used for improving the resolution and contrast of vertical but not horizontal lines, and quadrupole illumination is used for improving rectangular but not circular features.

The term superresolution is sometimes misapplied. Measurements of small features alone cannot be taken as resolution, and improvements against some arbitrary baseline are not necessarily superresolved. By taking advantage of non-linearities in resist development, for example, isolated trenches and holes can be readily formed with dimensions tighter than the bright fringes and spots of the optical exposure. But with relatively large spaces between the features, resolution (and information content) remains unenhanced.

In dense patterning, diffraction effects can negatively impact image fidelity above the strict diffraction limit. Well-defined line-elbows and rectangle corners in the object-plane become highly distorted in the image plane. To address this problem, optical proximity correction (OPC) techniques seek to pre-compensate for diffraction effects in the mask design. In order to obtain a rectangle at the image plane, the corresponding mask feature in the object plane is flared at the ends and narrowed in the middle. Contrast improvement can be achieved with phase-shift masks that reverse electric field amplitude just after the object plane, obtaining darker nulls between the intensity features in the image plane. While these methods are sometimes advertised as enabling superresolution [3], they are more accurately described as resolution enhancement techniques (RET). That is, they improve resolution in a real and practical way, but only to the fundamental limit.

In semiconductor manufacturing, *CD* sets a lower bound on both the size of individual electronic devices and how densely they can be packed. A process parameter k_1 is a lumped term describing the net effects of aberrations and processing non-idealities. As processes and technologies mature, lower values of k_1 can be achieved thus enabling tighter critical dimensions. The fundamental lower limit is 0.25, as discussed above, but is more comfortably

0.4 in a manufacturing environment. As written in the lithography literature:

$$CD = k_1 \frac{\lambda}{NA} \tag{2.27}$$

Despite the planar nature of semiconductor lithography, inverse-square scaling of depth-of-focus (DOF) with NA can place an extreme demand on axial positioning and require restricted surface topography. Because of this, depth-of-focus can be as important as CD or more so at high NA. Another process parameter, k_2, is used to scale it:

$$DOF = k_2 \frac{\lambda}{NA^2} \tag{2.28}$$

Since the terminal resolution of ArF excimer ($\lambda = 193$ nm), NA=1.3 immersion lithography was reached in leading-edge processes, with $CD = 38$ nm, further improvements in pattern density have been achieved with multiple exposure and multiple patterning. Many variations exist, but the basic concept is to create non-linearities through processing that cannot be achieved with available linear optics. Dual tone resists crosslink with high exposure dose and are chemically insoluble with zero dose; only intermediate doses cause resist removal in developer. This provides the benefit of pitch-doubling with a single exposure.

Double or multiple exposure processes involve exposing the same photoresist film to different patterns, often originating from different masks, in sequence. This can be used with off-axis illumination configurations that are optimized for high resolution in a certain lateral direction. By breaking-up the exposure this way, it is possible to obtain optimized contrast at high resolution in $\hat{x}$ and $\hat{y}$ simultaneously. But without dual-tone or other non-linear behavior, the fundamental resolution limit is not improved.

Double or multiple patterning, on the other hand, can improve fundamental resolution. Instead of mere multiple exposures, the entire lithographic process is repeated for the same process step. For example, isolated narrow trenches are obtained in negative-tone resist with extended exposure. The resist is then be developed and the underlying layer etched for permanent transfer of the narrow trenches. Upon resist removal, the substrate is coated

with resist again and the entire process repeated with fine overlay alignment to achieve a second set of trenches interleaved with the first. Spacers may also be used to multiply pattern density, used alone or in conjunction with multiple patterning. To make spacers, a conformal coating is applied to pre-patterned features with vertical or near-vertical sidewalls. Etching removes the thin portions of the film on top of mesas or in-between features, leaving pillars on each sidewall. The pre-patterned feature is then selectively removed, leaving behind only the pillars which have twice the spacing density of the original support feature. While effective for extending miniaturization to the extent that resist development contrast is high and photoacid diffusion is low, these technologies incur a direct cost against throughput.

Directed self-assembly (DSA), on the other hand, imposes only limited throughput costs and is one of the most promising technologies for extending optical lithography. There are multiple DSA variations, with one particular process shown in Fig. 2.6. The basic concept is to pattern a template with conventional optical lithography, apply a block-copolymer film, and anneal it to produce ordered binary polymer domains aligned with the template. Upon selective removal of one of the domains, a density-multiplied polymer stencil remains. For applications such as memory and bit-patterned media (BPM), functional structures are often periodic and could greatly benefit from an efficient line or dot-multiplying DSA process. But while periodic-pattern density is increased, information density is not. That is, current DSA technology produces a template of narrow and tightly-spaced parallel lines across large areas. Additional, high-resolution “cut” or “trim” patterning is required to fabricate useful devices or vias from the template.

2.4 Superresolution

Lithography and microscopy are closely related, as each is approximately the other operating in reverse. In recent years, stimulated emission-depletion (STED) microscopy has demonstrated superresolved imaging of dense features, in real-time in the far-field. Briefly, STED is an extension of confocal microscopy. In addition to the excitation laser beam,

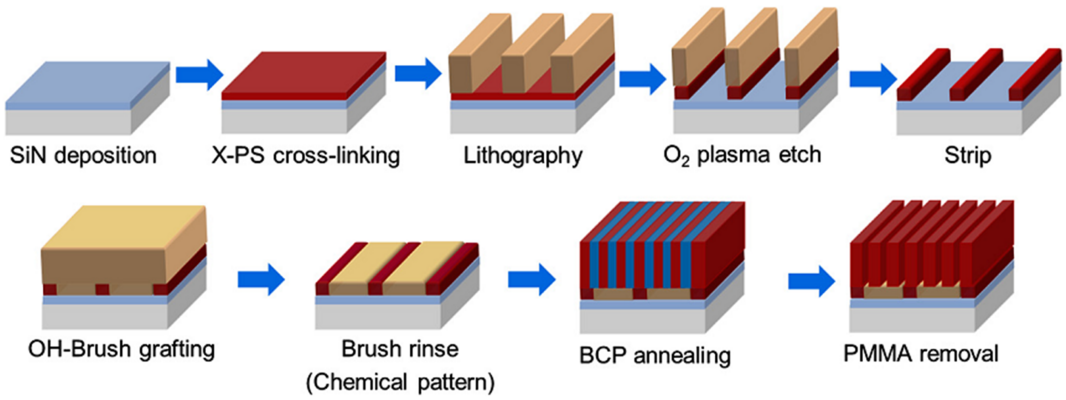

Figure 2.6: From [61]. Schematic overview of the UW chemo-epitaxy process flow.

a second laser beam, with a wavelength chosen to preemptively eliminate fluorescence by draining the excited-state population, is formed into a dark-centered Gauss-Laguerre donut and focused around the excitation spot. As the power of the de-excitation beam is increased, confinement of the fluorescing region is enhanced. Superresolved imaging is performed by scanning the co-aligned spots across a sample while collecting the fluorescent emission in a photomultiplier tube, and reconstructing the signal map as a function of scan position. Resolution is typically improved 2-3x, but an especially impressive 5 nm resolution has been achieved with visible light in the special case of imaging nitrogen-vacancies in diamond [194].

Even more recently, STED microscopy has inspired new approaches to lithography. Menon and coworkers [7] reported on a bilayer technique for 2-color superresolution, consisting of a photochromic film laminated on top of a conventional resist film. When the stack is illuminated by red light, an azobenzene-derived species in the upper film undergoes a ring-opening reconfiguration, causing increased absorbance in certain portions of the UV spectrum. Acting as a dynamic near-field mask, the red-patterned photochromic film can limit the spatial extent of transmitted UV light to shrink features. Since the photoisomerization is to some extent reversible, the process can be repeated to achieve superresolved features.

This technique has the advantage of completely decoupling the 2-color response by

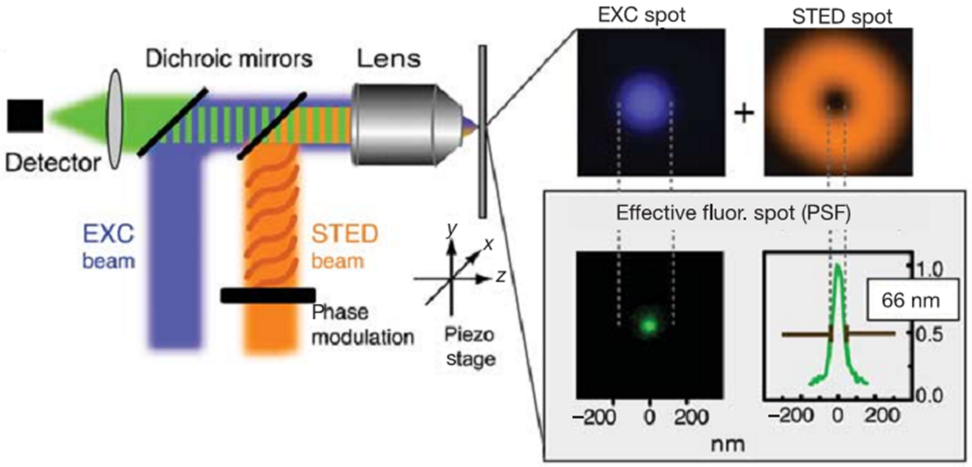

Figure 2.7: From [235]. Stimulated emission-depletion (STED) is a superresolution variant of confocal microscopy, where a Gauss-Laguerre spot induces non-linear de-excitation at the confocal spot periphery to narrow the fluorescence emission point-spread-function (PSF). STED provided the inspiration for multiple superresolution lithography schemes, including the one examined in this thesis.

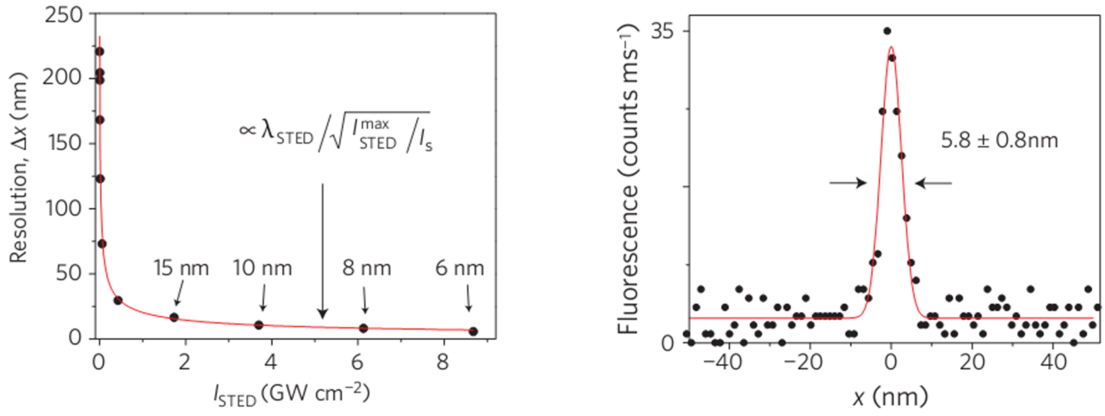

Figure 2.8: From [194]. STED imaging of nitrogen-vacancy (NV) centers in diamond, with PSF width $\sim \lambda/130$. This dramatic result may be enabled by the all-physical (not chemical) mechanism of NV fluorescence and fluorescence-deactivation with STED.

physical separation, allowing a more engineered system design. It also refrains from consuming species, which is an important feature for the multiple activation / deactivation cycles required for dense, superresolved patterning. The main challenges are absorption contrast

and cycle times. Even with high loadings of photoswitchable chromophores with $\Delta\varepsilon \approx 10^4$ where ε is molar absorptivity, submicron films still have absorption modulation depths of only order 5x, leading to incomplete suppression of feature edges. Switchable absorption cycle times, on the other hand, are greatly relevant to throughput. While the UV-driven open $\rightarrow$ close isomerization is measured in seconds to minutes, red-driven close $\rightarrow$ open is measured in hours.

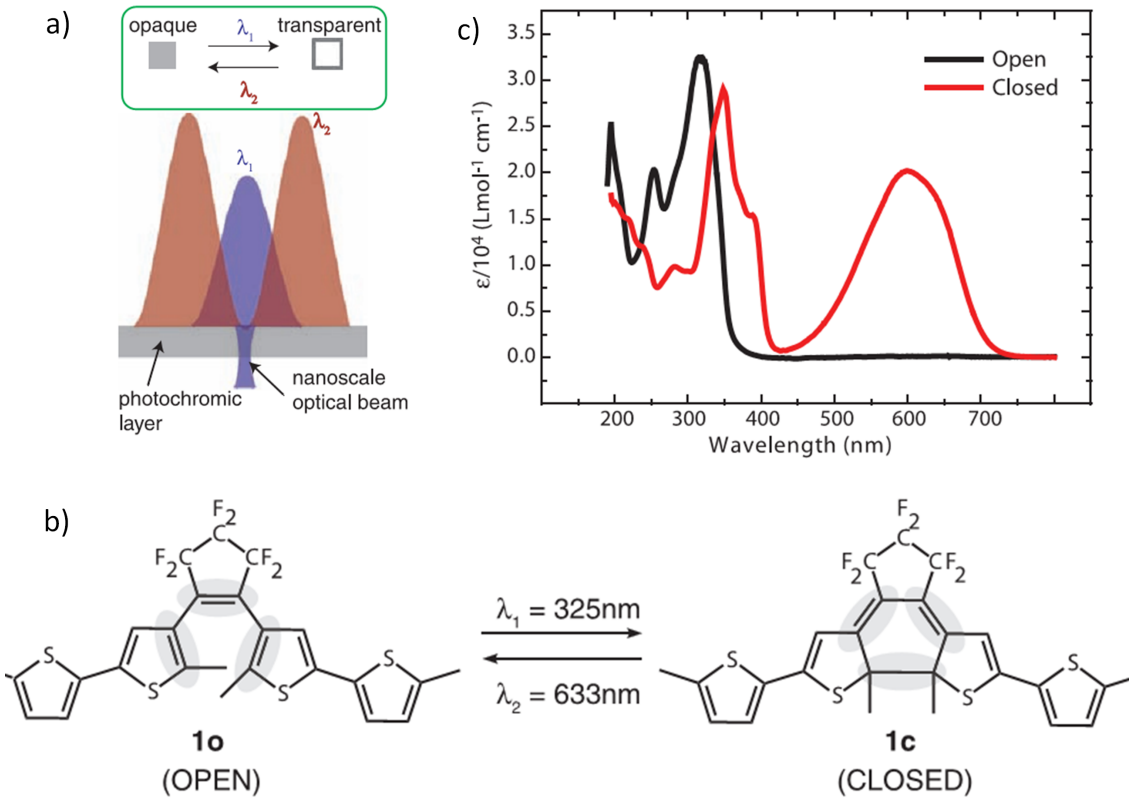

Figure 2.9: From [7]. Original caption: The scheme of absorbance modulation. a) The photochromic layer turns transparent upon exposure to λ_1 and opaque upon exposure to λ_2. When illuminated with a node at λ_2 coincident with a peak at λ_1, a subwavelength transparent region (or aperture) is formed through which photons at λ_1 penetrate, forming a nanoscale optical writing beam b) Structures of the open- and closed-ring isomers of compound 1. c) Absorbance spectra of compound 1 in the open and closed forms in hexane.

Another novel approach originated from the Fourkas group at Maryland, involving deactivation of the photoinitiator. In a method termed photoinduced deactivation, photoini-

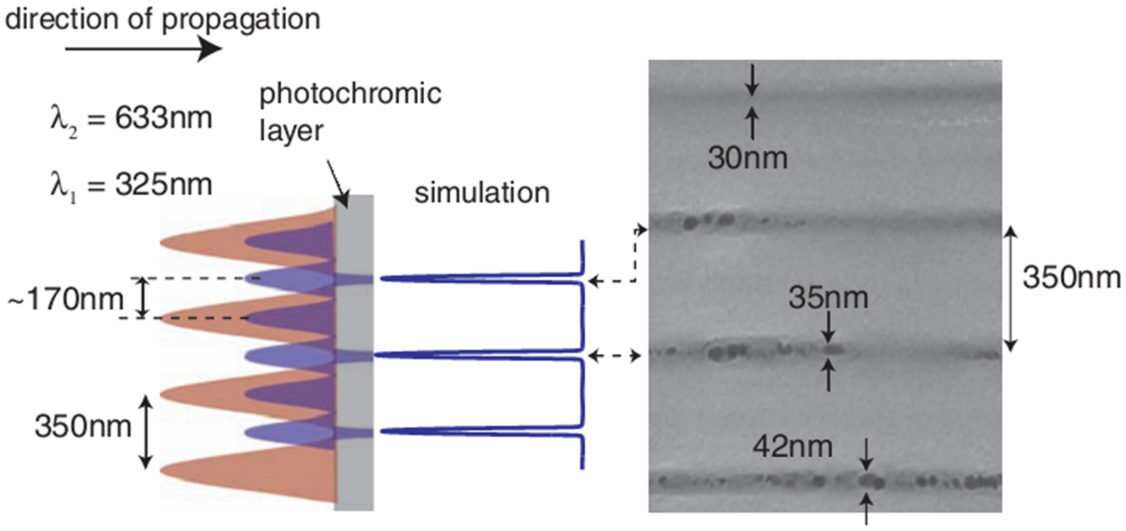

Figure 2.10: From [7]. The developed lines at the right were generated with absorbance modulation lithography, although it is unclear from this image whether the line narrowing is due to patterned photochromic absorbance or underlying resist contrast γ.

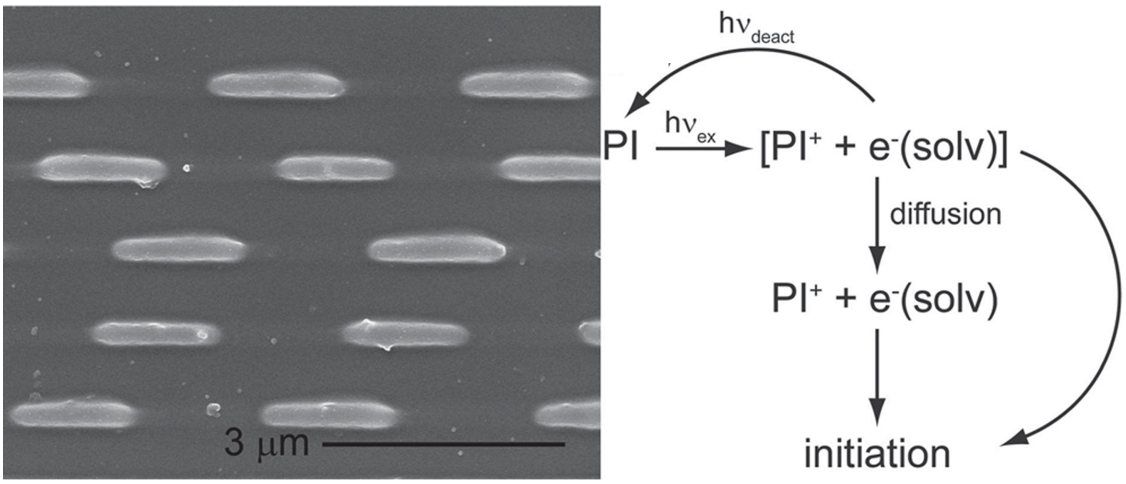

Figure 2.11: From [78]. Photoinduced deactivation of photoinitiation causes the voids that appear between the polymer dashes in the photo on the left. The relatively long deactivation time-window suggests that stimulated emission depletion of the excited singlet state does not play a role. Instead, Fourkas proposes (right) that an ejected, solvated photoelectron may be driven back into the parent molecule by the deactivation beam to regenerate the photoinitiator and prevent primary radical production.

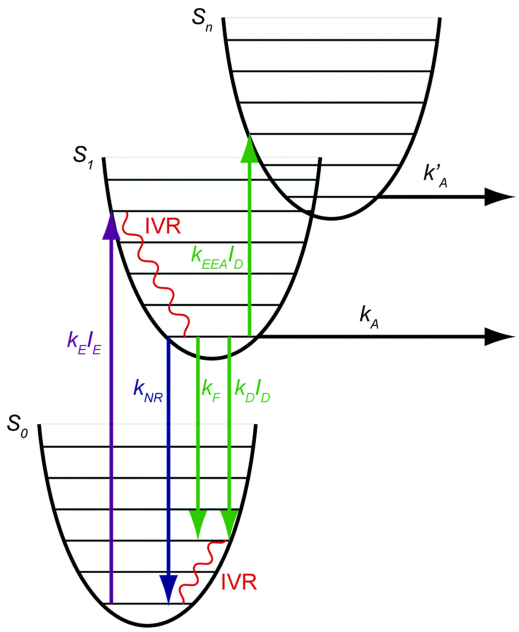

Figure 2.12: From [78]. Original caption: Photophysical scheme for STED-based, 2-colour photolithography. The photosensitiser begins in its electronic ground state S_0, and is driven to its first excited electronic state, S_1, via absorption (violet arrow) with rate constant $k_{\mathrm{E}}I_{\mathrm{E}}$. The electronically-excited molecule relaxes to its ground vibrational state via intramolecular vibrational redistribution (IVR). The molecule can then activate a reaction with rate constant k_{A}, relax nonradiatively with rate constant k_{NR}, fluoresce with rate constant k_{F}, or undergo stimulated emission with rate constant $k_{\mathrm{D}}I_{\mathrm{D}}$. It can also be driven to a higher electronic state S_{n} by the deactivation beam, with rate constant $k_{EEA}I_{\mathrm{D}}$. The rate constant for activation from S_{n}, $k_{\mathrm{A}'}$, is generally larger than k_{A}.

tiator is deactivated via a mechanism that appears to not be stimulated-emission depletion, as evidenced by the relatively long time constant associated with the deactivation process. They speculated that absorption from the excitation beam causes an electron to be ejected from the photosensitizer, becoming solvated but remaining nearby the parent molecule as shown in Fig. 2.11. Light from the deactivation beam then has the effect of driving the solvated electron back into the parent molecule, thus regenerating the photoinitiator and preventing radical initiation. They admit that the actual mechanism of photo-deactivation is poorly understood [78], and raise questions about the mechanisms in STED-based lithography as well. In this, they refer to a sister-technique developed primarily by the Wegener

group at Karlsruhe. The observed short lifetimes of the deactivation window is evidence that the deactivation mechanism is indeed STED-based. They excited a coumarin-based laser dye with two-photon absorption and were able to de-excite it with a CW beam, demonstrating a 13% resolution improvement in dense patterning [71]. The main difficulty with this family of techniques is achieving strong, selective deactivation. Excited-state absorption (see Fig. 2.12) is believed to be a major problem, but complexity in the electronic configuration of the photosensitizer has so far obscured clear understanding.

Yet another technique, attempting enhanced confinement of polymerization with photogenerated radical scavengers via single-photon kinetics, has been reported on by groups at Colorado [202] and Swinburne [80]. It is the subject of this thesis.

Chapter 3

Radical photopolymerization in thin films and the two-color response

Photoinhibited superresolution (PInSR) lithography involves orthogonal control of competing chemical reactions between photogenerated species. By projecting onto a resin film the superposition of complementary monochromatic light patterns at different wavelengths, patterned saturation of scavenger species may enhance spatial confinement of polymerization to exceed the optical diffraction limit. With the benefit of transient scavenger concentration, subsequent optical exposures add additional tightly-confined features to create a complete polymer pattern. Processing is finished with a solvent wash to clear away unpolymerized resin, yielding a polymer stencil with features that are, with respect to the optical imaging system, superresolved. This chapter introduces the fundamental photochemistry and development of the resin / monomer platform, and covers FTIR results concerning the relationship between photoinhibition and viscosity.

PInSR employs two photochemical processes to serve as interfaces between the optical and chemical systems. Photoinitiation occurs when a molecular species (or combination of species) called photoinitiator absorbs incident light and forms reactive primary radicals. These add to monomer, initiating a polymerization chain reaction that greatly amplifies the material-transforming effect of the absorbed light.

The second photochemical process is referred to here as photoinhibition. Like photoinitiator, photoinhibitor also absorbs light to produce radicals, but the scavenging radicals formed tend to inhibit polymerization instead of initiating it. Additionally, owing to separate

molecular structures, photoinhibitor may have an optical absorption spectrum completely different from the photoinitiator. This allows the possibility of orthogonal photoinitiation and photoinhibition.

3.1 Compounds for photoinitiation and photoinhibition of polymerization

Wavelength-selective optical absorption by the photoinitiator and photoinhibitor makes it advantageous to use narrow-band sources, and the need to produce tightly-focused spots requires a high degree of source coherence. Lasers are therefore an obvious choice. Beam wavelengths are chosen for maximally orthogonal excitation of the photoinitiator and photoinhibitor systems in the resist, which are co-chosen for having complementary spectra. A successful selection of compounds and source wavelengths was demonstrated in [202], and is used extensively in this work.

Photolithographic pattern transfer requires some kind of light-induced change in material properties, whether they be mechanical, chemical or optical in nature. Radical photopolymerization is an efficient means of achieving large mechanical change in a resin, especially when crosslinking occurs. During radical photopolymerization, light is first absorbed by photoinitiator and converted to primary radicals that add to monomer molecules. Radicals are conserved in the monomer addition, but relocate to the just-added monomer group where they may add to another monomer and another after that, in a chain reaction. This proceeds until the propagating chain is terminated by reacting with another radical; radicals are created and destroyed in pairs. In this process only initiator dissociation is endothermic at room-temperature, requiring energy from incident photons. Primary radical addition, chain propagation and termination are exothermic and happen spontaneously during and after light exposure.

Even without crosslinking, polymerization causes large changes in material solubility and mechanical properties. For example, at room-temperature monofunctional methyl methacrylate is a liquid with greater volatility and lower viscosity than water. With com-

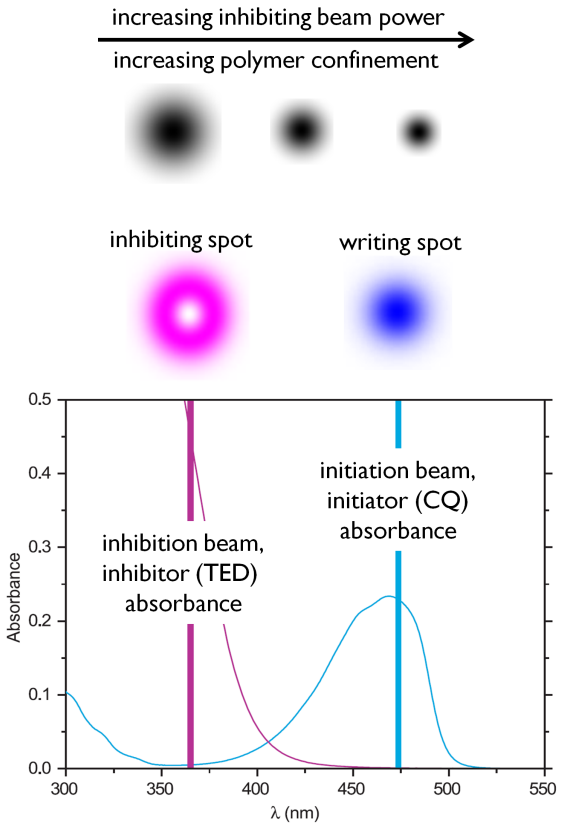

Figure 3.1: Superresolution is enabled by enhanced, but temporary, spatial confinement of cross-linking polymerization. Localized polymerization of monomer occurs within the focused spot of the 473 nm writing beam, initiated by the blue-light sensitive dye camphorquinone (CQ). The CQ absorption spectrum is rather interesting in that it contains a null near 365 nm, providing a window for selective photoexcitation of another species. Localized inhibition / retardation of polymerization occurs within the donut-shaped focal spot of the 364 nm inhibiting beam, caused by photodissociation of TED into DTC radical scavengers. Orthogonal two-color control is enabled by the complimentary absorption spectra of the photoinitiator (CQ) and the photoinhibitor (TED). When the donut-shaped inhibiting spot is superimposed upon the writing spot, increased inhibiting beam power results in increased spatial confinement and a smaller polymer dot.

plete polymerization into poly(methyl methacrylate), the resulting thermoplastic is a strong solid with typical melting point of 160 °C. When multifunctional monomers are polymerized, crosslinks form between the polymer chains. After sufficient crosslinking a continuous network forms and the resin is said to have gelled. Solvent may penetrate this network and cause it to swell, but unlike unreacted monomer or unattached oligomer the crosslinked network

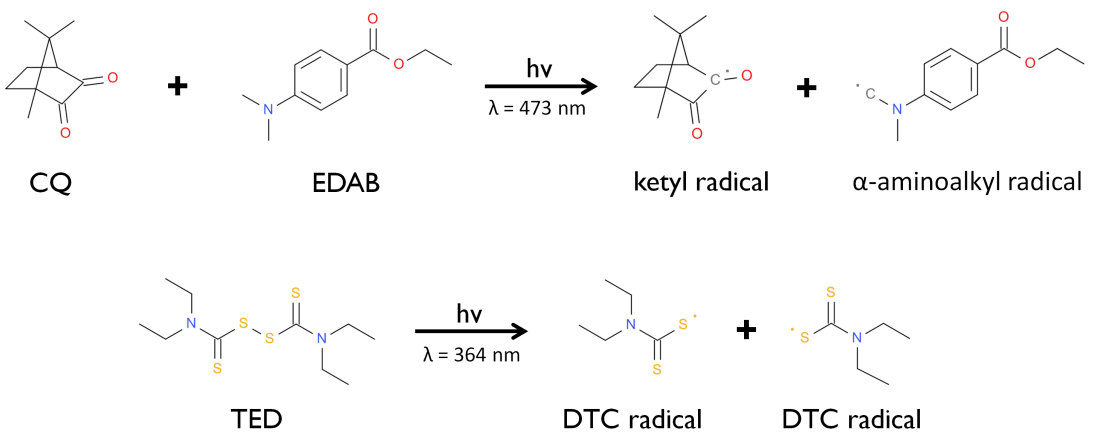

Figure 3.2: Camphorquinone (CQ) is a blue-sensitive dye that is paired with a tertiary-amine coinitiator to initiate radical polymerization. Tetraethylthiuram disulfide (TED) undergoes homolytic cleavage under near-UV light to produce dithiocarbamyl (DTC) radicals that terminate (but do not efficiently initiate) chain polymerization.

cannot be dissolved. This feature may be exploited to form a binary polymer stencil: after a solvent rinse, only light-cured regions remain and may be used to as a chemical or physical resist for subsequent processing steps.

Photoinhibited superresolution lithography makes use of a Norrish type II initiating system, consisting of the dye camphorquinone (CQ) and the electron-donating tertiary amine ethyl 4-(dimethylamino) benzoate (EDAB). CQ is chosen for its absorption spectrum, which features a peak in the blue at $\lambda = 469$ nm, and a deep trough in the near-UV at $\lambda = 365$ nm. Upon absorbing a photon of blue light, CQ is promoted to a short-lived excited-singlet state from which it can undergo intersystem crossing to an excited triplet state. It may then react with the co-initiator EDAB by abstracting a hydrogen, thus creating a relatively unreactive ketyl radical on the parent CQ molecule and an α-aminoalkyl primary radical on the parent EDAB molecule that can add into monomer to initiate chain polymerization.

There is a large and growing variety of monomers available for radical polymerization. In this work, methacrylates such as triethylene glycol dimethacrylate (TEGDMA)

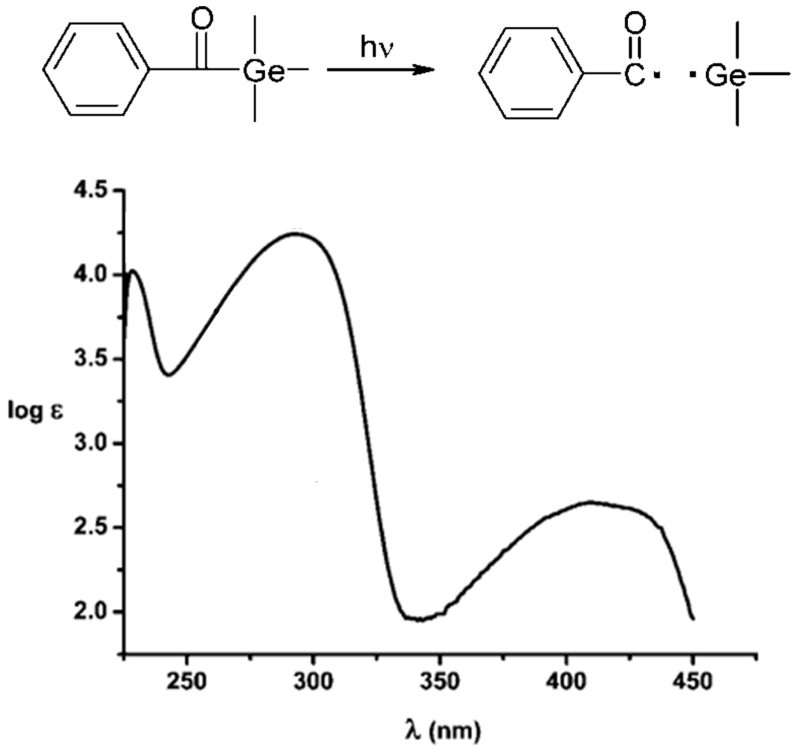

Figure 3.3: From [65]. Benzoyltrimethylgermane (BTM-Ge) is a Norrish type-I photoinitiator, with an absorption spectrum that features sensitivity in the visible-band and a relatively lower-absorbing window in the near-UV. BTM-Ge may be an attractive alternative to CQ for two reasons: both photogenerated radicals (acyl and germyl) should efficiently add to methacrylate monomer, and a co-initiator is not required.

and isophorone urethane dimethacrylate (UDMA-IPDI) are generally used. Acrylate-based resins would cure more quickly but are unfortunately incompatible with TED, as discussed below. The multifunctional nature of the monomer allows crosslinking, whereby two polymer chains incorporate the same monomer unit. Difunctional monomers are used here only because they are widely available; monomers with 3 or more methacrylate reactive groups may allow PInSR resins with more efficient dose-to-gellation.

Typical resin systems with photoinitiator and monomer, if designed correctly, can be used for diffraction-limited photopolymerizatation lithography. Resolution beyond $\lambda/\ 4NA$ requires some type of non-linear optical response, provided in photoinhibition superresolution

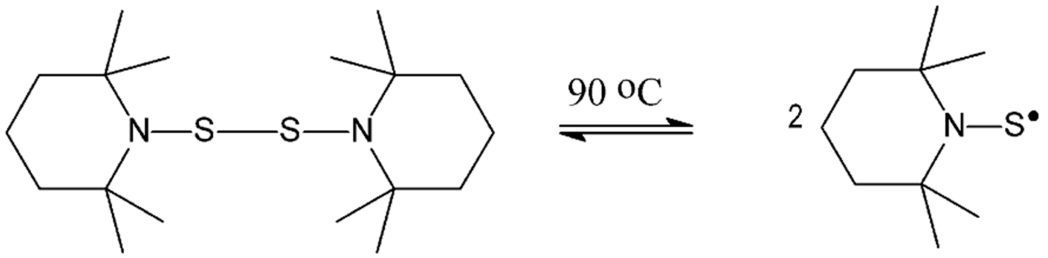

Figure 3.4: From [32]. The compound 2,2,6,6-tetramethylpiperidin-1-yl disulfide can undergo homolytic cleavage to produce 2,2,6,6-tetramethylpiperidin-1-ylthiyl (TEMPS), the sulfur analogue of TEMPO. While additional work is required to determine the suitability of TEMPS as a photoinhibitor, it may have advantages over TED. The presence of methyl groups around the disulfide bond may reduce undesired chain-transfer of primary or propagating radicals into the disulfide, thus enabling use with fast-reacting acrlyate monomer. Also, chain-termination with TEMPS may be irreversible, eliminating the possibility of continued living-radical polymerization under UV illumination.

lithography by two-color control of polymerization.

As mentioned earlier, PInSR lithography uses a second beam to control a photopatterned termination mechanism. Tetraethylthiuram disulfide (TED), known in the literature as an iniferter, is used here as a photoinhibitor and is the parent molecule of scavenging radicals that can cross-terminate primary and propagating radicals. The term iniferter was coined by Otsu [181] as a shortened form of initiator / chain transfer agent, a class of compound useful for living radical polymerization. While PInSR is not an implementation of living-radical polymerization per se, it does appropriate the use of photo-induced attenuation of the polymerization rate. This owes to the (mostly) non-initiating, sulfur-centered dithiocarbamate (DTC) radicals created by photocleaving TED with near-UV light. While not efficient in starting a propagating polymer chain, DTC radicals will readily combine with primary and propagating radicals, retarding the polymer conversion rate. DTC radicals will also recombine with other DTC radicals at a nearly diffusion-limited rate [191], thus regenerating TED.

3.2 Evidence of photoinhibition, side-reactions

In this work, it is necessary to have a parameter that describes the photoinhibition efficacy of a particular resin under particular experimental conditions. For this I introduce the term "photoinhibition contrast" (PIC), defined here as the ratio of average polymerization rate under blue-only illumination to the average polymerization rate under both blue and UV illumination. For two-color FTIR measurements of polymer conversion, this is done by taking the ratio of slopes for one and two-color conversion vs. time plots during a specified interval. For patterned photoinhibition experiments, PIC is determined by taking the ratio of exposure time required to gel the sample under superimposed blue and UV focused spots to exposure time required to gel the sample under a blue-only focused spot. For such a measurement to be meaningful, blue irradiance must be held constant for the blue-only and blue+UV experiments. Although this parameter has the shortcoming that it depends on illumination conditions, it is helpful for describing photoinhibition efficacy. Photoinhibition contrast, together with diffusion-induced pattern blurring, determine the degree of superresolution that is possible in a PInSR system.

Several side reactions are possible in this system. DTC radicals are capable of initiating chain polymerization, but this typically requires temperatures of 80 °C or higher [163]. In experiments conducted during this work, methacrylate resins containing TED and no other photoinitiator did not polymerize even after several hours of UV exposure at ∼10 $mW{\cdot}cm^{-2}$. Importantly for living-radical polymerization, DTC end-caps may absorb near-UV light and detach from polymer chains. This allows chain growth to resume, although a high concentration of DTC radicals would tend to minimize growth of resurrected chains by causing them to be quickly recapped. Another unwanted and likely more-significant side reaction is initiation by the near-UV beam. This can be caused by CQ excitation at $\lambda = 364$ nm or by another unintended photoreaction, such as photoinitiation from impurities. This has a direct impact on the degree to which polymerization can be suppressed, a fundamental

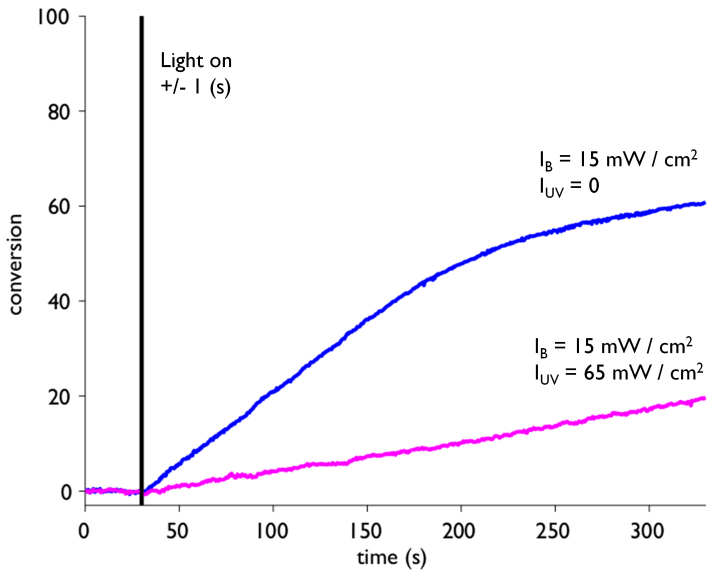

Figure 3.5: Two-color photopolymerization of triethyleneglycol dimethacrylate (TEGDMA) resin, containing 1 wt% CQ, 0.5 wt% EDAB and 3 wt% TED. Neat TEGDMA viscosity $\eta =$ 10.2 [198]. Retarded cure under additional UV illumination is the basis for two-color control. This resin is used in the first published description of the photoinitiation / photoinhibition superresolution scheme [202]. Photoinhibition contrast (ratio of slopes) is 3.7, measured in the interval $40 < t < 60$ (s).

factor limiting superresolution ability.

For many non-biological applications, acrylate monomers are preferred due to benefits of their higher reactivity. The kinetic propagation constant k_p of a typical acrylate is on the order of 20,000 M·s^{-1}, significantly higher than a typical methacrylate with k_p on the order of 300 - 1,000 M·s^{-1}. Faster propagation can result in greater light sensitivity and faster curing.

Unfortunately, acrylates cannot be used in PInSR resists due to a strong interaction with the uncleaved photoinhibitor TED. By design, TED should be inert in the resin apart from UV photosensitivity. What I have observed, however, is that TED powerfully inhibits polymerization of acrylates. Blue-light initiated photopolymerization of an acrylate is shown in Fig. 3.6, with and without TED. Anomalous results of other groups notwithstanding [80], acrylate-based resins containing TED would seem impractical.

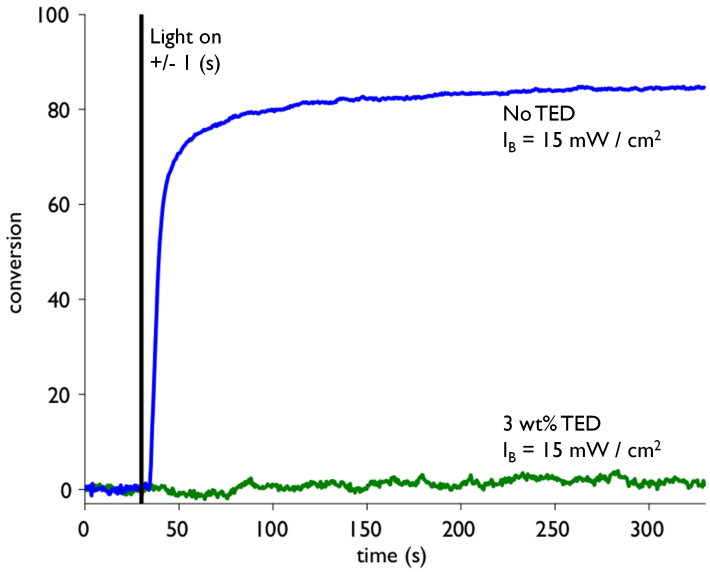

Figure 3.6: TED effect on acrylate photopolymerization. Strong inhibition is likely caused by acrylate chain-transfer to the TED molecule, resulting in a DTC-terminated chain and a non-initiating DTC radical. Base resin is hexanediol diacrylate (HDDA) with 1 wt % CQ and 0.5 wt% EDAB.

Of the physical parameters, resin viscosity is perhaps the most important aspect of PInSR resists. This is due to many factors, especially the need for low mobility and species confinement which will be discussed in a later section. Viscosity can have a large effect on polymerization rate or photosensitivity, with peak polymerization rate R_p tending to be higher during the cure of more viscous resins. This arises from suppressed termination kinetics, radical termination being generally diffusion-limited.

3.3 Necessity of the thin-film configuration and the associated effects of resin viscosity on photoinhibition

In the initial work on this topic, small features were written into a bulk TEGDMA formulation sandwiched between glass plates. This configuration has the advantage of simplicity and impermeability to atmospheric oxygen, but the 10 μm minimum thickness achievable between glass slides makes it unusable for dense patterning with single-photon absorption

kinetics. Spin-coating is an attractive alternative, as it is commonly used to produce uniform thin films with arbitrary thickness; such films need only be cured in an environment purged of oxygen.

Thin films may be formed instantaneously if the TEGDMA formulation is deposited on a spinning substrate, but of low viscosity liquids only the few that are super-wetting [63] can be spun to stable thin films that resist rupture. Liquids with high viscosity, on the other hand, flow more slowly and can resist rupture for significant intervals. In spin-coating trials, I observed that UDMA (Sigma) and other monomers with viscosity $\eta > 8{,}500$ cP are good candidates for open 1 μm films. Alternatively, linear polymers such as PMMA may be added to increase viscosity; these films may be additionally stabilized against rupture by entanglement effects [242].

Choice of solvents is crucial for good spin-casting. High solubility of solids (the non-volatile resin or resist to be deposited on the substrate) in the solvent is required to prevent precipitation before solvent evaporation is complete. Also, solvent vapor pressure should be relatively low to moderate the evaporation rate and thus prevent dynamic evaporation from causing ripples in the spin-coated film, also known as the "orange-peel" effect [130]. For these reasons, solvents such as PGMEA ($\eta = 3.7$ Torr, 20 °C) and cyclohexanone ($\eta = 3.4$ Torr, 20 °C) are commonly used to spin-cast organic resins and resists.

Another important aspect of resist chemistry to consider is substrate adhesion. Crosslinked polymer on smooth glass can be accidentally washed away during solvent rinse, but certain measures can prevent this. One method is to react a silane coupling agent onto the glass surface; examples are shown in Fig. 3.7.

Use of silane coupling agents can result in robust covalent bonds with the substrate, but also tends to lower the surface energy which can degrade resin wetting. An alternative is to incorporate an adhesion promoter in the resin and leave the glass surface clean and unaltered. Several new adhesion promoters came on the market from Esstech at the time of this writing, and though the structures are proprietary they have been beneficial in this work.

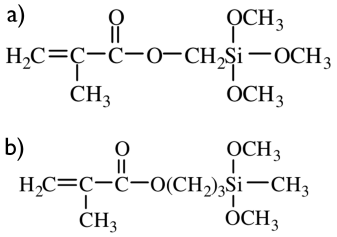

Figure 3.7: Methacrylate silane coupling agents from Gelest: a) trialkoxy structure, b) dialkoxy structure. Functional groups including the Si atom attach to glass or silicon wafers, while the methacrylate groups incorporate in (meth)acrylate polymer chains [85].

Results obtained with 5 wt% PL-2212 (Esstech) have been especially good, and comparable to that of silane coupling agents.

In bulk tests using FTIR spectroscopy, various neat resins were characterized for photoinhibition. Within the initial screening, reasonable photoinhibition efficacy is observed with low-viscosity monomers like TEGDMA and HDDMA. With the high-viscosity UDMA (η = 8,500 cP), however, no photoinhibition effect is observed at all under the test conditions (see Fig. 3.11).

In a second round of tests [76], I added high and low-viscosity inert diluents to a TEGDMA resin (η = 10 cP, neat) to assess the effect on photoinhibition. Dilution with low-viscosity hexane (η = 0.4 cP) improved photoinhibition contrast to 7.0, while dilution with higher-viscosity triethylene glycol (η = 40 cP) degraded photoinhibition contrast to 2.1. Assuming no change in the chemistry, this suggests that photoinhibition is viscosity-dependent.

In a third test, I mixed a low-viscosity diluent (cyclohexanone, η = 2 cP) to UDMA photoinhibition resin at 50 wt%. This dramatically improved photoinhibition contrast from 1 (no effect, Fig. 3.11) to 7.3, as shown in Fig. 3.12.

As I will show later, radical photoinhibition with TED is not impossible at high viscosity. But in the experimental regime where analytical instruments such a FTIR spectrometers are commonly used, with light irradiance in the range 0.5 - 50 mW·cm^{-2}, photoinhibition

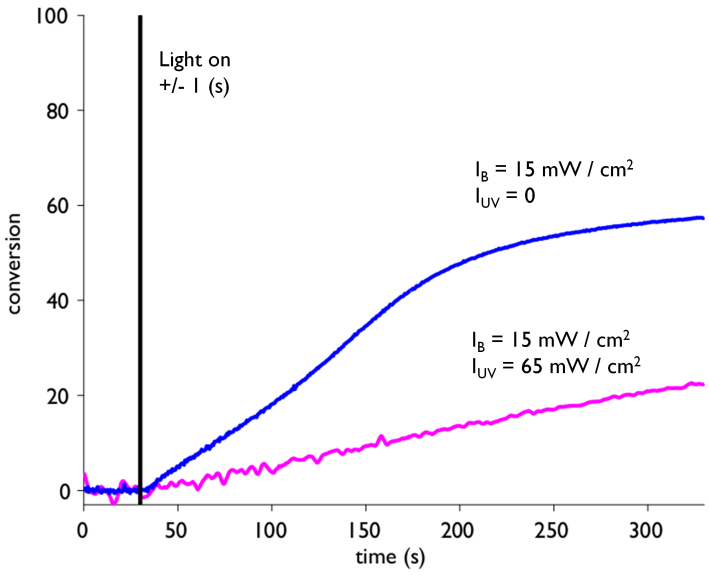

Figure 3.8: Two-color photopolymerization of hexanediol dimethacrylate (HDDMA), containing 1 wt% CQ, 0.5 wt% EDAB and 3 wt% TED. Neat HDDMA viscosity $\eta = 4$ [198]. This demonstrates that in addition to TEGDMA, the two-color response can occur in other non-viscous methacrylate resins at typical flood-cure irradiances. Photoinhibition contrast is 5.1, measured in the interval $40 < t < 100$ (s).

efficacy is strongly reduced with increasing viscosity. This is overcome with the very high irradiance of a focused laser spot, where TED-based photoinhibition and high viscosity can co-exist. But the valuable techniques commonly used in photopolymers research cannot easily be adapted to this regime, and without these tools the research becomes significantly more difficult.

One explanation for poor photoinhibition in high viscosity resins is geminate recombination of TED: the DTC radical pair produced from TED photocleavage does not escape its solvent cage and instead recombines to reproduce the parent molecule. This effect is observed in other high-viscosity systems, and is equivalent to a reduced quantum yield for the reaction TED + hν $\rightarrow$ DTC$\cdot$ + DTC$\cdot$. A reproduction of the flash laser photolysis experiments by Plyusnin [191], but with higher-viscosity solvents, could test this hypothesis.

Another explanation for the photoinhibition / viscosity relationship is suppressed ter-

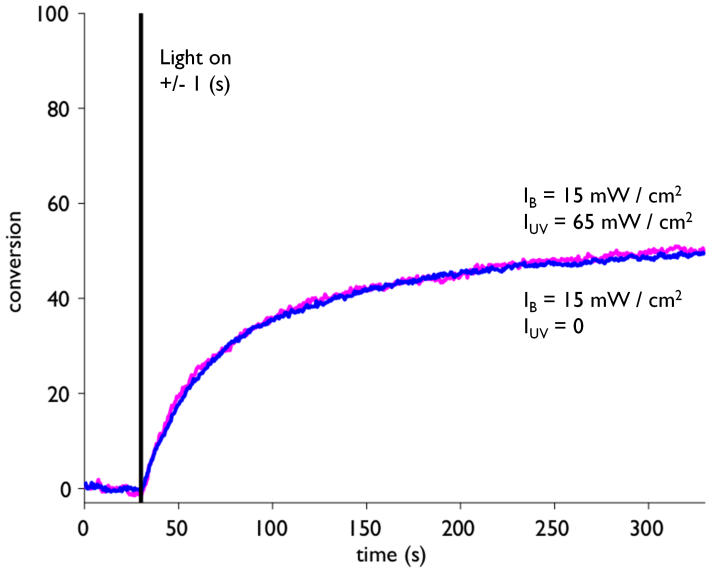

Figure 3.9: Two-color photopolymerization of ethoxylated (2) bisphenol-A dimethacrylate (E2BADMA), containing 1 wt% CQ, 0.5 wt% EDAB and 3 wt% TED. Neat E2BADMA viscosity η = 1,082 cP [199]. Photoinhibition is not observed under these conditions (photoinhibition contrast is 1), though it is observed under very high UV irradiance [38].

mination. Rate constants for radical combination are typically very high, on the order of 10^9 - 10^{10} M·s^{-1} in non-viscous liquid media, so are typically limited by diffusion. When diffusivity is reduced the termination rate constant is similarly reduced, with little effect on rates of initiation and propagation. A well-known example of this is the autoacceleration effect, observed during the radical polymerization of initially low-viscosity resin. As polymer conversion increases, mobility decreases thus slowing termination. Assuming steady-state where $R_\mathrm{i} = R_\mathrm{t}$, this forces a higher concentration of propagating radicals and results in a higher polymerization rate R_p.

Strongly suppressed photoinhibition efficacy was observed over a series of FTIR photocuring experiments, in which the photoinitiator choice, photoinitiator concentration, illumination wavelength and incident irradiance were all identical. The primary-radical generation rate therefore should have been constant, to first order, for all the resins characterized.

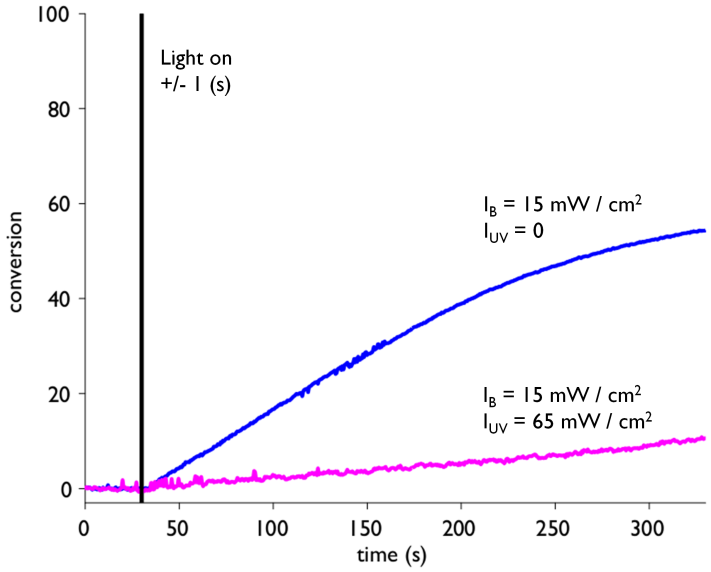

Figure 3.10: Two-color photopolymerization of TEGDMA containing 1 wt% CQ, 0.5 wt% EDAB and 3 wt% TED, mixed 3:1 with hexane diluent. The photoinhibition effect is enhanced, compared to results from the non-diluted TEGDMA resin in Fig. 3.5. Photoinhibition contrast is 8.6, measured in the interval $40 < t < 100$ (s).

But the rate of cross-termination, in which a DTC radical combines with a primary or propagating radical, is the product of both radical concentrations and the rate constant k_t. This rate constant is diffusion-limited, and so decreases approximately linearly with viscosity. So even with zero geminate recombination, equivalent photoinhibition in a resin with 10x increased viscosity would require 10x increased DTC radical concentration.

I used the ring-opening inhibitor 1,4,4-trimethyl-2,3-diazabicyclo[3.2.2]non-2-ene 2,3-dioxide (TAOBN, Hampford Research) to test this hypothesis. TAOBN is understood to be reactive as a radical scavenger in its open state but not in its closed state, with the equilibrium proportion of rings in the open-state being a function of temperature. This simulates a TED-containing resin exposed to UV light, but without the possibility of bimolecular geminate-recombination of the inhibitor. Time-resolved FTIR polymer conversion results of the TEGDMA control experiment ($\eta = 10$ cP) are shown in Fig. 3.13, and demonstrate the

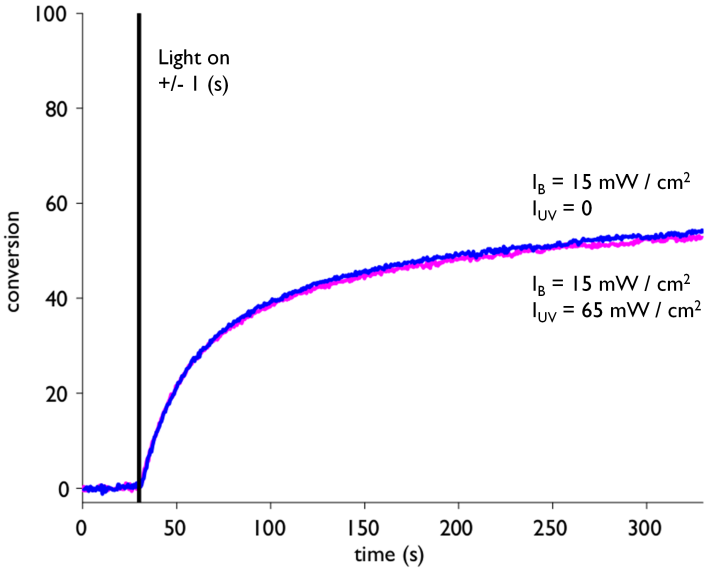

Figure 3.11: Two-color photopolymerization of urethane dimethacrylate (UDMA, Sigma) resin, containing 1 wt% CQ, 0.5 wt% EDAB and 3 wt% TED. Neat UDMA viscosity η = 8,500 cP [67]. The two-color response appears to be completely suppressed as with E2BADMA.

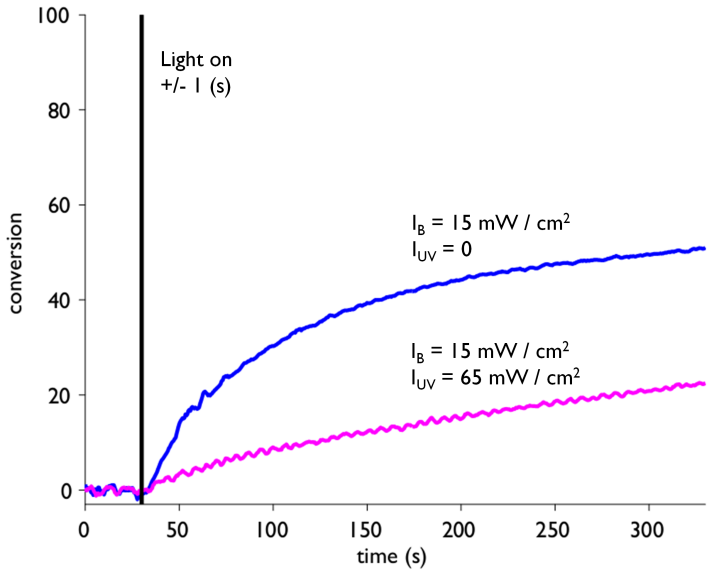

Figure 3.12: Two-color photopolymerization of UDMA resin, containing 1 wt% CQ, 0.5 wt% EDAB and 3 wt% TED, mixed 1:1 with non-viscous cyclohexanone diluent. Photoinhibition contrast is 5.1, measured in the interval $40 < t < 60$ (s).

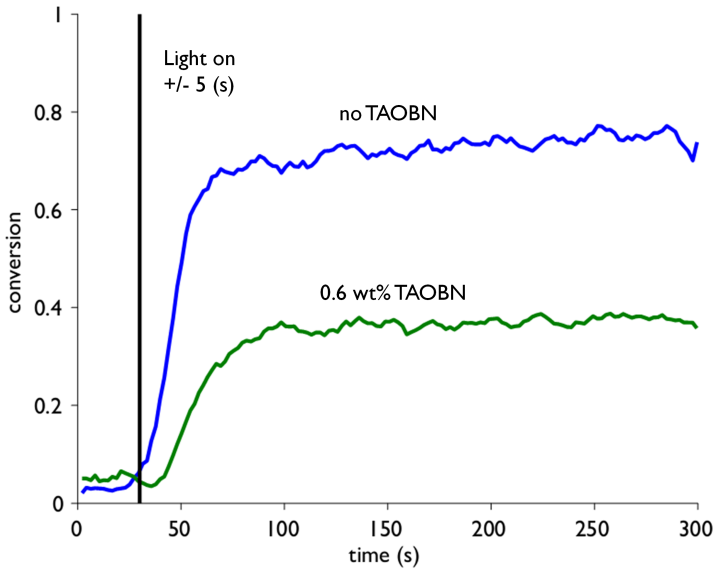

Figure 3.13: TAOBN retards room-temperature photopolymerization of TEGDMA resin containing 0.5 wt% TPO, under 365 nm illumination at 5 mW·cm^{-2}. The premature conversion plateau in TAOBN-containing resin is likely due to exhaustion of initiator. Photoinhibition contrast is 2.5, measured in the interval $40 < t < 60$ (s) for the control and $45 < t < 65$ (s) for the test. The apparent ∼5 s delay in conversion of the TAOBN-containing test experiment is most likely due to delayed onset of illumination (caused by a sticky shutter).

significant effect of 0.6 wt% TAOBN. Results from the UDMA test samples (η = 8,500 cP) are shown in Fig. 3.14, and indicate 0.6 wt% TAOBN had little or no effect. The difference between the control and experiment results is remarkable, and suggests that geminate recombination effects are not necessary to explain the viscosity-dependence of photoinhibition shown above.

One interesting caveat to the photoinhibition / viscosity results is the case of TEGDMA mixed 1:1 with PMMA (120k MW). Despite much slower flow and greater thin-film stability than the other bulk-monomer viscous resins, a small amount of photoinhibition was observed as shown in Fig. 3.15. This is likely due to relatively high mobility for small molecular species, allowed by excess free-volume around the PMMA coils.

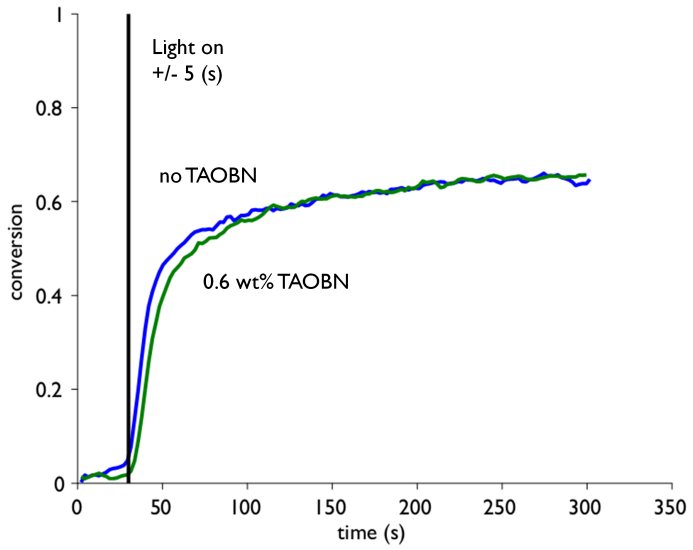

Figure 3.14: TAOBN fails to retard photopolymerization of UDMA (Esstech) resin containing 0.5 wt% TPO, under 365 nm illumination at 5 mW·cm^{-2}. Seperate experiments showed that inhibition of UDMA photopolymerization was possible, but required 10-20 wt% TAOBN. Photoinhibition contrast is roughly 1.

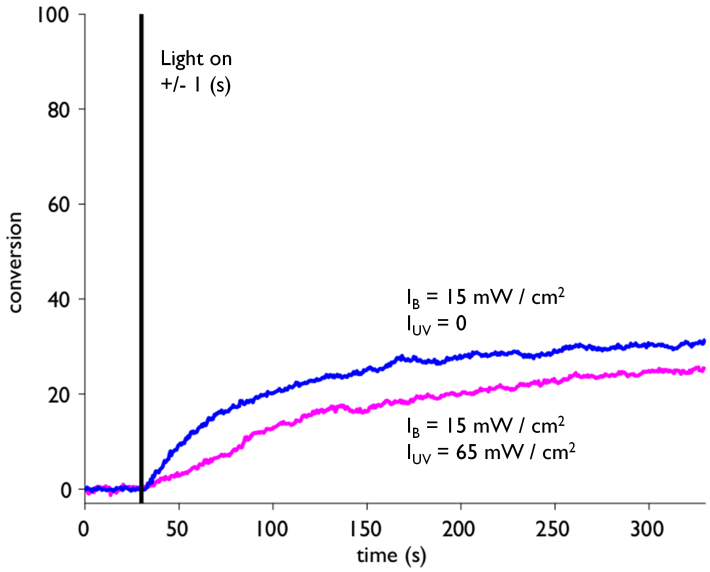

Figure 3.15: Two-color photopolymerization of TEGDMA containing 1 wt% CQ, 0.5 wt% EDAB and 3 wt% TED, mixed 1:1 with PMMA (120k, Sigma). The observed photoinhibition in this viscous film may be due to large macroviscosity and small microviscosity, as discussed by North and Reed [175]. Photoinhibition contrast is 2.8, measured in the interval $40 < t < 60$ (s).

Chapter 4

Two-color laser direct write system

The experimental layout and controls for PInSR direct write lithography is similar to that of STED microscopy, from which PInSR was inspired. But specific requirements, especially focusing and sample mounting, necessitate design and construction of a custom writing station. This chapter covers sources, optics, electronics, positioning and system control. Also described is a special mount and oxygen-removing purge system, required for polymerization of the radical-initiated thin-film.

Thanks to single-photon absorption kinetics, the two-color photoinhibited superresolution (PInSR) approach can ideally be adapted for high-throughput projection lithography. But for the work presented here, a direct-write configuration is used and the experiment closely resembles a stimulated emission depletion (STED) microscope. Both systems utilize Gauss and Gauss-Laguerre beams at different wavelengths for orthogonal control of material response; the STED deactivation and pump beams are replaced in PInSR with inhibiting and writing beams.

Reviewing the photochemistry, camphorquinone (CQ) is a visible-light photoinitiator that can react with a non-photosensitive tertiary-amine coinitiator to generate primary radicals. Tetraethylthiuram disulfide (TED), used here as the photoinhibitor, is an ultraviolet-activated radical scavenger. TED does not have appreciable absorption in the visible spectrum, but increasingly absorbs shorter wavelengths in the ultraviolet (UV). CQ is common in dental resins, with a peak absorption in the blue and an almost non-absorbing null in

the ultraviolet near the mercury i-line. Since TED does have some absorption at this wavelength, the $\lambda = 364$ nm emission from an Ar+ laser is chosen for the inhibition beam. A broader wavelength selection is possible for the writing beam, given the non-absorption of TED in the visible, but excitation near the CQ absorption peak at $\lambda = 469$ nm makes the most efficient use of photons. A $\lambda = 473$ nm diode laser is therefore chosen to supply the writing beam.

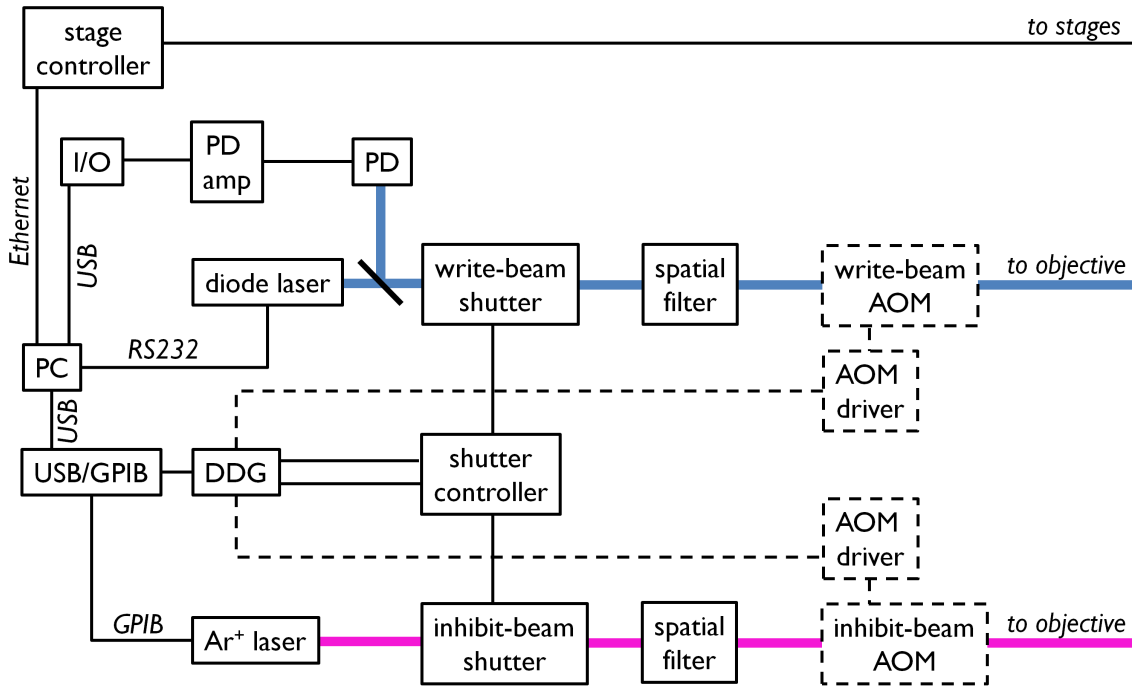

Figure 4.1: PInSR controls schematic.

4.1 Optical setup

A 20 mW CW blue $\lambda = 473$ nm diode laser from Omicron (Rodgau, Germany) is used to supply a stable, low noise, high wavefront quality writing beam. Also tried were lasers from B&W Tek (Newark, DE) and CrystaLaser (Reno, NV), which use diode-pumped solid-

state (DPSS) technology to induce Nd lasing at 948 nm, which is then frequency-doubled. These lasers were rejected when large power drift and high frequency noise were observed; output drift prevents consistent lithographic exposures, and high-frequency modulation can wreak havoc on the kinetics of radical photopolymerization.

An argon-ion (Ar+) laser from the Coherent Innova 300C series supplies a $\lambda = 363.8$ nm UV inhibiting beam, by way of a single-line output coupler. Beam power, along with other parameters, is adjusted by changing commanded tube current or setpoint optical power (using feedback from an internal power meter). It is useful during patterning experiments to change setpoint power from automation control software, and this is accomplished via RS232. Constant-current mode is preferred for reliable tube starting; switching to constant-output afterwards provides exposure repeatability. The setpoint power and observed output power, as measured with a separate power meter, have a linear relationship but a non-unity scaling factor may cause the absolute power readout to be inaccurate. Water-cooling is required for laser operation, and insufficiently fast or cool water flow can cause the controller to fault.

Writing and inhibiting beams are made to pass through standard attenuators, beam splitters, spatial filters and beam expanders, and are steered by 4f relays that image the steering mirror onto the objective back-focal plane. Just before the objective, the beams are combined with a dichroic mirror that reflects at $\lambda = 473$ nm and transmits at $\lambda = 364$ nm. Fused-silica lenses are used along the UV beam to prevent unwanted attenuation. UV doublets were used initially, but extended exposure of the spatial-filter focusing lens to the high-intensity unexpanded beam tended to induce damage in the cement between the elements, thus causing significant absorption and aberration of the beam. To solve this problem, long focal-length singlets are used to focus the narrow beam into the spatial filter. Beyond the spatial filter, a charge-1 spiral phase plate (SPP), design wavelength $\lambda_{\text{des}} = 365$ nm from RPC Photonics (Rochester, NY) is optionally inserted into the Gaussian beam to convert it to the donut-shaped GL_0^1 mode. STED researchers working with non-paraxial (high-NA) GL_0^1 beams have observed that clean, axially-symmetric and dark-centered spots only oc-

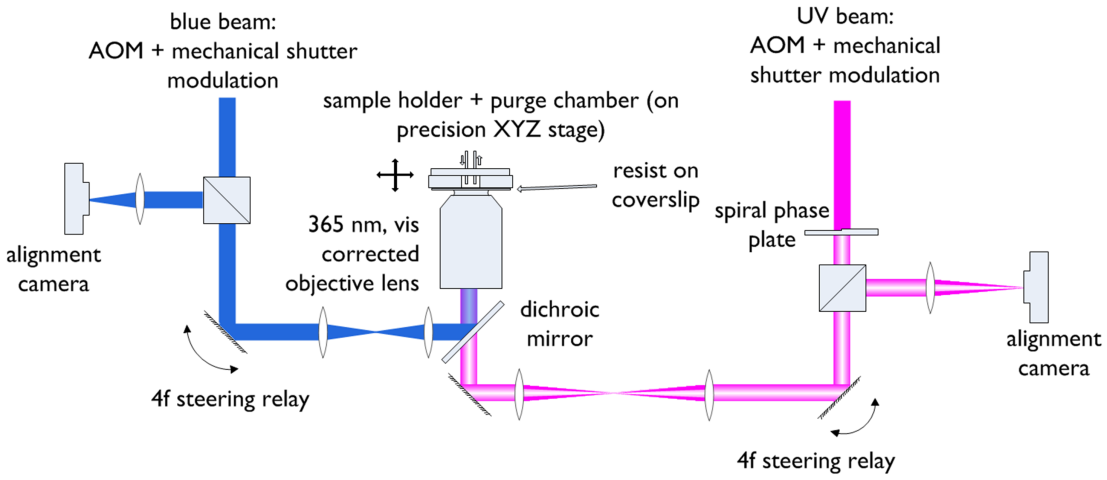

Figure 4.2: PInSR optical schematic. The blue writing beam and UV inhibiting beam are filtered and modulated before passing into 4f relays, which image a steering mirror onto the objective back focal plane. A dichroic mirror in the last relay segment combines the beams. Photosensitive thin-film samples are mounted across a purge chamber, vertically positioned in beam focus and scanned horizontally for writing.

cur with near-perfect circular polarization (see [194], references therein). While obtaining highly circularly-polarized beams is relatively straightforward with linearly polarized light and quarter-wave plate, phase effects from out-of-plane turning mirrors and restricted clearance in the steering relay necessitate two waveplates placed farther up the beam. The goal is to pre-compensate for later polarization distortions by generating a particular elliptical polarization: a half-waveplate rotates the linearly polarized beam to a particular orientation and quarter-waveplate introduces a particular degree of ellipticity. Optimum orientation of both elements is determined by iterative repositioning of each element to minimize sinusoidal power fluctuations, measured on a power meter placed beyond a spinning analyzer at the objective mount. When optimized, the beam is highly elliptical exiting the quarter-wave plate but nearly circular at the objective mount (typical degree of circular polarization $\approx$ 0.97).

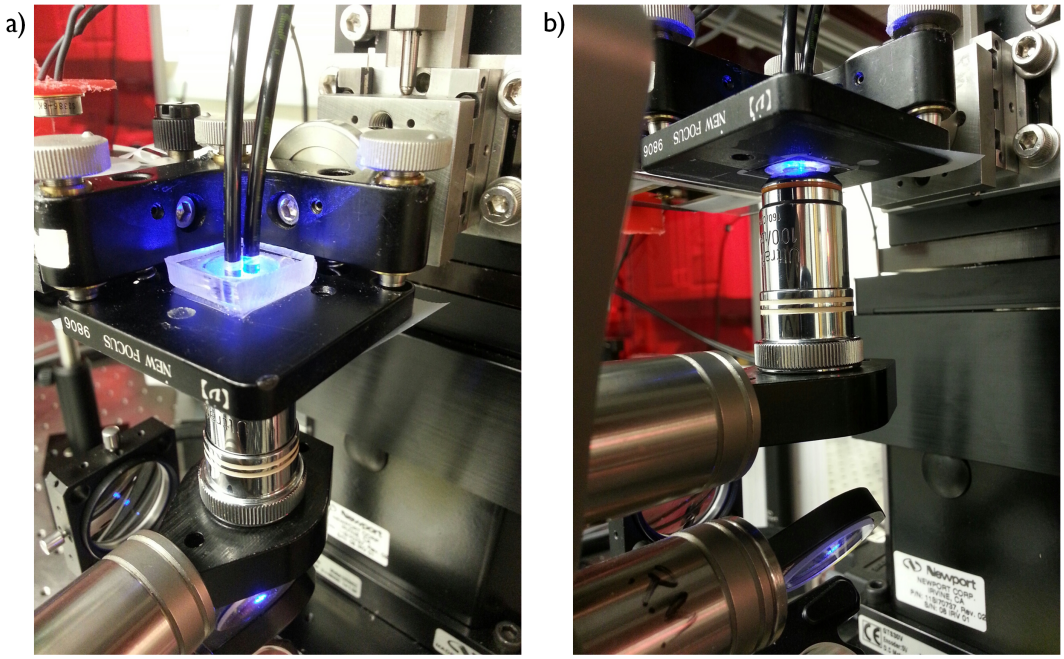

Figure 4.3: Sample holder at focus position above objective. a) From above: purge chamber consists of a 10 mm circular hole capped with a square plexiglass window, with one 1/8" OD nylon tube for gas supply and another for exhaust. Tip/tilt is adjusted by thumbscrews. b) From below: resist-on-coverslip sample is placed over the purge chamber and held in place with sticky-tape.

Focusing is achieved by detecting sample-surface reflections that pass back through the spatial filter pinhole during an axial scan. A beamsplitter redirects the weak confocal reflection to a low-noise photoreceiver (New Focus 1801) with fixed gain. The photoreceiver output is biased and amplified by a 2-stage amplifier, with gain optimized to fill the A/D dynamic range during an air/glass surface pass through the beam focus.

The GL_0^1 dark central null is critical for PInSR direct-write, and numerical simulations help to understand SPP fabrication and alignment tolerances in the system. Figures 4.6 and 4.7 show three important simulated cases of a monochromatic beam that has passed through a spiral phase plate, computed by Fourier-transform. SPPs may be made with a finite number

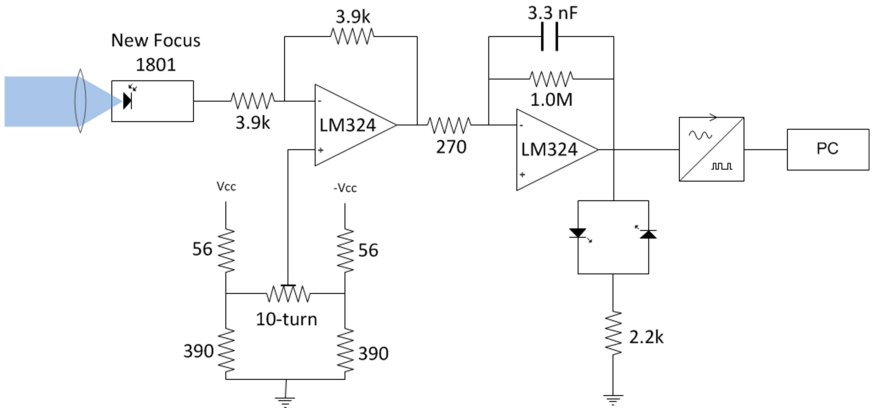

Figure 4.4: Focus detector schematic: Confocal reflected light is focused onto a silicon photodiode with an integrated low-noise preamp (New Focus 1801 photoreceiver). To compensate for thermal drift and ambient light, receiver signal bias is adjusted with a unity-gain inverting amplifier before passing into a high gain amplifier. Visible LEDs provide a visual indication of confocal reflection.

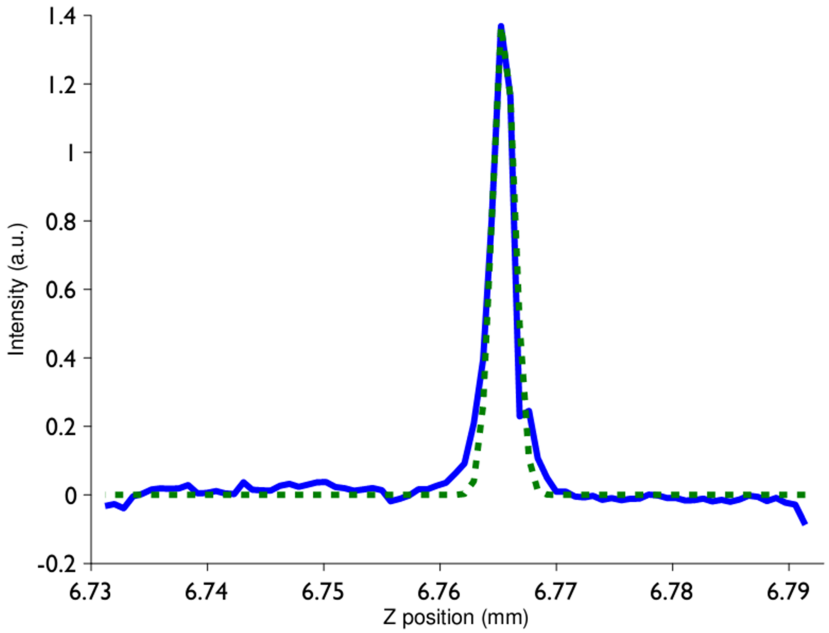

Figure 4.5: Typical focus scan of coverslip surface, $\lambda = 473$ nm, NA = 1.2. Sample plane position is estimated by fitting focus coordinates just outside the writing area.

of discrete stairsteps that form the phase ramp; reducing this number increases azimuthal

variation in the profile, but null depth remains unchanged. Offcenter SPP alignment in the beam and errors in the amount of phase wrap (design wavelength λ_{des}) seem to have the same general effect: asymmetric lobes appear around the null, but the null darkness is again retained.

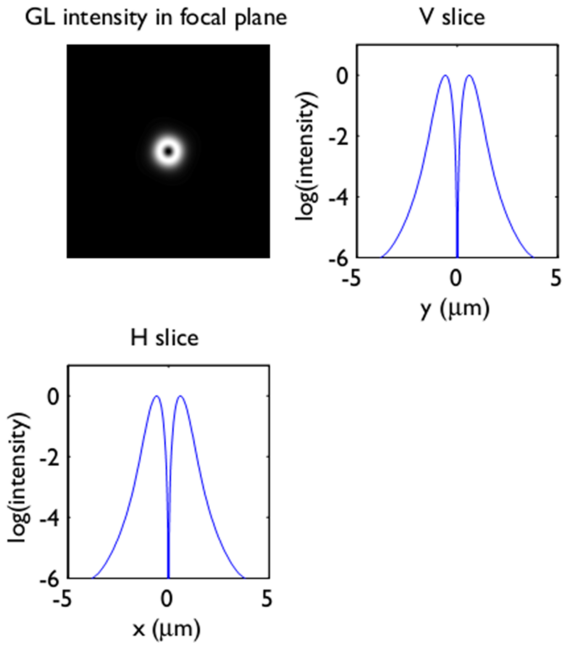

Figure 4.6: SPP: 16 steps, correct design wavelength, aligned in beam

Objective lens choice is crucial for achieving diffraction-limited visible and UV spots at the same axial focus. While it is not discussed much in the manufacturer literature, experience suggests that most modern oil-immersion lenses are only corrected in the visible. Many lenses may offer high UV transmission, especially those designed for fluorescence imaging, but several lenses tested (Olympus 1.4 NA / 60x PLAPON super chromatic aberration-corrected; Olympus 1.4 NA 100x UPLSAPO; Nikon 1.4 NA 60x CFI Lambda), performed dismally in gold nanoparticle PSF tests at $\lambda = 364$ nm, with focal spots several times broader than the diffraction limit. Since the numerical lens design is likely optimized by minimizing high-order polynomial functions within a parametric design space, it is perhaps unsurprising to observe wild performance deviations outside that design space. A 1.3 NA / 40x oil Neofluar from

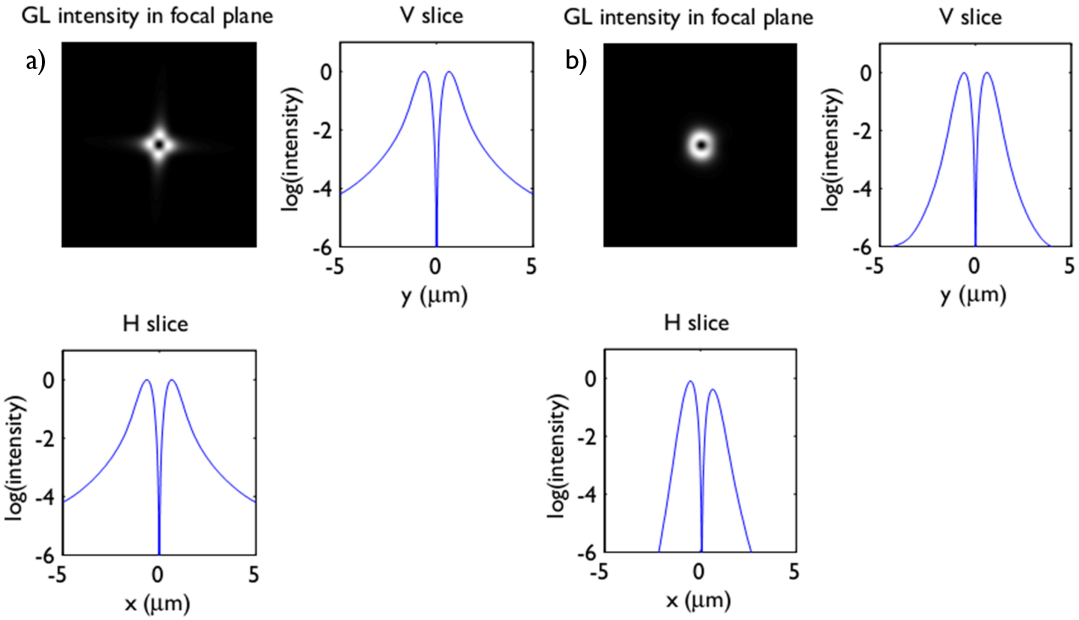

Figure 4.7: SPP: a) 4 steps, correct design wavelength, aligned in beam; b) 16 steps, 10% error in design wavelength. Misalignment in beam gives a similar effect. Note that relative null depth but not absolute null intensity is affected by these small errors.

Zeiss yielded a diffraction-limited PSF at $\lambda = 364$ nm, but the axial chromatic error between that focus and the $\lambda = 473$ nm focus was several microns. Zeiss Ultrafluar objectives are specifically designed for UV and visible correction; a 0.2 NA / 10x Ultrafluar and a rare 1.2 NA / 100x 365 nm glycerol Ultrafluar were obtained for this work, and diffraction-limited performance was demonstrated in the visible and UV.

Despite UV and visible corrected design, the Ultrafluar objectives have a small but measurable axial chromatic error between $\lambda = 364$ nm and $\lambda = 473$ nm, resulting in a $\sim$3 μm difference in focus. Slight decollimation of the blue beam, by linear-stage adjustment on the 2nd 4f steering-relay lens, corrects the error without significantly degrading the transverse PSF. Decollimation tuning of the blue is done by first precisely focusing the UV beam on a reflecting sample. Next, reflected blue light traveling back through the blue spatial filter is maximized by adjusting a linear stage holding the 2nd 4f mirror.

Figure 4.8: Zeiss Ultrafluar objective lenses, corrected in UV and visible bands.

4.2 Alignment

Beam angular tolerance required to maintain a stationary diffraction-limited spot in the focal plane is derived given just λ and the objective input aperture D. For the 1.2 NA Ultrafluar, D = 4 mm. At $\lambda = 364$ nm, angular resolution $\theta = 19$ arcsec. But the 0.2 NA Ultrafluar has a slightly larger input aperture of D = 6.5 mm, which gives $\theta = 12$ arcsec. Counterintuitively, transverse alignment is more difficult with the lower-NA objective. Angular adjustment resolution of 1/10 of a diffraction-limited spot or 1 arcsec is desired for fine alignment of the blue and UV beams, which is beyond the sensitivity of manual thumb-screw adjustment of mirror-mounts. Piezo-actuated Picomotors (New Focus) improve screw-angle resolution to 0.03 degrees and are remotely controlled, eliminating unwanted deflections from finger contact and improving beam steering resolution to 0.1 arcsec.

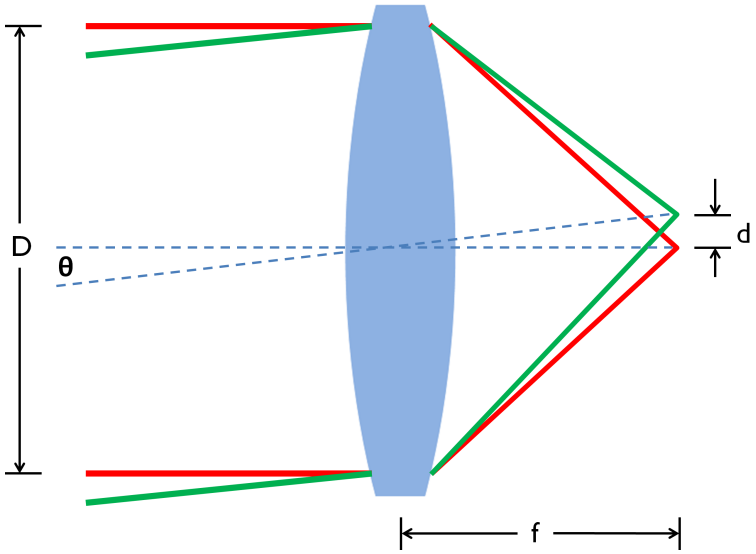

Figure 4.9: Diagram for angular sensitivity derivation, given lens aperture diameter D, NA and index n at the image plane.

$$d = \frac{\lambda}{2NA} \tag{4.1}$$

$$f = \frac{D}{2NA} \tag{4.2}$$

$$\tan\theta = \frac{d}{f} = \frac{\lambda}{D} \tag{4.3}$$

Use of ND filter wheels during an experiment can present alignment difficulties; Thorlabs reflective ND filters used in this system have a specified parallelism of < 0.03 arcmin, translating into as much as a 180 arcsec beam angle deviation as filters are switched. This is dealt with by placing the ND filter wheel near an adjustable steering mirror before the spatial filter and tweaking mirror tilt for maximum pinhole transmission with every ND filter change.

Relative position of blue and UV spots can be determined at high NA by imaging reflections from randomly dispersed gold nanoparticles at the focal plane. For this, a beam-

splitter, imaging lens and camera are installed in both beam channels before the steering relay. Gold nanoparticles (100 nm diameter, Sigma) are spin-cast from water onto a clean glass coverslip and inspected for distribution with a dark-field microscope. A droplet of photo-curable resin is placed on the same coverslip surface, which is laid face-down against a clean glass microscope slide with sticky-tape spacers. The resin is then cured through the glass with a UV lamp, rendering a layer of nanoparticles encapsulated by crosslinked polymer approximately index-matched to glass. The encapsulant resin is prepared by mixing ethoxylated bisphenol-A diacrylate (Sigma) with 0.5 wt% Lucirin TPO (BASF). As the sample is scanned past the objective focus, reflections from the gold particles are visible on the cameras. When a particle has been moved into the beam focus, a very bright reflection may be observed. To check that both blue and UV spots have been aligned to the same particle, it is useful to translate to a new particle and alternate beams; if a bright reflection is observed from one beam but not the other, the spots may have been aligned to different particles.

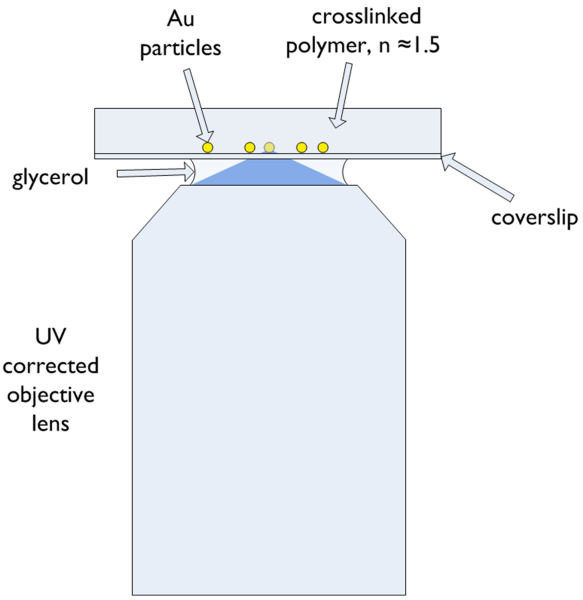

Figure 4.10: Alignment by reflection from gold nanoparticles on a coverslip surface, encapsulated by a crosslinked polymer that is index-matched to glass.

Alignment at both high and low NA can be done by making a small hole in a thin gold film with a focused UV beam, then steering the blue spot through it. For this, gold is sputtered on a clean coverslip until the coverslip is mostly reflective and only barely transparent. The coverslip is then mounted gold-down onto a glass slide with sticky-tape spacers and without resin, then secured at the edges to the slide with sticky-tape. The UV ablation / melting response is subject to a strong non-linear threshold effect, so brief flashes from a high-power beam are best for making a diffraction-limited hole. To monitor blue and (lower power) UV transmission through the hole, a photodiode may be mounted above the alignment target. Sticky-tape suspended above the alignment target provides a diffusive screen. Rough alignments may be done by eye and fine alignments using the continuously updated readout of a power meter.

4.3 Control and synchronization

Separate mechanical shutters from Vincent Associates (Rochester, NY) independently modulate the blue and UV beams. Two shutter types are used: the large-aperture VS series, capable of 20 ms pulses, and the small-aperture LS series, capable of 0.5 ms pulses. Shutters are driven by a Vincent Associates controller. Nanosecond modulation was demonstrated with acousto-optic modulators (AOMs) from Crystal Technology (Palo Alto, CA). Finite AOM on/off contrast was a limiting factor due to the step-and-wait nature of the writing system, which was dealt with by combining mechanical shutter and acousto-optic modulation on each beam-line. For simplicity, however, mechanical shutters are used without AOMs for general patterning experiments. Fast direct modulation is possible with the PhoxX diode laser, which may be useful in future work. Coarse adjustments to beam power are made with neutral-density filters, and fine adjustments via the laser controllers. This gives a combined beam power range of 36 nW – 3.2 mW at $\lambda = 473$ nm, and 360 nW – 12 mW at $\lambda = 364$ nm.

To avoid non-deterministic USB timing, shutters are signaled by an SR535 (Stanford

Research Systems) digital delay generator (DDG). The SR535 provides four programmable rising and falling-edge signals following a trigger, allowing for two independent pulses of arbitrary duration and delay. DDG programming and triggering is done via GPIB.

Precise sample positioning is accomplished with a Newport XPS XYZ-stage stack. Transverse control (horizontal, parallel to the sample plane) is by XMS 160 and 100 linear-motor stages rated for 10 nm minimum incremental motion, while axial control (vertical, normal to the sample plane) is by a GTS 30V rated for 100 nm minimum incremental motion. A Newport XPS controller receives commands via Ethernet from an experiment automation computer. XMS stages are slow but precise in step-and-expose dot-writing programs. The GTS 30V is specified for bidirectional repeatability of +/- 0.1 μm, which is well within the 350 nm DOF for $\lambda = 364$ nm light into a 1.2 NA objective. However, apparent bidirectional repeatability issues necessitated approaching z-positions always from the same direction, a method that increases experiment time somewhat but seems to successfully address the problem.

Writing station automation is implemented in MATLAB, using the Data Acquisition Toolbox and the Instrument Control Toolbox with VISA (National Instruments). Focus-detector levels are read via USB from a 1208 FS DAQ (Measurement Computing, Norton, MA). The SR535 DGG is programmed and triggered via a USB/GPIB adapter from (ICS Electronics, Pleasanton, CA). Coherent Innova 300C beam power is set via RS232, and the Newport XPS controller receives commands via Ethernet.

Ambient oxygen is an efficient inhibitor of radical polymerizations, and its removal is usually necessary for curing to proceed. In some configurations, a resin is sandwiched between barriers such as glass or gas-impermeable plastic. Oxygen can be removed by diffusion in a purged chamber prior to lamination, or by an optical pre-cure designed to consume oxygen but not the monomer. Bulk curing (e.g. dental composites) can be performed without barriers; the thickness of the resin protects all but a near-surface layer from in-diffusing oxygen. Single-photon-absorption fine patterning of resins requires the resin to be cast in

a thin film to eliminate out-of-focus exposure at high NA, and to limit the formation of tall (and possibly weak) structures at low NA. Oxygen exchange with ambient air is fast throughout an open-faced liquid thin-film, however, so a purge system is needed. This is accomplished by sealing the thin-film sample against a cavity and flowing ultrahigh-purity N2 through it; at a flow of 0.25 Lpm, a 1 cc cavity should reach 1 ppm oxygen in 15 s [124].

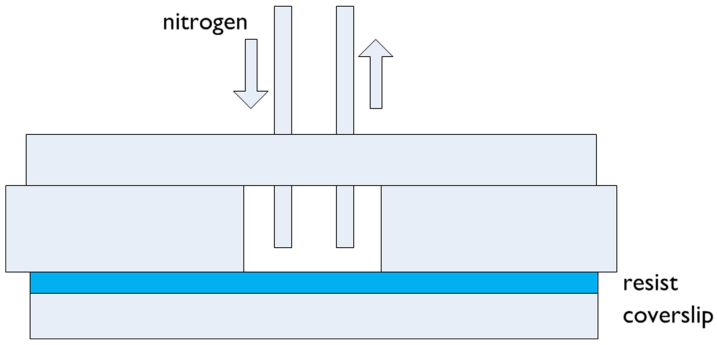

Figure 4.11: Sample holder with nitrogen purge. Writing and inhibiting beams are focused from underneath the coverslip into the resist thin-film.

One is generally advised never look directly into any laser beam, but as Innova 300C series lasers emitting in the ultraviolet are classified as Class IV, precautions are taken very seriously. Protective eyeglasses are always worn when the laser may be emitting; close-fitting wrap-around yellow-tinted glasses are preferred for comfort and protection from side-incident stray beams. Eyeglasses designed to block laser radiation are typically marked with optical density (OD) numbers in various parts of the spectrum, but protection can also be determined directly by measuring attenuation when eyewear is inserted in the beam. To protect others in the lab environment, a laser interlock is also used; a wall switch controls power to the 208VAC 3-phase receptacle supplying power to the laser. When the switch is on, bright red lights above the lab doors are illuminated.

Chapter 5

Photoinitiator evaporation

Upon completion of an effective purge system for resin thin-films, patterned results showed the unexpected effect of resin photosensitivity diminishing over time. This chapter describes the follow-on investigation and discovery of photoinitiator (camphorquinone) volatility, which up until now has not been recognized in the literature. Analysis of sorption kinetics is presented, in an attempt to quantify the evaporation effect. A technique is presented that gave stable photoinitiator concentration over time, a requirement for repeatable experiments.

Two important photoresist characteristics for radical-mediated PInSR lithography are a non-glassy state and thin-film geometry. Photogenerated pattern-transfer occurs through chemical reaction, resulting in a liquid-to-solid phase transition. The mobility afforded by a liquid or rubbery solid host allows the various photopolymerization reactions to proceed, unlike the case of a glassy solid where diffusion is negligible. In contrast, the cationic photoresists commonly used in semiconductor manufacturing are exposed in a glassy state; there, the photogenerated acid species is long-lived. A post-exposure bake (PEB) after exposure raises mobility enough to allow photoacid-catalyzed reactions. PInSR also requires a thin-film configuration to eliminate out-of-focus polymerization from single-photon absorption kinetics. Unlike two-photon or multiple-photon initiated patterning, which is axially isolated by a super-linear intensity response, single-photon patterning is linear or sub-linear and will tend to accumulate significant material change beyond the optical focus in a thick resin. Therefore

it is possible in PInSR to create dense patterns in a thick resin that cannot be recovered, due to the unavoidable polymerization of a blurred-image above the focal plane.

These two requirements are met by formulating a resin with viscosity high enough to resist dewetting from the substrate but low enough to allow polymerization. This has been accomplished by combining the non-reactive solid linear polymer poly(methyl methacrylate) (PMMA) with the non-viscous liquid triethylene glycol dimethacrylate (TEGDMA) monomer approximately 1:1, to make a negative-tone photoresist that can be spin-coated from cyclohexanone onto a glass coverslip. When this resin is spin-cast onto a methacrylate-functionalized glass, the resulting thin film refrains from dewetting for hours to days. The thicker a film is cast the longer it remains rupture-free, as expected.

5.1 Evidence for volatility

When camphorquinone (CQ) and tertiary-amine coinitiator (EDAB) are present in the pre-cast solution, patterns may be written into cast thin films by scanning the sample across the blue beam focus. This requires the sample to be mounted in a chamber purged of oxygen, which is a strong inhibitor of radical polymerization. The resulting crosslinked polymer stencil may be recovered by 20 s rinses first in cyclohexanone then methanol followed by nitrogen blow-drying. Photospeed, however, tends to diminish the longer the sample has been mounted in the purge. The observed effect is correlated with the total purge time and not post-exposure purge time, which eliminates causation by truncated dark-cure. Since diminishing photospeed is correlated with time in the dry nitrogen-purged chamber, it was initially believed that sensitivity loss was due to effects associated with decreased mobility, which resulted from either the loss of residual solvent or water. Cyclohexanone and water vapor were evaporated into the nitrogen purge upstream of the sample chamber over the course of several experiments, but the continual photosensitivity loss was not improved.

In an alternative approach, the resist was reformulated with another photoinitiator: 0.5 wt% Lucirin TPO instead of 1 wt% camphorquinone, and exposed to UV light within

the TPO absorption spectrum. Patterns developed from these experiments show no loss in sensitivity, pointing to initiator evaporation as the likely cause of diminishing photosensitivity. Given that CQ powder has a distinctive odor while the coinitiator EDAB has none, we hypothesized that CQ was volatilizing from the thin film. This hypothesis at first seems unlikely given the 200 °C melting point of CQ and an absence of literature on the topic. On the other hand, evaporation rates are generally proportional to surface area; small volatility that would go unnoticed elsewhere is detected more easily in thin films where the ratio of surface to volume is high.

I tested this hypothesis by attempting to volatilize CQ from solution and then trap it in another liquid. For this, three sealed 20 mL scintillation vials were connected in series by vinyl tubing as shown in Fig. 5.1. The first vial contained CQ in stirred TEGDMA, and the last vial contained stirred, neat TEGDMA. An empty vial between them served as a trap for any liquids or solid particles. A moderate flow of air was started through the assembly, and after 19 h the experiment was stopped.

Initial inspection revealed that the 3rd vial had turned from clear to yellow. While the shade of yellow was much lighter than the first vial, the color change was easily visible under room lights. The middle trap vial remained empty and dry. A UV-vis spectrum was taken of the light yellow liquid from the 3rd vial, against a background of neat TEGDMA. The obtained curve, shown in Fig. 5.1, exactly matches the distinctive absorption spectrum of camphorquinone. This hypothesis was also tested by attempting to add CQ vapor to the nitrogen purge stream before it passes through the sample holder. For this, nitrogen flow was routed through a scintillation vial containing ∼0.1 g of CQ powder as shown in Fig. 5.2, center.

5.2 Gas-phase delivery of photoinitiator to resin thin-films

In the next experiment a TEGDMA/PMMA resist was formulated with EDAB coinitiator, but no CQ initiator. A sample of it was spin-cast to 1.5 μm on a coverslip and

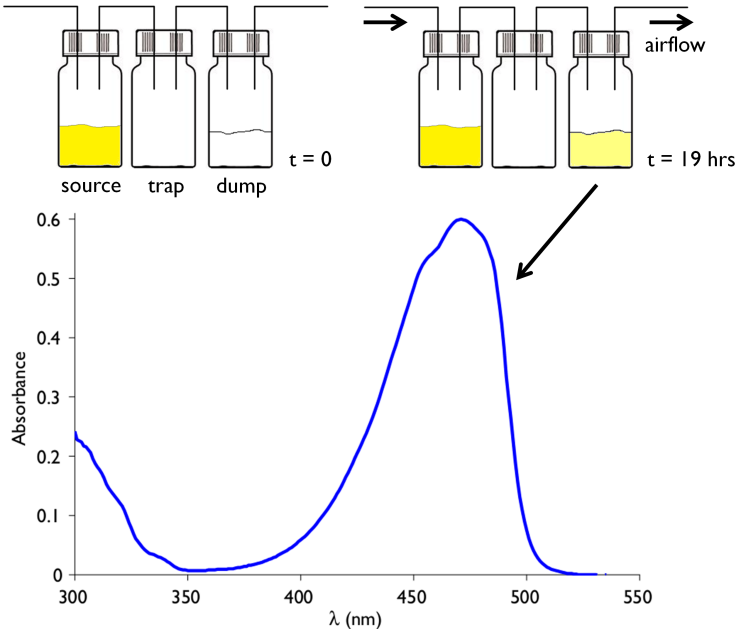

Figure 5.1: Top: diagram of bulk CQ volatility measurement. Initiator volatilized from a source solution migrates via forced convection to a dump. Bottom: UV-Vis absorption spectrum of dump after 19 hrs, exactly matching the known spectrum of camphorquinone.

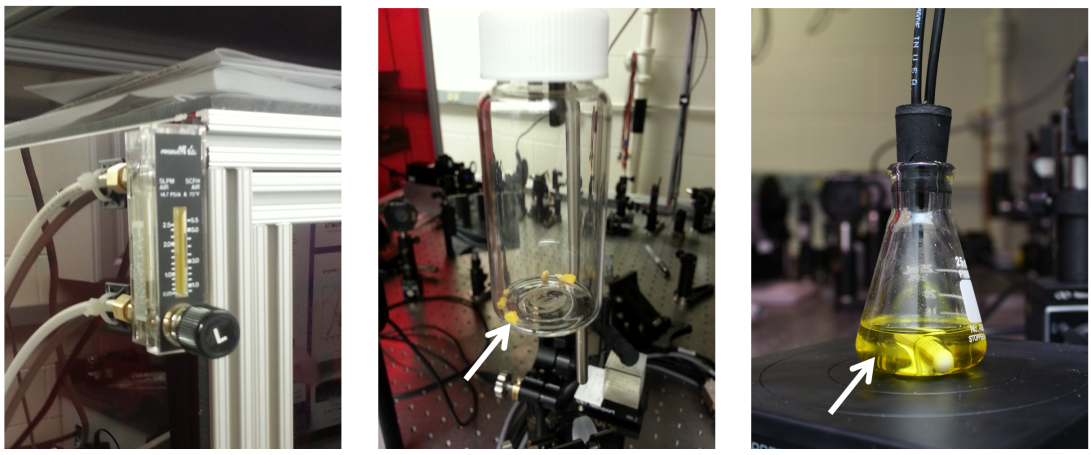

Figure 5.2: Left: flow meter used in this work, typically set to 0.25 Lpm. Center: camphorquinone (CQ) pellets in purge stream have an effect equivalent to ∼1 wt% CQ in formula. Right: CQ in solution with stir provides a constant surface-area for initiator volatilization

mounted on the holder. At $t = 0$, gas flow at 0.25 Lpm was started and a raster-scan of uniform optical exposures began; when the exposures stopped at $t = 33$ m the sample was immediately removed to atmosphere and rinsed in solvent. Microscope inspection of the

coverslip surface clearly showed a dot array, with faint or missing dots at the beginning and end as shown in Fig. 5.3.

The presence of as little as 100 mg CQ powder in the purge-stream resulted in a detectable CQ-odor at the exhaust, and excessive photosensitivity (see "chemical flare" below). While dry powder CQ in the purge-stream is effective, there are at least two problems associated with it: vapor concentration is not easy to adjust, and evaporation rate is a function of the effective surface-area of the powder - a quantity that both varies with sublimation / impurity concentration, and is inherently difficult to estimate. To address these issues, I vaporized CQ into the purge from a stirred liquid carrier solution (see Fig. 5.2). CQ vapor concentration is then controlled by solution concentration, and only slowly diminishes as CQ molecules evaporate from the constant surface-area at the bottom of the flask headspace.

Since the vast majority of exposed fluid in the vaporizer consists of the liquid carrier (solvent) itself, attention must be paid to solvent volatility and solubility to avoid unwanted swelling of the thin film. Inland 19 vacuum pump oil was successfully used as a CQ-carrier for much of the patterning work. Vapor pressure is specified to less than 10 μT at 25 °C, and large oil-droplets left on thin, uncured methacrylate films did not appear to dissolve the films at all. A possible complication of using this vaporizer solution is poor mixing of CQ. Even with agitation, darker yellow coloring observed at the top of the volume suggests CQ surface-enrichment. Plasticizers are another category of CQ carrier candidates, since they are engineered for very low volatility. The handbook by Wypych [239] is an informative reference: Dibutyl phthalate, which quickly dissolves CQ, has a measured vapor pressure of 1-2 $\times$ 10^{-5} T at room temperature. Trioctyl trimellitate has an impressively low estimated vapor pressure of 4 $\times$ 10^{-11} T. A paper by Hickman et al. is another useful reference here [100].

Similar experiments with TPO-initiated resists show uniform exposure response 10 s after starting the nitrogen purge, consistent with oxygen removal calculations shown earlier [124]. Since the response shown in Fig. 5.3 had still not stabilized 100 s into the same 0.25

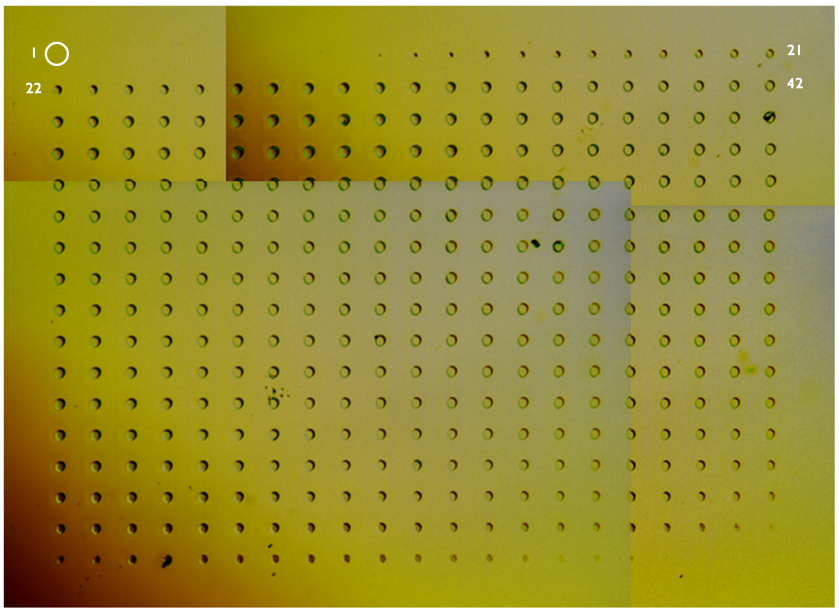

Figure 5.3: Composite DIC micrograph of a polymer dot array. Exposure (100 ms) occurred at a 4.5 s interval in a raster-scan with 100 μm square spacing, beginning immediately upon flow of nitrogen and CQ vapor. Dots 1-42 are missing or small due to incomplete CQ sorption; dots 315-441 (not shown) are small or missing to due incomplete dark polymerization.

Lpm purge, and since the film was formulated without photoinitiator present in solution, the upward ramp in dot size is taken to indicate increasing absorption of CQ vapor. Exposure response finally stabilizes at 150 s, indicating equilibrium CQ exchange between the film and the purge stream. Towards the end of the array the response begins to diminish, despite uniform conditions throughout the writing process. This is taken to be oxygen termination of post-exposure polymerization (dark cure), induced by removing the sample to room air. Decker [60] and others have observed this effect, though the dark-cure usually observed is typically shorter than the 10 m interval seen here.

Unexpected evaporation of one compound raises questions about similar effects with other species, and a cursory investigation suggests that it does occur. In one experiment, dry CQ powder was weighed after being placed in a 100 mT vacuum for 30 m. The sample was then returned to the vacuum for another 10 m and then removed again to be re-weighed.

The co-initiator EDAB and photoinhibitor TED were processed similarly. Results showed a normalized mass-loss in the EDAB sample about 10% the loss observed in the CQ sample. Slight volatility was also observed in the TED sample, though it amounted to only 1% of the loss observed in the CQ sample. A TPO-formulated thin-film resist sample was photopatterned and left in a nitrogen purge overnight. In the morning, it was photopatterned again in a different region then removed and developed. Inspection of the arrays clearly showed loss in photosensitivity after the overnight purge. Evaporation of TEGDMA has not been quantified in this work, though evidence for it has been observed. Films consisting of TEGDMA and PMMA (1:1 by weight) were spin-cast on glass to a thickness of 1 μm, and left in an oven overnight at 60 °C. The thermal treatment caused the soft and rubbery films to become glassy. Since ambient oxygen strongly inhibits radical polymerization in thin films, the modulus change is most likely due to preferential evaporation of the monomer over the 120k PMMA. In the absence of extended incubation at elevated tempertures, TEGDMA-PMMA films remained relatively soft for several days.

A related phenomenon has been observed in commercial photoresist processing, known by the term chemical flare [232]. There, photogenerated acid volatilizes during the post-exposure bake and re-deposits elsewhere causing unwanted haze and blurring of patterns. Interestingly, the flare can be prevented with the use of a top antireflection coating [35]. A similar effect may occur in volatilized CQ radical photopolymerizations, as shown in Fig. 5.4. Whether or not it is noticed, evaporation of other "non-volatile" species is likely in many applications with high surface-area-to-volume ratio. Even glassy polymers may experience unexpected evaporation or absorption, though low mobility will tend to limit the effect to a thin layer near the surface.

5.3 Sorption kinetics

Two physical processes control initiator sorption: diffusion to and away from the surface, and evaporation or absorption between the surface and ambient. Mass transport to

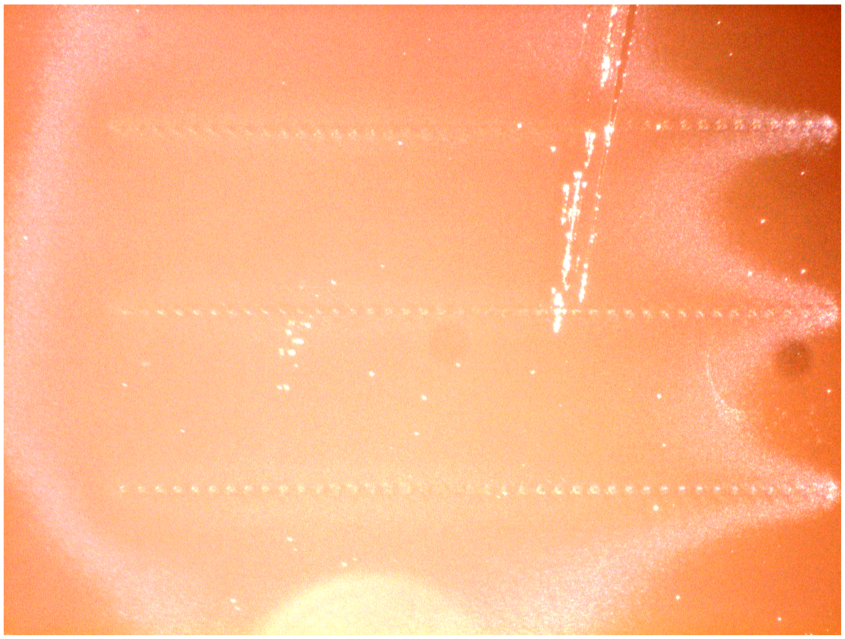

Figure 5.4: Haze effect in TEGDMA/PMMA film, exposed with ∼1 g CQ present in the purge inlet stream. This is possibly related to the chemical flare observed by Brunner et al. [35], where photogenerated acid evaporates and redeposits in unexposed areas.

the surface may be modeled by one-dimensional Fickian diffusion, where the characteristic diffusion length $L = 2\sqrt{Dt}$, where D is diffusivity and t is time. Fluorescence recovery after photobleaching (FRAP) measurements of TEGDMA/PMMA resist give small-molecule D = 0.25 $\mu m^2 \cdot s^{-1}$, which can be incorporated into a kinetic model. For example, solving the diffusion length equation for a 1.5 μm film gives a characteristic diffusion time of 2.3 s. Since observed initiator evaporation takes 2 – 3 min, evaporation is likely controlled by another mechanism.

Evaporation generally cannot be predicted from the boiling point [102]. De Heen [58], however, was able to show that the evaporation rate of various organic liquids is approximately proportional to the product of vapor pressure and molecular weight. This finding is successfully reproduced and summarized by Hofmann in [102]. Since there appears to be no available experimental data on the volatility of CQ at room temperature, I use de Heen's method in reverse to estimate CQ vapor pressure from evaporation measurements.

Evaporation of monomeric plasticizer from a polymer thin-film is treated by Smith et al. [208]. While very low volatility is a feature of most plasticizers, evaporation does occur and is especially evident in thin non-glassy films. But depending on mobility, evaporation from a polymer film may also be limited by species diffusion to the surface. Smith et al. use neutron scattering to measure plasticizer concentration through depth and apply a diffusion analysis described by Crank [51] to model evaporation. In that work, equilibrium plasticizer distribution is not uniform through the film thickness; it tends to accumulate in greater concentration at the substrate/polymer and polymer/air interfaces. This surface enrichment effect is apparently due to surface energy and free energy balance, and is significantly diminished at lower plasticizer concentrations. For the sake of simplicity, I disregard possible surface enrichment here.

The boundary condition for evaporation across a surface can be represented as

$$-D\,\partial C/\partial z = \alpha(C_0 - C_\mathrm{s}) \tag{5.1}$$

at $z = 0$, where C_0 is the local concentration just inside the boundary, C_s is the equilibrium concentration with the ambient environment and α is the evaporation coefficient. Given a thin sheet with thickness $l < z < l$ and applying the boundary condition at each surface, concentration C is solved below given initial uniform concentration C_2 and ambient equilibrium concentration C_0 as shown by Crank [51]:

$$\frac{C - C_2}{C_0 - C_2} = 1 - \sum_{n=1}^{\infty} \frac{2L\cos(\beta_n z/l)exp(-\beta_n^2 Dt/l^2)}{(\beta_n^2 + L^2 + L)\cos\beta_n}, \tag{5.2}$$

where α is evaporation rate and D is diffusivity. β_n are the positive roots of

$$\beta\tan\beta = L \tag{5.3}$$

and L is the dimensionless quantity

$$L = l\alpha/D, \tag{5.4}$$

that indicates whether mass-transfer is diffusion or evaporation-limited.

Note that while the above solution is for evaporation from both sides of a sheet with thickness $2l$, the solution is identical for a sheet of thickness l bounded by an impermeable substrate on one side; the zero-flux condition at $z = 0$ is met in both cases.

Integrating the expression above to obtain total mass contained in the sheet gives

$$\frac{M_t}{M_\infty} = 1 - \sum_{n=1}^{\infty} \frac{2L^2\, exp(-\beta_n^2 Dt/l^2)}{\beta_n^2(\beta_n^2 + L^2 + L)}. \tag{5.5}$$

This is plotted in Fig. 5.5. When L is significantly less than unity, sorption or desorption is limited by diffusion away from or towards the surface; when L is significantly greater than unity, rate of surface adsorption or evaporation is the limiting factor.

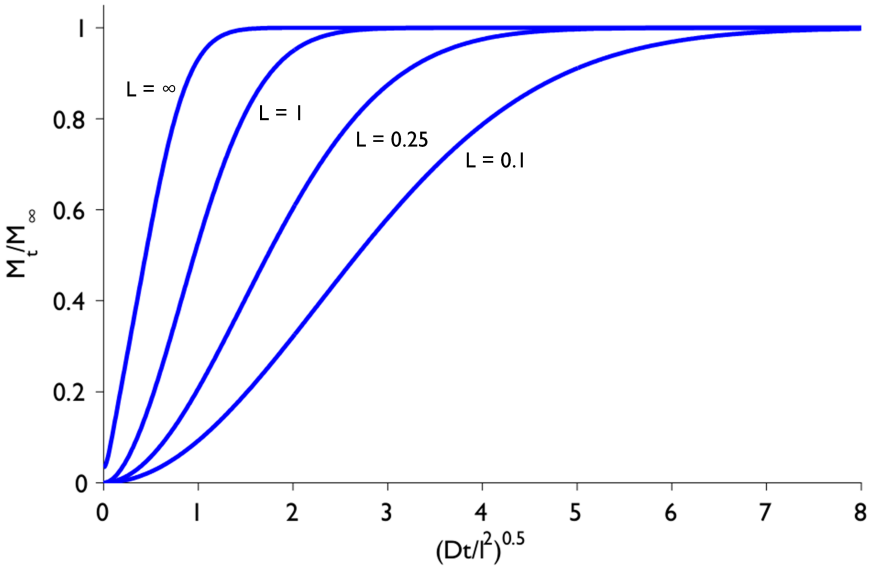

Figure 5.5: One-dimensional mass sorption or desorption relative to equilibrium concentration. For high L, mass gain or loss is limited by diffusion to the boundary; for low L, it is limited by transfer across the boundary.

Polymer dot diameter and optical exposure are seen in this work to have a roughly linear relationship [75]. While the basis for this is not yet understood (I speculate on it in Chap. 6), simply accepting the empirically-demonstrated relationship along with irradiance / initiator-concentration reciprocity enables measurement of the relative initiator concentration. In Fig. 5.6, experiment and model are compared for initiator absorption into a 1.5 μm resist film

with 0.25 $\mu m^2 \cdot s^{-1}$ diffusivity. Although the apparent subzero y-intercept seems to indicate a thresholding effect (probably due to residual oxygen or the gel threshold), this is ignored to simplify the model. The best-fit evaporation rate (obtained by iterative adjustment) is $\alpha \approx 30$ nm/s. Since the initiator is dissolved in solution and must diffuse to the surface to evaporate, this unit is physically meaningful as evaporation from an equivalent (though imaginary) neat, free liquid.

Using the simple evaporation rate estimate from de Heen, we can attempt to estimate the vapor pressure of camphorquinone at room temperature. For this we need a reference to establish the empirical constant K in Eq. 5.6:

$$\alpha(K) = M(P). \tag{5.6}$$

To do this, a methanol sample was first weighed and then evaporated from a closed container in a 20 °C water bath, using the same purge rate as the CQ uptake experiment. After evaporation it was weighed again, with the evaporation rate calculated to be 5.82×10^{-4} $g \cdot s^{-1}$. Methanol specific gravity is 0.791, which gives $\alpha = 7.36$ $\mu m^2 \cdot s^{-1}$. With molecular weight 32 and 20 °C vapor pressure of 96 mmHg [55], the experimental calibration parameter K = 417. Using experimentally-fitted $\alpha = 0.030$ $\mu m^2 \cdot s^{-1}$ for camphorquinone and a molecular weight of 166, we obtain a RT vapor pressure of 0.08 mmHg. This is a remarkable match to the predicted value of 0.1 +/- 0.4 mmHg at 25 °C[1] .

Fig. 5.8 shows concentration as a function of depth in the 1.5 μm TEGDMA/PMMA film. Due to fast diffusion within the film, initiator distribution is nearly uniform during the entire uptake period. This is in contrast with the curves presented in Fig. 5.9, showing concentration as a function of depth in the 100 nm UDMA-IPDI film. There, dramatically lower mobility causes steep gradients in depth-resolved initiator concentration during the uptake period. At the same time that total uptake begins to flatten, as shown in Fig. 5.7, the depth-resolved concentration shown in Fig. 5.9 begins to flatten as well.

[1] ACD/Labs PhysChem Suite

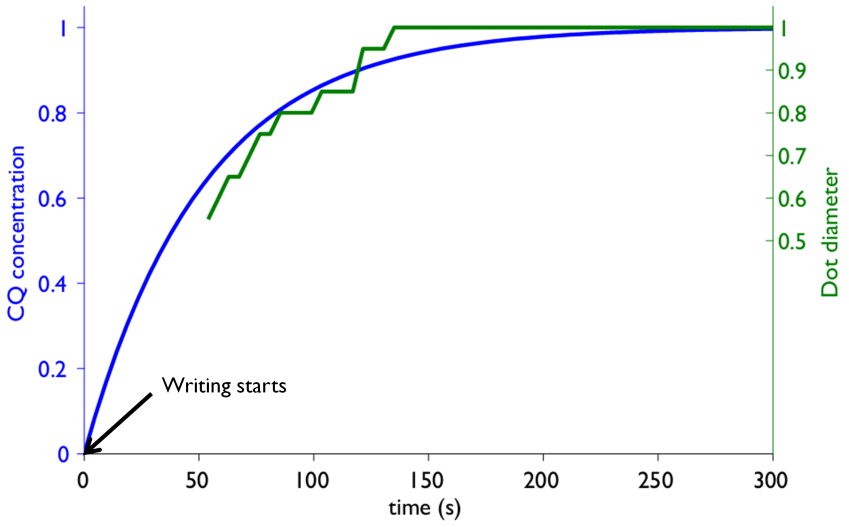

Figure 5.6: Initiator absorption into resist film, model and experiment. Polymer dot diameters are shown in green, starting where they first appear at a position corresponding to $t = 50$ s. Mass absorption (from Eq. 5.5) is shown in blue, with model inputs of film thickness 1.5 μm, diffusivity 0.25 $\mu m^2 \cdot s^{-1}$ and evaporation rate $\alpha = 0.030$ $\mu m^2 \cdot s^{-1}$.

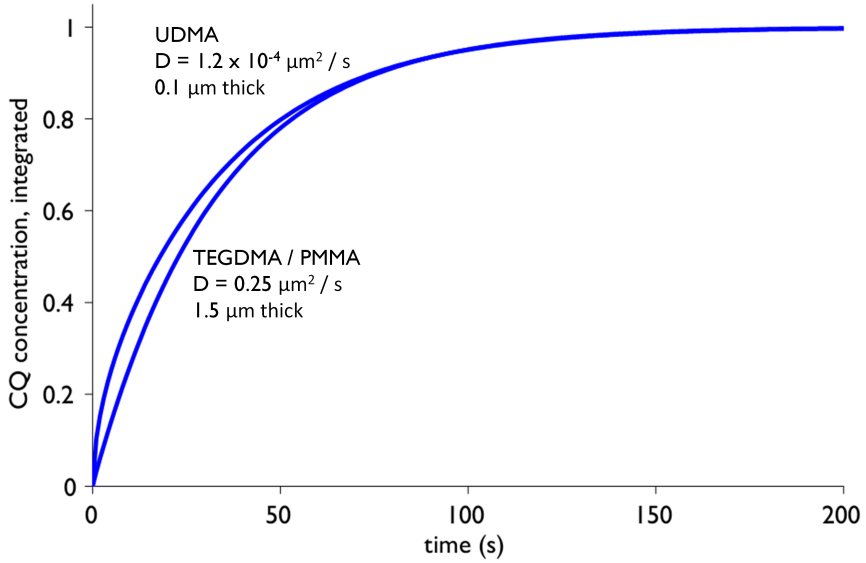

Figure 5.7: Initiator uptake profiles of a 1.5 μm thick TEGDMA/PMMA film and a 100 nm thick isophorone urethane dimethacrylate (UDMA-IPDI) film, both used in this work, are modeled in Fig. 5.5. Despite the similarity in total mass uptake, modeled initiator distribution during the uptake period is markedly different in the two films (shown below).

With some changes in design and materials, fast time-resolved control of camphorquinone concentration could be demonstrated with this system. Approximately 1.2 m of 2 mm ID nylon 11 fuel tubing was used for transfer between the vaporizer cell and the sample holder, constituting 75 cm^2 and the vast majority of surface area in the system. A calculation based on analysis from Ohring [177] estimates 100,000 collisions between an average N_2 molecule and the tubing walls, for our typical 0.25 Lpm flow rate. Thus there is ample opportunity for surface adsorption and even bulk absorption into the nylon, slowing the time constant of vapor modulation. Results from related work suggest the purge system is best run overnight through a closed sample holder prior to running an experiment, for maximum stability in vapor-controlled initiator concentration. The use of stainless-steel inner walls and shorter line lengths could help make a system with near-instantaneous vapor delivery to a thin-film sample.

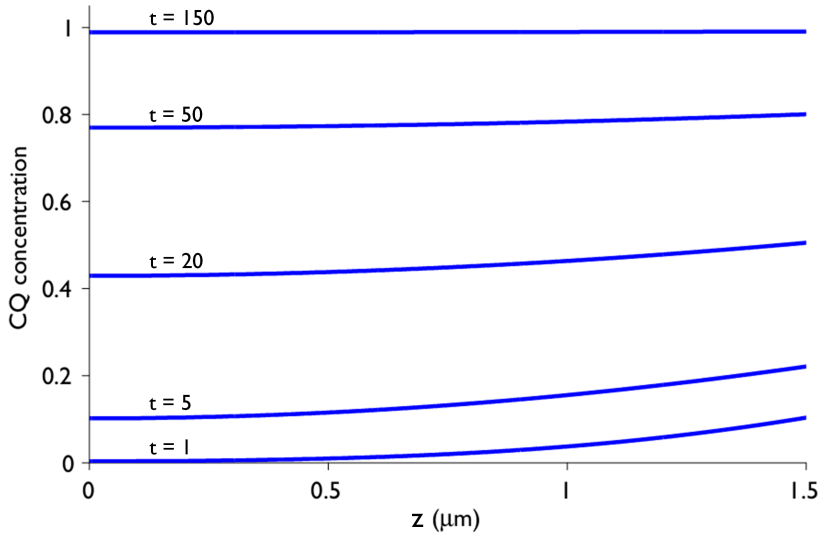

Figure 5.8: Depth-resolved initiator concentration in a 1.5 μm TEGDMA/PMMA film. At L = 0.3, initiator uptake is limited by the volatility of CQ.

There is precedent in exploiting volatility for patterning and polymerization. Tsao et al. [222] demonstrated direct-initiation UV laser patterning of surface-adsorbed methyl-

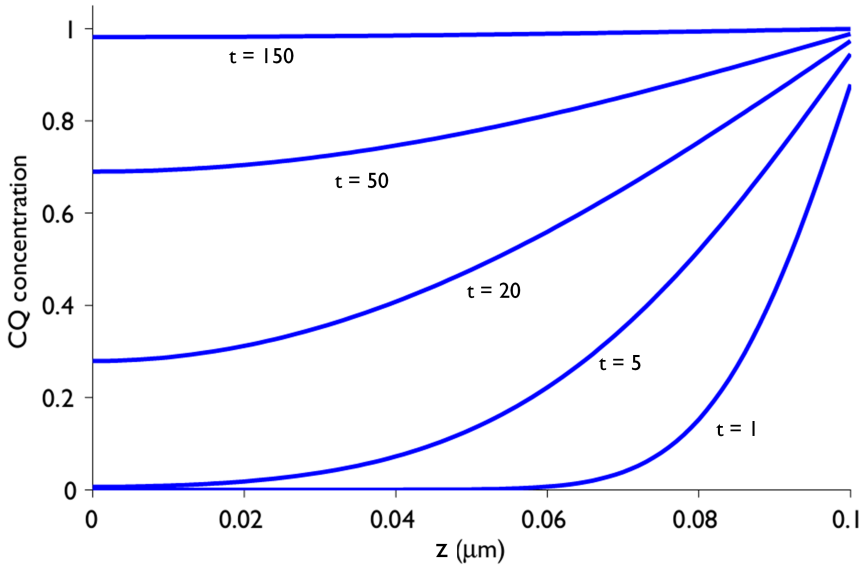

Figure 5.9: Depth-resolved initiator concentration in a 100 nm UDMA-IPDI film. At L = 42, initiator uptake is limited by mobility in the viscous resin.

methacrylate monomer. Neckers et al. [168] describe using borane-based vapor as a radical initiator to remotely cure resin. Chan and Gleason [40] performed near-UV patterned chemical vapor deposition (CVD) by combining vapor-phase initiator and monomer. To my knowledge, this is the first discussion of in-situ photopatterning with an initiator under vapor-phase control.

Applications for vapor-phase control of photosensitive media could include lithography, sensing and chemical screening. Removal of initiator from a film has a desensitizing effect, and could allow storage under ordinary room-lights. Consumption of species during exposure and polymerization could be replenished through the vapor phase, volatile waste products removed by desorption. Many formula combinations could be screened within the same sample, multiplexing spatial optical exposure with time-varying species concentration of initiator, inhibitor, monomer, fluorescent tags and other species.

Chapter 6

Patterned photoinhibition, radical diffusion and superresolution

The high optical intensities and short time-scales needed for high-throughput direct laser writing (DLW) are foreign to analytic methods used in polymer labs. Patterning is therefore necessary not only for demonstration, but also for fundamental experimentation and understanding. This chapter covers my initial work in high-NA photoinhibition, and the disappointing result that optically-sharp inhibiting-beam exposures can yield a highly blurred distribution of photogenerated radical scavengers. I discuss this result in terms of diffusive mass-transport, and propose using highly viscous resin to contain photogenerated species. Encouraging results are shown in this new resin, with 3× superresolution demonstrated at low NA. Furthermore, spot-walkoff tests suggest that similar superresolved patterning may be possible at high NA.

Initial PInSR materials development relied on large-area, low irradiance, extended-exposure experiments with FTIR spectroscopy and dynamic modulus analysis, where the irradiance levels were similar for both wavelengths tested [202]. The characteristic scales of direct-write lithography, however, are much more extreme: submicron lengths, $\sim$MW$\cdot$cm^{-2} optical irradiances and millisecond to nanosecond exposure times. Since radical-based flash photopolymerization is a non-linear process and simplifications such as the steady-state approximation are not necessarily justified, experiments on PInSR materials are best implemented in the DLW configuration itself.

6.1 Spot photoinhibition in a viscous resin

To test photoinhibition in a DLW configuration, I first developed a resist formulation based on the original formulation by Scott [202]. Starting with the 2-color resin containing CQ, EDAB and TED dissolved in TEGDMA monomer, I added PMMA (120k, Sigma) at a ratio of 1:1. To assist the process, acetone was added and later evaporated away, leaving a soft and gum-like solid material. To enable spin-casting, 3 parts cyclohexanone (instead of acetone) were added to 1 part resin formula. Cyclohexanone works well as a spin-casting solvent for many of the (meth)acrylate resins I evaluated. As with acetone, it is a good solvent for nearly all materials discussed here. It also evaporates at a relatively slow rate, which is crucial for spin-casting smooth films and avoiding the orange-peel effect. Particulate contamination, which can form nucleation sites that induce film dewetting, was removed with a 0.2 μm syringe filter.

Films with a thickness of 1–2 μm were spun onto acrylic-functionalized glass slides and then mounted in an oxygen-purged environment on the direct write station shown schematically in Fig. 4.2. Dot arrays were written, moving the sample with a precision stage and modulating the beams with a mechanical shutter. Arrays consisted of alternating rows of blue-only and blue+UV illumination, increasing in exposure time column by column. Samples were developed by 2-stage cyclohexanone and methanol rinse, and blown dry with compressed gas.

Resin exposure to the inhibiting beam must be balanced between two extremes: When the exposure is too short and/or the spot irradiance too low, the photoinhibition effect is too weak to enhance polymerization spatial confinement and no superresolved patterning is possible. When the exposure is too long and/or the spot irradiance too high, polymerization is induced by the inhibition beam itself that also prevents superresolved patterning. As discussed in Chap. 3, photoinhibition efficacy can be quantified ratiometrically by comparing polymerization rates with, and without co-exposure to the inhibiting beam. I refer to this

ratio as photoinhibition contrast (PIC).

When photocuring is monitored with FTIR spectroscopy, photoinhibition contrast can be obtained directly from the slope of the time-resolved conversion profile. In the small-spot limit where FTIR spectroscopy is impractical, photoinhibition contrast can be indirectly estimated by comparing the minimum writing-spot exposure duration required to gel the sample with, and without co-exposure to the inhibiting spot. Examining [202], FTIR conversion experiments in TEGDMA resin show that PIC ≈ 5. In results from a thin-film, small spot photoinhibition experiment depicted in Fig. 6.1, PIC ≈ 10.

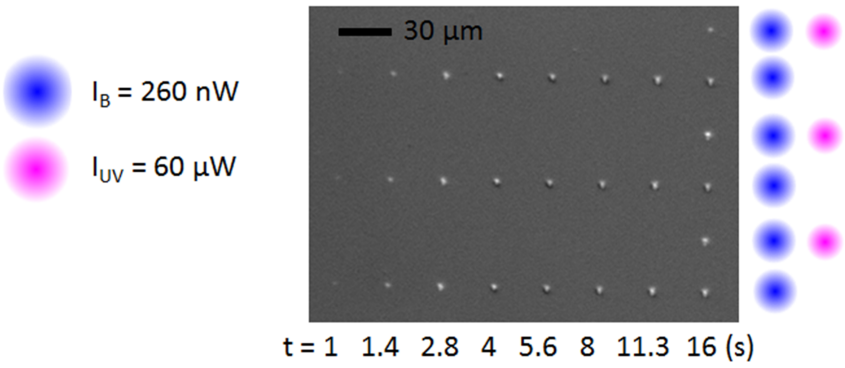

Figure 6.1: A DIC microscope photo of dots written and inhibited with Gaussian (G) blue and G-UV beams, focused onto a spun PINSR photoresist through a 0.25 NA microscope objective lens. Exposure time is multiplied by $\sqrt{2}$ with each column from left to right, and the exposure conditions alternate from blue-only to blue+UV with each row. Three pairs of rows are shown to demonstrate repeatability. For the 3 blue+UV rows, only the rightmost dot is visible.

This is a somewhat surprising result, considering the absence of observed photoinhibition in viscous resins discussed earlier. A simple explanation is that the FTIR photocuring experiments are practically limited in the ratio of UV to blue irradiance. If time-resolved polymer conversion trials of the viscous resins could be repeated with $50\times$ the UV irradiance (taking care to not heat the sample), perhaps photoinhibition would be observed. Another explanation is that high irradiance fundamentally alters polymerization kinetics, in a way favorable for photoinhibition control. To the extent that high resist irradiance is required

for effective photoinhibition, DLW is the preferred configuration for PInSR lithography.

With other STED-inspired superresolution lithography techniques, a significant challenge is the degree to which the material response to one color of light can be inhibited by the other color. Absorption contrast limitations in thin-film photochromics [7], and difficulties in initiator de-excitation [213], are examples of this. With radical-based photoinhibited superresolution (PInSR), however, the inhibition response shown above should be strong enough to demonstrate patterning well below the diffraction limit [76]. Indeed, at least three published investigations claim to have achieved superresolution with this technique. But a close inspection of these results raises some questions about the validity of the claims, a topic which will be addressed later in this chapter. In the next section I will discuss unsuccessful attempts at superresolved patterning, and my subsequent investigation into the underlying kinetic and diffusion issues.

With focused spot exposures, I confirmed in various methacrylate resins that knob-shaped polymer dots (Fig. 6.2) may be formed with dimensions matching or even smaller than the full-width half-max (FWHM) of the focused blue Gaussian (G) spot. But in this regime polymer dot size is observed to be an approximately linear function of exposure time, meaning that over-exposures can result in gelled dots with significantly larger diameters. Considering the exponential decrease of the optical PSF with transverse distance, this result is somewhat surprising and suggests that feature confinement at high NA is controlled by diffusion and not optical resolution.

The photoinhibition effect may readily be observed by removing the phase plate, superimposing a bright-centered UV spot on the blue spot, and adjusting the UV intensity to cause an increased exposure time required to gel dots in the sample (Top, Fig. 6.2). Smaller and more-defined dots result from sufficiently long UV spot exposures, possibly due to a more tightly focused optical spot and to the termination of out-diffusing carbon-centered radicals by UV-generated dithiocarbamyl (DTC) radicals. Larger and less-defined dots sometimes result from a shorter exposure to superimposed blue and UV spots, which possibly indicates

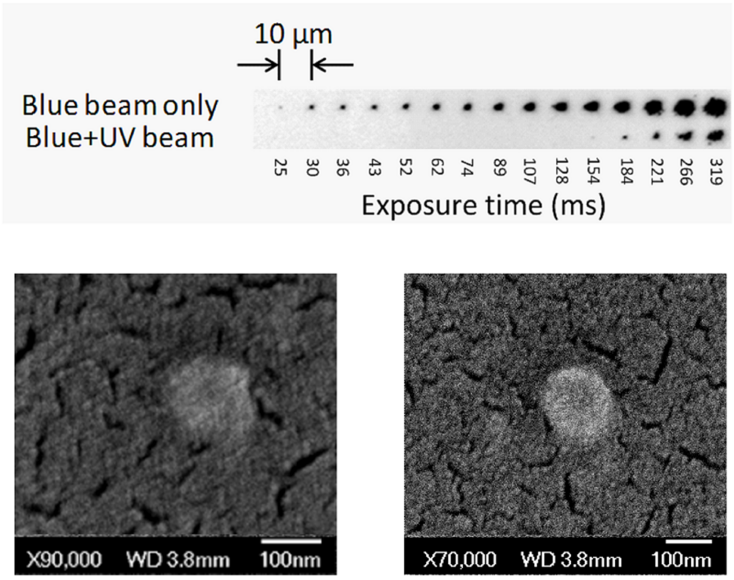

Figure 6.2: Photoinhibition and minimum feature sizes for blue plus donut-shaped Gauss-Laguerre (GL) UV exposures in a resist [76], spun onto a coverslip in an O_2-free chamber. Top: contrast-reversed darkfield microscope image of two rows of polymer dots on glass; optical exposure time increases from left to right. The upper row is exposed to a blue-only spot, the lower row to superimposed G-blue and G-UV spots. Superimposing the UV spot increases the minimum required blue exposure to gel the sample by more than a factor of 7 ($P_{\mathrm{B}} = 350$ μW, $P_{\mathrm{UV}} = 390$ μW). Bottom: SEM images of the smallest polymer dots formed *with* (right) and *without* (left) a GL-UV beam. Although the GL-UV spot causes an increase in the exposure time required to gel a dot, the dots are not smaller than the smallest ones fabricated with blue light alone ($P_{\mathrm{B}} = 40$ nW, $P_{\mathrm{UV}} = 450$ nW, exposure time $\tau = 1 - 2$ s). This indicates that the pattern of inhibitors created by the GL-UV beam may not be patterned over the polymerization timescale. All dots in this figure are fabricated in an open-top film purged with nitrogen, on a coverslip substrate with no reflective gold layer. The resist contains the same photochemistry (see Fig. 6.1 in a viscous 1:1 solution of triethylene glycol dimethacrylate (TEGDMA) and poly(methyl methacrylate)-120k (PMMA).

that smaller and faster-diffusing radicals are dominating prior to gelation.

6.2 No evidence for enhanced confinement with GL-inhibition

A similar photoinhibition effect is also apparent when the spiral phase plate is replaced and the dark center of donut-shaped UV spot is aligned with the bright center of the blue spot. By comparing the dimensions of dots fabricated without the GL inhibiting beam to

those fabricated with it on, I expect to observe the enhanced polymer confinement required for superresolution patterning. What is actually observed, however, is an unchanged polymer confinement; the smallest dots fabricated with the superimposed G-blue and GL-UV spots are the same size as the smallest dots fabricated with G-blue spots alone (Bottom, Fig. 6.2), which is rather disappointing. The increased exposure time-to-gel associated with the UV photoinhibition is observed, but the effect appears to be equivalent to lowering the power of a blue-only writing beam; instead of enhancing confinement of polymer dots, the addition of the UV spot reduces polymerization efficiency.

Failure to observe enhanced feature confinement prompted me to investigate the fundamental spatial and temporal characteristics of the PInSR system. Since I was not able to observe features significantly smaller than 100 nm fabricated from the resist described in Fig. 6.1, I decided to investigate the material system for which the best results had been reported: an ethoxylated (2) bisphenol-A dimethacrylate (E2BADMA) resin used by Gu et al. to achieve 40 nm dots [38]. The resin has a viscosity $\eta = 1100$ cP @ 25 °C, and contains the same photochemistry (CQ, EDAB and TED) as the original work [202] (Fig. 6.1). With respect to the optical system, the measured relative position and profile of the beams are reasonably well characterized; spot dimensions (FWHM) as measured with gold nanoparticles are $d_B = 290$ nm and $d_{UV} = 240$ nm, with spot alignments better than 50 nm. In Fig. 6.3, polymer dot size is an approximately linear function of exposure time. Given exposure to an optical spot with Gaussian distribution $y = Ae^{-x^2}$ and assuming steady-state polymerization with constant gel-threshold, we see by inspection that a $10^{14}\times$ increase in exposure would be required to achieve the $7\times$ increase in gelled-dot diameter seen in Fig. 6.3. The most reasonable hypothesis is that diffusion spreads primary and propagating radicals over a profile at least a few μm wide in E2BADMA, and optical exposure merely controls the amount of the profile above the gel threshold. The following experiment supports this hypothesis by confirming diffusional blurring of the patterned radical scavengers.

With the spiral phase plate removed, superimposed G-UV and G-blue spots are used to

write a column of dots where the exposure time increases along the column. The next column is the same but now the spots have been transversely offset. The third column has twice that offset, and the forth column three times etc. The photoinhbition effect of the UV spot diminishes with increased offset with the blue spot, but much more slowly than expected; a spot centroid transverse offset of 1.1 μm is required to decrease the photoinhibition contrast by half (dotted line, Fig. 6.4). Here I define photoinhibition contrast (*PIC*) as $PIC = \tau_{\mathrm{B}}/\tau_{\mathrm{B+UV}}$, where τ_{B} is the minimum exposure time to gel the dot with the inhibition beam off, and $\tau_{\mathrm{B+UV}}$ is the minimum exposure time to gel the dot with the G-inhibition beam on. This wide radius of measured inhibition is an order of magnitude larger than the optical spot that generates it. This indicates that the photoinhibition effect has spread significantly beyond the extent of the UV PSF in the time scale of polymer gelation. This in turn suggests that the donut-shaped DTC$\cdot$ distribution has blurred-out; radical diffusion rate is too fast relative to the polymerization rate for enhanced polymerization confinement at this spatial scale.

From the real-time FTIR studies of photopolymerization by Decker [60] of short exposures to intense laser beams, I see that the majority of the conversion may occur after the exposure, over longer intervals in the dark (so-called dark cure or dark polymerization). To obtain an estimate of the minimum time-to-gel, I use a variable delay of the UV exposure relative to the blue exposure. With sufficient UV delay, the photoinhibition effect is not observed; I then use this delay as an estimate of the minimum time to gel. Relative to simultaneous exposures (no UV delay) the photoinhibition contrast is observed to fall by 75% within the 0.5 seconds, the minimum delay implemented. With a delay of more than 2 seconds, no change in photoinhibition is observed. Since no photoinhibition effect is possible in the dot after it gels, I take 2 seconds as a minimum time to gel for the given exposure. To our knowledge, this is the first time dark-cure intervals have been estimated in direct-write lithography, although similar measurements have been done for holography [165].

6.3 Observation of diffusional blurring of photogenerated inhibitor

To achieve well-defined superresolved polymer features, the photoinhibitor concentration must retain the profile of the UV optical spot for at least the gelation time interval. I must thus compare the measured gelation time to the DTC radical diffusion time into the dark UV null. Figure 6.4 indicates diffusion of DTC radicals sufficient to reduce contrast by 50% over a distance of approximately 1 micron in the gelation time, indicating that the diffusion time across the approximately 100 nm PSF may be a factor of 100 smaller than the gelation time. As direct measurement of the DTC radical diffusivity is difficult, I substitute the DTC radical with a fluorescent molecule of similar size and measure its diffusivity via fluorescence-recovery-after-photobleaching (FRAP) [14].

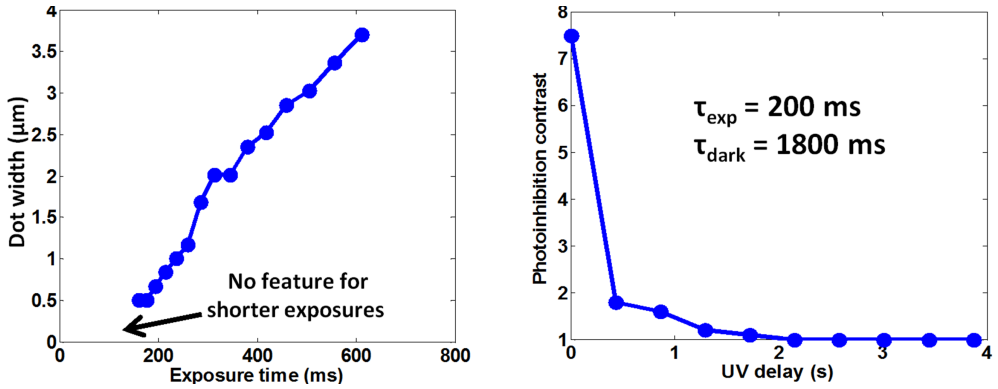

Figure 6.3: Measurement of PInSR dynamics with blue and UV spot exposures. Left: the polymer dot width is an approximately linear function of exposure time ($P_{\mathrm{B}} = 4.1\ \mu$W). Right: blue and UV exposures are staggered in time to estimate the lower limit of the dark polymerization interval. For small gelled features resulting from a 200 ms blue exposure, the photoinhibition effect is observed as long as 2 seconds later ($P_{\mathrm{B}} = 4.1\ \mu$W, $P_{\mathrm{UV}} = 130\ \mu$W, τ = 100-600 ms).

Adding 7-mercapto-4-methylcoumarin to the monomer causes visible fluorescence to occur under a UV lamp, which is not observed in the neat monomer. Using a 0.25 NA microscope objective, thin laminated samples are observed to fluoresce and then quickly bleach under focused $\lambda = 364$ nm light. A camera placed behind a UV filter is used to measure fluorescence intensity and the bleaching process. After using an intense UV beam

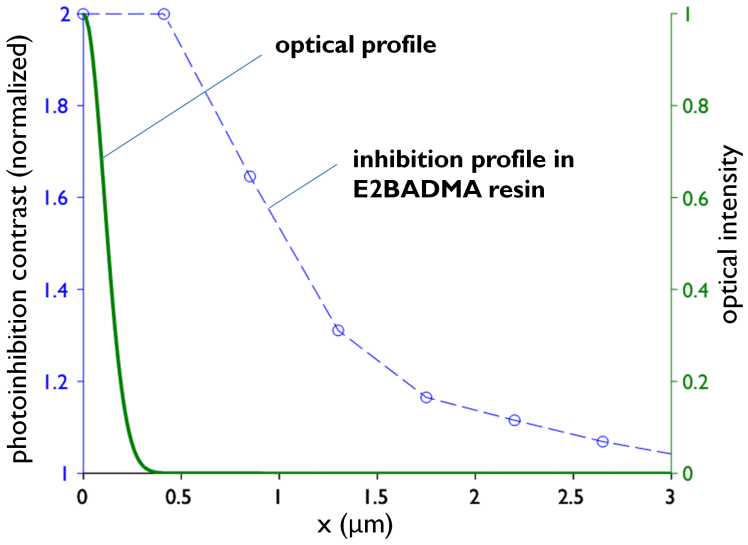

Figure 6.4: Dotted line: the photoinhibition effect of the UV beam is measured as a function of spot offset. Relative to spot centroid alignment, photoinhibition contrast falls to half for a spot offset of 1.1 μm ($P_{\mathrm{B}} = 4.1$ μW, $P_{\mathrm{UV}} = 130$ μW, $\tau =$ 100-600 ms). Solid line: PSF of G-UV optical spot, for comparison. Profile is scaled appropriately to FHWM measured with gold nanoparticle.

to quickly bleach the spot in < 0.5 seconds with bleaching parameter K of approximately 10 [14], half the fluorescence intensity returns after 5.0 seconds.

Using the equation from [14], $D = \gamma_D w^2/4\tau_{1/2}$, I find D to be 0.26 $\mu\mathrm{m}^2{\cdot}\mathrm{s}^{-1}$, which agrees closely with the value used in [81]. Considering that the hole radius of the GL-UV spot is approximately 100 nm (using the 1.2 NA writing lens), radical in-diffusion time may be estimated using the same analysis. For this, I assume a circular hole of $w = 100$ nm and $\gamma_D = 0.88$ [14]. The estimated diffusion time $\tau_{1/2\,\mathrm{DTC}}$ taken for DTC radicals to halfway fill-in the hole is 8.5 ms, 230x faster than the 2 second estimated polymerization and consistent with the order-100x factor estimated earlier from spot offsets. Given these two numbers a-priori, one would not expect to achieve enhanced submicron confinement through photoinhibition with this material.

6.4 Discussion on feature-size reduction vs. superresolution

Since at least three studies have claimed superresolved features at high NA with this technique, under similar conditions, a discussion of their results is warranted. A 2009 paper from Scott et al. was the first publication on this superresolution lithography method, showing the reduction of polymer dots from 5 μm to 1 μm written with 0.45 NA optics, and a 65 nm dot written with 1.3 NA optics [202]. Although the successive reduction in dot diameter demonstrated at 0.45 NA is dramatic, the smallest dot in the SEM image is approximately 1 μm across and is similar in dimensions to a diffraction limited blue spot produced with that optic. The largest dot is several times the diameter of the blue spot, further evidence for the significant out-diffusion of active species, particularly acute in that low viscosity (η = 10 cP @ 25 °C) neat triethylene glycol dimethacrylate system. An isolated 65 nm dot is shown, but there is not clear evidence that the small size was enabled by patterned inhibition. In two follow-up papers from another group [38, 81], the fabrication of 40 nm dots is reported in the same viscous resin used here. The dot diameter is indeed smaller than the FWHM of the writing spot, but experiments demonstrating that this resolution is due to patterned inhibition are not presented. Instead, the figures seem to show that increased UV beam power has an effect equivalent to reduced exposure time. Figure 4b [38] in particular seems to indicate this, including the suggestion of a 60 nm dot fabricated with the UV beam turned off. Another paper from the same group investigates resolution explicitly [81], with tests of dot spacing illustrating the Rayleigh resolvable limit. An inhibition effect is seen in the presence of UV light, but experiments demonstrating that the observed resolution is specifically due to patterned (as opposed to uniform) inhibition are not presented. Another resolution enhancement method [214] that is not controlled in these experiments is the use of conventional inhibitors to sharpen the gel threshold. Considering the measured diffusion and gelation times, it seems likely that feature size reduction at the submicron scale presented to date was most likely due to a combination of the gelation

threshold, oxygen inhibition and unpatterned DTC radical inhibition. These effects can be beneficial for weakly limiting the spatial extent of polymerized features, but are better and more easily achieved without photoinhibition. More recently, Gan et al. [80] have shown suspended lines with 20 nm spacing fabricated by a related method that would seem to prove that patterned photoinhibition enables dramatic superresolution. But the polymer lines in that study are not fixed to a rigid substrate but are instead suspended, a configuration which could lead to significant shrinkage distortion and translational shift during polymerization, solvent rinsing and drying. The resin used in that study is also notable for containing only acrylate monomers along with the photoinhibitor TED, a combination earlier shown to cause total polymerization inhibition. Follow-up work to answer these questions would greatly help to clarify the mechanisms at play.

6.5 Overcoming radical diffusion

To achieve enhanced feature confinement with the advantage of insensitivity to the gelation timescale, photo-cleavable inhibitor molecules would need to react before diffusion causes the optically-defined pattern to blur. In the strong-confinement limit where there is an excess of photoinhibitor, fast elimination through recombination would maintain pattern definition. It has been observed, however, that the DTC radicals found in this work already recombine to form TED at near diffusion-limited rates [191]. Thus, $\tau_{1/2\ \mathrm{DTC}}$ must be increased relative to τ_{gel}. A number of potential approaches can be considered. Photoinhibitor in-diffusion may be slowed by increasing the resin viscosity, and by chemical modifications to increase the molecular weight of the photoinhibitor itself. Gelation can be accelerated by increasing the optical intensity, in combination with a conventional inhibitor to limit continued polymerization in the dark. Further gel acceleration is possible with faster curing resins and/or lowering the gel threshold, for example by increasing the monomer functionality and/or partially polymerizing the resin with a uniform optical precure.

In order to demonstrate unambiguous superresolution on a rigid substrate, I chose to

simultaneously lower species mobility and reduce numerical aperture. Isophorone urethane dimethacrylate (UDMA-IPDI) [12] is a high-viscosity monomer I evaluated for this study. Using the falling ball method I measured a viscosity of $\eta = 500{,}000$ cP, approximately 500× the listed viscosity of E2BADMA. Anticipating the difficulty of measuring very slow diffusion in this resin with the classical FRAP method, I implemented a derivative method by Berk et al. [22] based on spatial Fourier analysis. The results are shown in Fig. 6.6, indicating a diffusivity of 1.2×10^{-4} $\mu m^2 \cdot s^{-1}$, meaning that small-molecule mobility is factor 2,000 slower in UDMA-IPDI than E2BADMA.

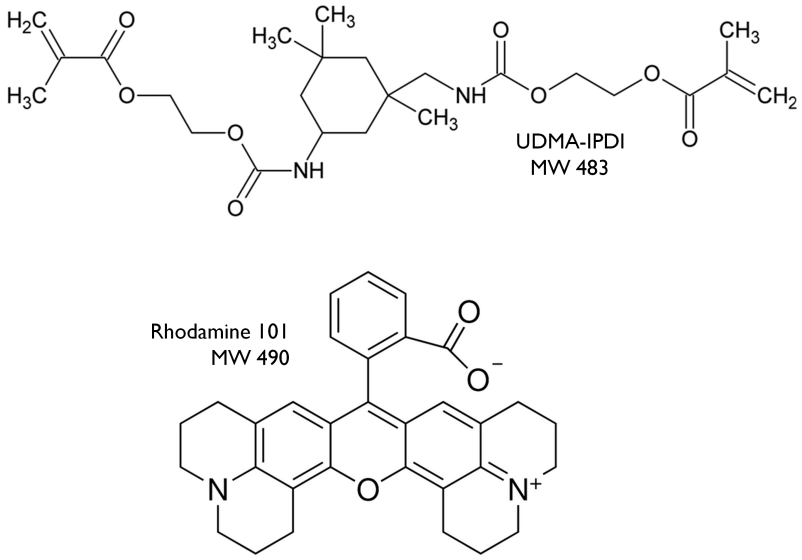

Figure 6.5: Structure of isophorone urethane dimethacrylate (UDMA-IPDI) from Esstech. Also shown is the structure of Rhodamine 101, the fluorescent tracer used for diffusivity measurements.

6.6 Demonstration of superresolution

To make the resin, UDMA-IPDI monomer was heated to 60 °C (to lower viscosity) and mixed with 0.1 wt% CQ, 0.5 wt% EDAB and 3 wt% TED. The fully-dissolved mixture was then spin-coated from cyclohexanone onto cleaned coverslips to form a 1 μm or thinner

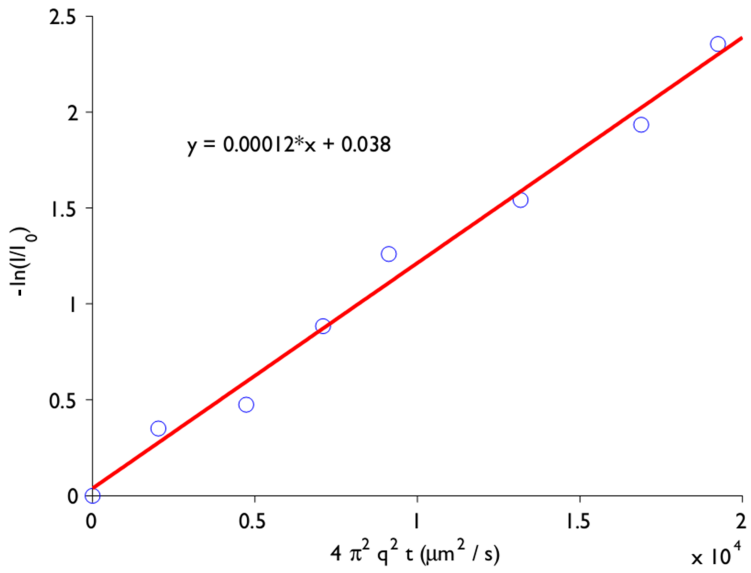

Figure 6.6: Fourier FRAP, after Burk et al. [22]. The slope of the fitted line indicates diffusivity, here estimated to be 1.2×10^{-4} μm^2·s^{-1}.

film. The samples were then mounted onto a nitrogen-purged sample holder and exposed sequentially to focused beams. To prevent CQ and EDAB evaporation, the nitrogen flow first passed through a flask containing a stirred solution of CQ and EDAB in vacuum pump oil.

Polymer dot arrays were inspected with a Olympus AX70 microscope operating in darkfield reflection mode, using 0.5-0.9 NA air objectives. Electron microscope images of gold-coated polymer features were obtained with a JSM-7401F field-emission SEM at an accelerating potential of 5 kV.

Fig. 6.8 - 6.11 show that these measures successfully address the earlier limitations. For the control experiment shown in Fig. 6.8 and 6.9, two polymer dot grids were written in sequence. The first had a square spacing of 5.0 μm and the second of 5.25 μm. The Sparrow diffraction [211] limit is observed for dot spacings of 1000 nm, as expected for $\lambda =$ 473 nm light at 0.2 NA. For the test experiment shown in Fig. 6.10 and 6.11, the first dot grid had a square spacing of 3.0 μm and the second of 3.2 μm. Here, the Sparrow diffraction

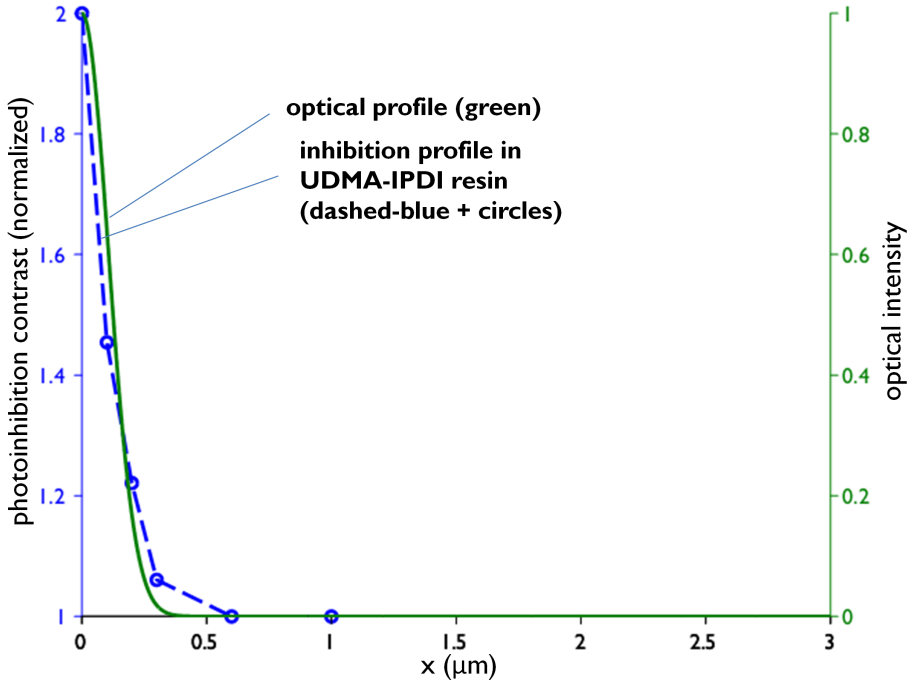

Figure 6.7: Photoinhibition contrast as a function of blue/UV spot misalignment. The blue spot point-spread function (calculated from a FWHM measurement) is shown in blue for comparison. Unexpected narrowness of the photoinhibition profile may indicate a super-linear relationship between the photoinhibition effect and UV spot intensity, though the experiment would need to be repeated several times to establish that the anomaly is real.

limit is observed for dot spacings of 300 nm, thus demonstrating a 3-fold improvement in resolution. Taken together, these tests provide an unequivocal demonstration of transient, enhanced feature confinement usefully applied for superresolved patterning.

I have shown that enhanced pattern confinement in PInSR depends strongly on the mobility of active species. Fast blurring of photo-generated inhibitor is seen in E2BADMA relative to the polymerization timescale, which most likely explains our inability to achieve superresolution in that material via PInSR. To address the issue, I formulated a new PInSR resin from a highly viscous monomer with significantly lower mobility. I also used low-NA optics to further slow diffusion relative to the spot size. This results in a demonstrated 3-fold improvement in resolution beyond the diffraction limit.

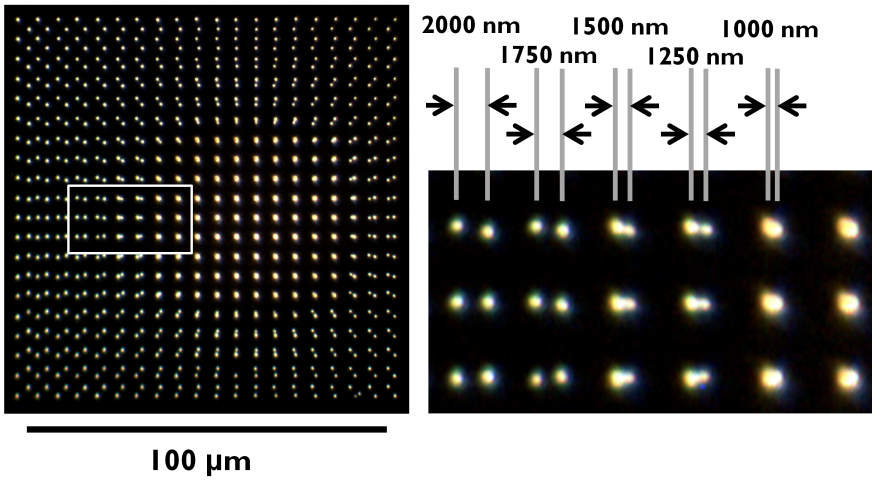

Figure 6.8: Control pattern (inhibiting beam off) written at 0.2 NA in UDMA-IPDI resin. Optical darkfield micrograph (0.8 NA) with zoomed inset. The Sparrow resolution criterion is met at 1000 nm dot spacing.

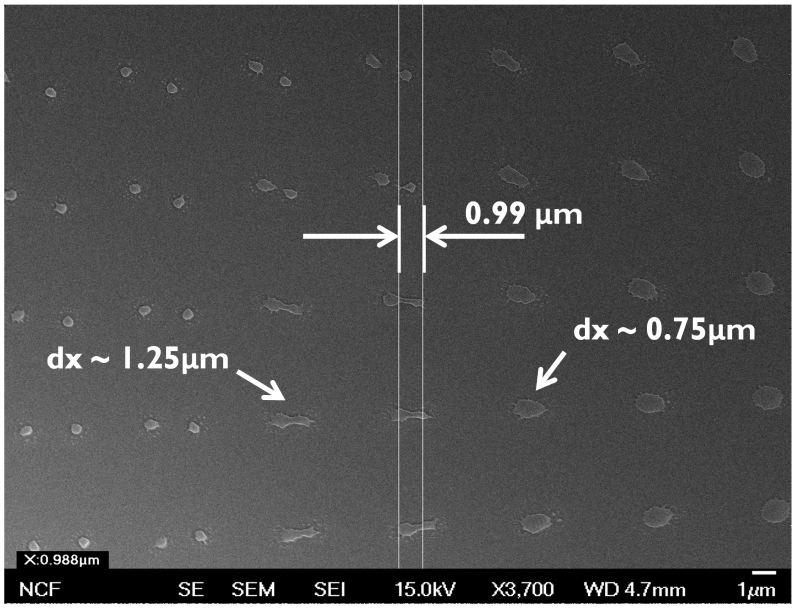

Figure 6.9: SEM image of control pattern in Fig. 6.8, after gold was sputtered onto sample.

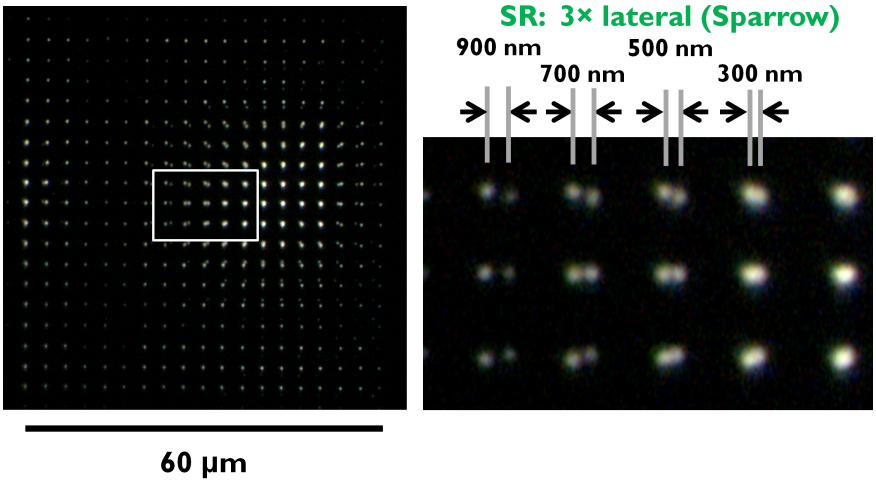

Figure 6.10: Test pattern (inhibiting beam on) written with parameters otherwise same as above. Optical darkfield micrograph (0.8 NA) with zoomed inset. Sparrow resolution criterion is met at 300 nm dot spacing. Darker regions of top dot array may be caused by slight underexposure during writing.

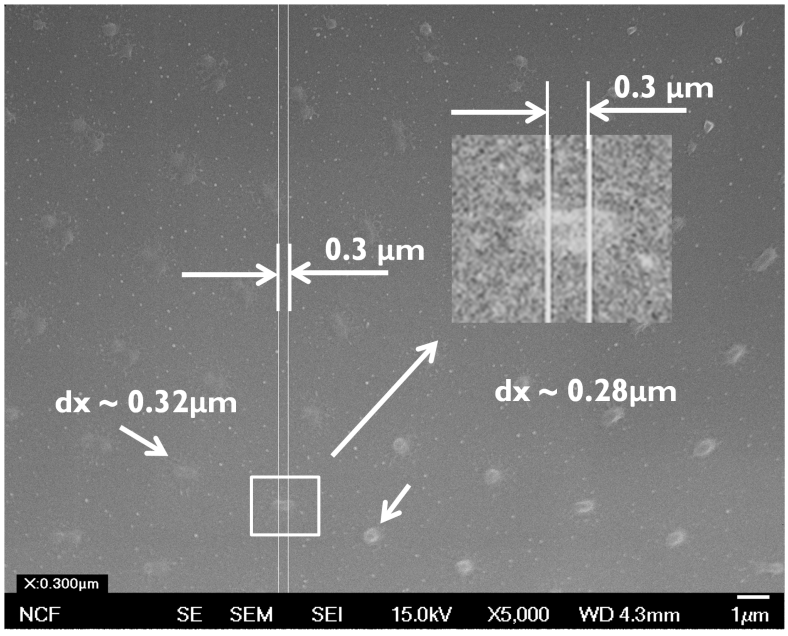

Figure 6.11: Test SEM image of test pattern in Fig. 6.10, after gold was sputtered onto sample.

Chapter 7

Reaction kinetics: analysis and modeling

The complexity of polymerization and, in particular, cross-linking polymerization [8] makes one hesitant to use ab-initio models for quantitative understanding of novel systems. Two factors, however, make a first-principles analysis appealing for understanding photoinhibition and superresolution. Low polymer conversion is required to meet the gel-threshold [202], which, as compared to extensive curing, should limit the amount of difficult-to-predict viscosity and diffusivity change that results from optical exposure. The other factor is that only a limited amount of information can be extracted from patterning experiments. This chapter seeks to develop kinetic analysis of specific phenomena: reactant photogeneration, reaction rates and mass-transfer. It concludes with exciting preliminary analysis, suggesting quantitative prediction of resolution preformance based on spatially-resolved photogenerated radical concentration.

7.1 CQ-amine photoinitiation

The patterning process begins with exposure and photoinitiation, whereby photoinitiator is converted to primary radicals. Camphorquinone absorbs light from the writing beam, which can promote it to an excited singlet state. From there it can quickly decay back to ground state via fluorescence or a non-radiative vibrational relaxation, or undergo intersystem-crossing to an excited triplet state. This state can slowly relax back to ground via phosphorescence or by reaction with another molecule in the system, which is possible given

long triplet-state half-life. In particular, it can abstract a hydrogen from a tertiary amine such as ethyl 4-(dimethylamino) benzoate, a co-initiator, creating a primary α-aminoalkyl radical and relatively unreactive ketyl radical. As discussed by Cook [50], one would expect conversion efficiency to depend on mobility given the finite lifetime of the triplet state ($\approx$ 50 ms). The CQ bleaching rate remains essentially unchanged even in glassy resins, however, probably meaning that relatively immobile CQ molecules are able to react with other molecules in the immediate vicinity. Starting with the analysis shown in [43], the consumption of a generic bleachable photoinitiator [PI] is described by

$$-\frac{d}{dt}[PI] = 10^3 \frac{\Phi_{\mathrm{PI}} I_{\mathrm{abs}}}{L} = 10^3 \frac{\Phi_{\mathrm{PI}} I (1 - e^{-\varepsilon'_{\mathrm{PI}} L[PI]})}{L} \tag{7.1}$$

where Φ_{PI} is quantum yield, I is irradiance in mol-hν·cm^{-2}·s^{-1}, $\varepsilon'_{\mathrm{PI}}$ is Napierian (decadic ε·2.302) molar absorptivity in M^{-1}·cm^{-1}, L is sample thickness in cm, and 10^3 cm^3·L^{-1}. Taking the thin-film approximation of Eq. 7.1,

$$\lim_{L \to 0} \frac{d}{dt}[PI] = -(10^3) \Phi_{\mathrm{PI}} I \varepsilon'_{\mathrm{PI}} [PI]. \tag{7.2}$$

Integrating Eq. 7.2 and normalizing,

$$\frac{[PI]}{[PI]_0} = e^{-(10^3)\Phi_{\mathrm{PI}} I \varepsilon'_{\mathrm{PI}} t}, \tag{7.3}$$

so that the characteristic $1/e$ dose-to-bleach is

$$It = \frac{1}{10^3 \Phi_{\mathrm{PI}} \varepsilon'_{\mathrm{PI}}}. \tag{7.4}$$

Chen et al. [43] determined quantum yield and molar absorptivity of CQ in a viscous methacrylate resin with 0.35 wt% tertiary amine monomer, using a blue LED dental lamp for illumination. Trial-averaged $\Phi_{\mathrm{CQ}} = 0.07$ and $\varepsilon_{\mathrm{CQ}} = \varepsilon'_{\mathrm{CQ}}/2.302 = 46$ M^{-1}·cm^{-1}. This gives $I_{\mathrm{B}}t = 135$ μmol-hν·cm^{-2}. Moving from (# hν) to J, multiplication with hcN$_{\mathrm{A}}/\lambda$ gives 253 kJ·(mol-hν)$^{-1}$ for 473 nm light. Converting, the dose $I_{\mathrm{B}}t = 34$ J·cm^{-2}. This is somewhat smaller than the value of 43 J·cm^{-2} reported in [43], though there is close agreement with analysis discussed at the end of that paper.

In this analysis, a bleaching event produces one primary radical and eliminates one CQ molecule. In order for bleaching to occur, a series of events must follow the creation of an excited singlet CQ by photon absorption: from the initial state, it must undergo intersystem crossing (ISC) to an excited triplet state and, while still excited, diffuse to react with another molecule to produce a single primary radical. The lumped probability of this chain of events occurring after photon absorption is expressed by the quantum yield Φ_{CQ}. In the case of photon absorption events that do not yield a primary radical, the CQ molecule is assumed to return to its original unbleached state.

7.2 Photocleavage of TED

The photoinhibitor TED does not require another reactant to produce dithiocarbamyl radicals (DTC·); instead, they are generated directly from photo-induced scission of the disulfide bond. Because DTC· + DTC· → TED, the rate equation for TED photodissociation has an additional term so that

$$\lim_{L\to 0}\frac{d}{dt}[PS] = -10^3(\Phi_{\mathrm{PS}} I \varepsilon'_{\mathrm{PS}}[PS] - k_{rec}([PS]_0 - [PS])^2) \tag{7.5}$$

where k_{rec} is the rate constant for scavenging radical recombination and PS is for photoscavenger, used here interchangeably with photoinhibitor to disambiguate from photoinitiator (PI). Although I discuss geminate recombination as a possible factor, it is not included in k_{rec}. Instead, geminate recombination is lumped into Φ_{PS}, which is the photodissociation efficiency (or quantum yield) coefficient such that PS $\xrightarrow{I\varepsilon_{\mathrm{PS}}\Phi_{\mathrm{PS}}}$ S· + S·. The recombination term $k_{\mathrm{rec}}([PS]_0 - [PS])^2$ describes the rate at which freely diffusing S· radicals combine to form the original photoinhibitor molecule, with S· + S· $\xrightarrow{k_{\mathrm{rec}}}$ PS. Because of this, photoinhibitor is not irreversibly bleached as with camphorquinone. If recombination is fast and photodissociation slow, scavenger concentration [S·] is low and [PS] is nearly its initial concentration $[\mathrm{PS}]_0$. On the other hand, if recombination is slow and photodissociation fast, [S·] can approach $2[\mathrm{PS}]_0$ and temporarily deplete [PS].

Because k_{rec} is medium-dependent, as discussed in detail below, photoinhibition dose is not a generally meaningful concept. But in order to gain some sense of TED photosensitivity, we can make the momentary assumption that recombination does not occur and treat TED photodissociation as analogous to CQ bleaching. Photodissociation sensitivity is then

$$It = \frac{1}{10^3 \Phi_{\text{PS}} \varepsilon'_{\text{PS}}}. \tag{7.6}$$

From UV-vis absorbance measurements presented earlier, molar absorptivity of TED ε_{TED} at $\lambda = 364$ nm is 250 $\text{M}^{-1}\cdot\text{cm}^{-1}$. This is similar to the value of 210 $\text{M}^{-1}\cdot\text{cm}^{-1}$ found in [149]. From that same reference, quantum yield Φ_{TED} is reported through kinetic model fits to be a strong function of wavelength, with $\Phi_{\text{TED}} = 0.33$ at $\lambda = 365$ nm. However, this value appears to be not absolute but relative to an arbitrarily assigned quantum yield of 1 for the photoinitiator DMPA, at $\lambda = 310$ nm. Without an absolute Φ_{DMPA} available, it is not possible to obtain an absolute Φ_{TED} from the relative value. In an unrelated European government report, absolute Φ_{TED} is listed as 2.97×10^{-3} for $\lambda > 290$ nm.[1] . Unfortunately, no further discussion or methods were found to accompany this value. Kerckhoven et al. [224] reported the quantum yield of TED at $\lambda = 280$ nm in cyclohexane from measurements of the signature ESR decay of 4-hydroxy-TEMPO, arriving at $\Phi_{\text{TED}} = 2.5 \times 10^{-3}$. Although the paper discussion describes the reported yield as relating to the dissociation event, the calculation instead appears to be based on the unscaled depletion of the radical TEMPO concentration C by the equation

$$\Phi_d = \frac{-dC/dt}{\alpha I_0}, \tag{7.7}$$

where α is TED absorbance and I_0 is UV optical irradiance. Since two identical radicals are produced by photodissociation of one TED molecule, strict quantum yield of *dissociation*, rather than DTC· production, may actually be half the reported value: $\Phi_{\text{TED}} = 1.25 \times 10^{-3}$. Calculating from this the flash $I_{\text{UV}}t$ required to dissociate TED to the 1/e level before recombination can occur, we obtain 1.39 mmol-h$\nu\cdot\text{cm}^{-2}$. Assuming that quantum

[1] European Commission "Review report for the active substance thiram," 6507/VI/99-Final

yield is wavelength-independent for $\lambda > 290$ nm as implied by the European Commission report, 328 kJ·(mol-hν)$^{-1}$ for 364 nm light converts 1.39 mmol-hν·cm^{-2} to 457 J·cm^{-2}. This assumption is at odds, however, with the fitted values reported in [149] where the apparently relative $\Phi_{\mathrm{TED}} = 0.33$ at $\lambda = 365$ nm but $\Phi_{\mathrm{TED}} = 0$ at $\lambda = 290$ nm. This last value is dubious, as clear and detailed evidence of TED photodissociation at $\lambda = 285$ nm is reported elsewhere [191] (and reproduced here in Fig. 7.3). To resolve this discrepancy, additional data would be helpful. Later in this chapter I will introduce a kinetic model for two-color photopolymerization control and, after validating it with existing data, use additional existing data to independently determine Φ_{TED}.

Since geminate recombination is known to significantly affect photodissociation efficiency in viscous solutions, I will review some of the literature on that topic here. Khudyakov et al. [120] analyzes geminate recombination in terms of competition between dissociation and recombination, k_{diss} and k_{rec}. From flash laser photolysis, they show an inverse-linear relationship between $\log(k_{\mathrm{diss}})$ and $1/T$. This culminates in an observed 5× reduction in the quantum yield of benzophenone as its glycerol host is cooled.

In later work [121], the same author notes that PI quantum yield may not approach zero even when dissolved in a very viscous host. They attribute this to a reduction in k_{diss} *and* k_{rec}. That is, the radical pair (RP) is formed but does not immediately recombine in the long-lived solvent cage. Instead, the RP must undergo a slow diffusional reorientation to align the active centers - during which time it has the finite probability of cage escape. Thus, as $\eta \to \infty$, $\Phi \to \sim$0.1–0.2, depending on RP active center alignment. Khudyakov asserts that fits to cage-reaction vs. viscosity data yielding intercepts of approximately zero ($\Phi \to 0$) have been shown in the literature, indirectly referencing [119, 174, 125] as examples. Re-examining the data in those papers, it appears that no instances of $\Phi < 0.1$ have actually been resolved. We can reasonably expect, therefore, that the TED photoscission efficiency is reduced by no more than factor ∼10 even in very viscous solvents.

Intriguingly, magnetic fields have been shown to decrease geminate recombination in

viscous solvents by slowing radical pair spin transitions [139]. When photon absorption leads to an excited triplet RP within a slowly-relaxing solvent cage, unwanted recombination can occur through $T_{\pm}$-S and T_0-S transitions. When the radical pair is separated but still in-cage, $T_{\pm}$-S transitions are driven by hyperfine coupling and other mechanisms that can be greatly suppressed by an external magnetic field. In contact pairs, however, H-independent spin-orbit coupling dominates the T-S rate. Thus even in the best case of non-contacting caged radical pairs, an external magnetic field can only suppress recombination in the 2/3 of radical pairs born into the $T_{\pm}$ state. With radical pairs occasionally coming into contact while still in-cage, spin-orbit coupling further reduces the magnetic effect. Finally, the 0.1–0.3 T fields required to realize effects of size 10–50% in experiments with related systems [139] would be difficult to implement in DLW for reasons of required magnet proximity and limited clearance, with the expected effect magnitude not large enough to dramatically improve TED quantum yield.

a)

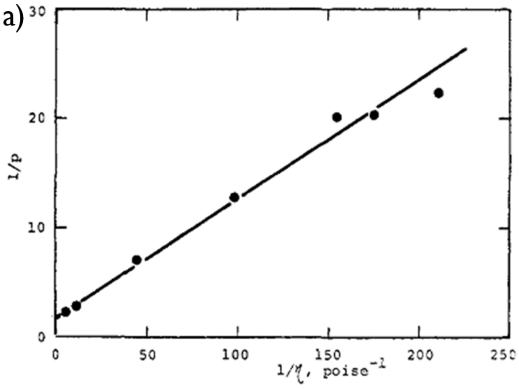

b)

Radical	Solvent	$aA/2b\alpha \times 10^3$ P/deg$^{1/2}$	$a/2b$	$\alpha \times 10^2$
$(CH_3)_3CO\cdot$	Di-2-ethylhexyl-phthalate–benzene	6.24	2.0	0.31
$(CH_3)_3CO\cdot$	Liquid paraffin–benzene	5.73	2.0	0.35
$(CH_3)_3CO\cdot$	Neat aromatics	5.06	2.0	0.40
$(CH_3)_3CO\cdot$	Neat aliphatics	2.64	2.0	0.76
$(CH_3)_3CO\cdot$[a]	Liquid paraffin–isooctane	2.19	2.0	0.92
$(CH_3)_3CO\cdot$, $C_6H_5C(CH_3)_2\cdot$[b]		0.575	1.23	2.1
$CF_3\cdot$[c]		0.5	1.1	2–3
$CH_3\cdot$[d]		0.07	1.1	10–20

Figure 7.1: From Niki et al. [174]: a) original caption : a plot of $1/p$ against $1/\eta$ for 2-ethylhexylphthalate-benzene solutions. b) original caption: the intercept, $a/2b$, for DBPO is about twice as large as those for tert-butylperoxy-α-phenylisobutyrate, per-fluoroazomethane and azomethane. Kodama has also obtained a value for $a/2b$ that is slightly larger than unity for azomethane. This difference must arise from the type and number of intervening molecules.

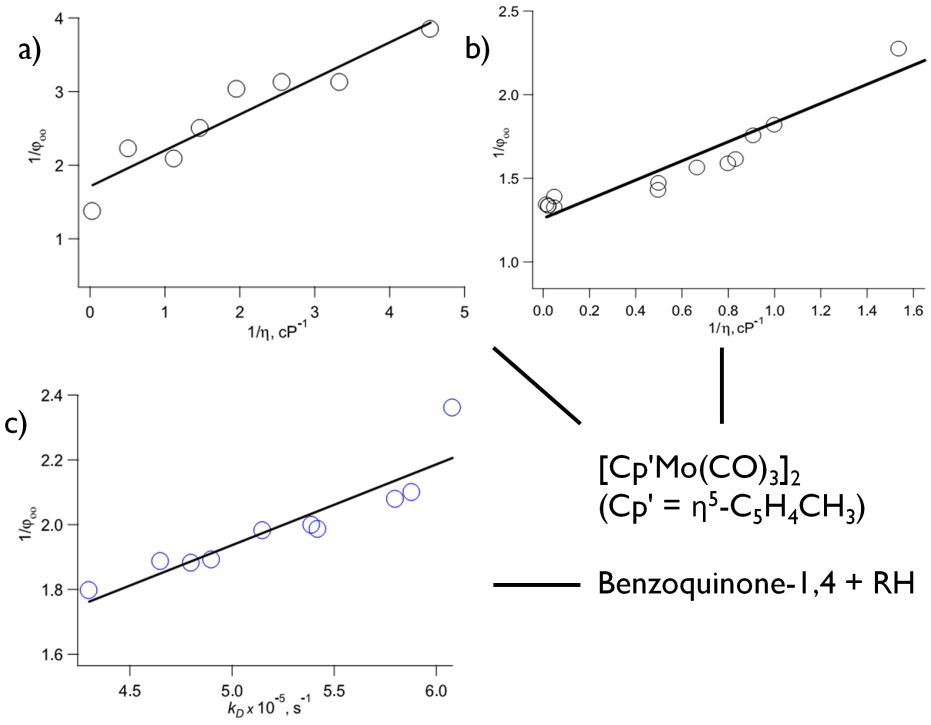

Figure 7.2: From review by Khudyakov in [121]: φ_∞ is probability of geminate recombination. Original data from [176] (a), [30] (b) and [120] (c).

7.3 DTC· recombination

After photolysis, DTC· escaping the solvent cage are free to terminate both primary and propagating radicals. This type of cross-termination is not final, given the finite probability that DTC end-caps can again be broken off by photolysis to regenerate the original carbon and sulfur-centered radicals [224]. For simplicity, however, I will treat DTC· cross-termination of primary and propagating radicals as true termination. TED itself is regenerated by combination of two DTC·, which is a key feature of the PInSR scheme.

Plyusnin et al. [191] studied dissociation and recombination of thiuram disulfides using flash laser photolysis, and found the reaction DTC· + DTC· → TED to proceed at nearly diffusion-limited rates in acetonitrile. That is, in acetonitrile at room-temperature, $2k_{\text{rec}} = 1.48 \times 10^{10}$ $\text{M}^{-1}\cdot\text{s}^{-1}$, compared with $k_{\text{diff}} \approx 10^3 8RT/3\eta = 1.92 \times 10^{10}$ $\text{M}^{-1}\cdot\text{s}^{-1}$, with the small difference attributed to spin and steric factors. The viscosity of acetonitrile $\eta = 0.34$

cP at 25 °C [55], which is lower than all the methacrylate resins discussed here for patterning. Therefore I will assume that TED reformation occurs at the Smoluchowski diffusion-limited rate appropriate for the mobility in a particular system.

As reviewed by Osborne and Porter [180], the usual formula for estimating the diffusion-limited rate constant $k = (10^3)8RT/3\eta$ $\mathrm{M^{-1}{\cdot}s^{-1}}$ [234, 59] results from combination of the Smoluchowski equation (1917)

$$k = (10^3)4\pi\sigma_{\mathrm{AB}}N_A(D_{\mathrm{A}} + D_{\mathrm{B}}) \tag{7.8}$$

for diffusion-controlled reactions, where σ_{AB} is the encounter cross-section, 10^3 $\mathrm{L{\cdot}m^{-3}}$, N_A is Avogadro's number, and $D_{\mathrm{A,B}}$ are the respective diffusivities for species A and B in $\mathrm{m^2{\cdot}s^{-1}}$, with the Stokes-Einstein equation

$$D = \frac{RT}{6\pi r\eta}, \tag{7.9}$$

where r is the diffusing species radius, R is the gas constant in $\mathrm{m^3{\cdot}Pa{\cdot}K^{-1}{\cdot}mol^{-1}}$, T is temperature in K and η is viscosity in Pa·s. It is assumed that the encounter cross-section $\sigma_{\mathrm{AB}} = r_{\mathrm{A}} + r_{\mathrm{B}} = 2r_{\mathrm{A}}$. The Smoluchowski equation is based on the assumption of Fickian diffusion and spherically-symmetric encounters between reactants A and B. This will probably lead to a slightly overestimated rate constant between between bulky reactants. The Stokes-Einstein equation assumes diffusion of a large particle in a continuous, viscous fluid. This assumption is not completely valid for systems where the solvent and solute are of similar dimensions, but large deviations from the formula are probably limited to cases where the assumption is inverted – i.e., when the solute is larger than the solvent [180] (such as the situation of a small tracer dye in a polymer melt).

As shown in Fig. 7.3 from Plyusnin et al., the recombination rate of DTC· into TED is a concentration-dependent second-order reaction. The half-life of a second-order reaction is $1/k[\mathrm{A}]_0$, so doubling [DTC·] by doubling the power delivered in a UV flash to a solution of TED should halve the lifetime of the DTC·.

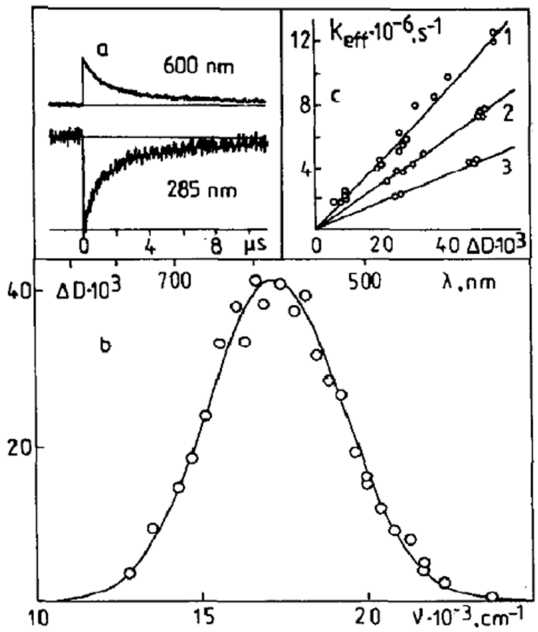

Figure 7.3: From Plyusnin et al. [191]. Original caption: laser flash photolysis of Me_4tds (7 $\times$ 10^{-4} M) in acetonitrile: (a) absorption kinetics after the laser pulse at 600 and 285 nm; (b) optical spectrum of intermediate absorptions (—, approximation by the gaussian curve according to eqn. (9) (of cited paper) with ω_{os}^{exp} = 17300 cm^{-1} and σ = 2050 cm^{-1}); (c) effective rate constant of absorption decay at 600 nm vs. initial ΔOD at temperatures of 297 K (curve 1), 265 K (curve 2) and 230 K (curve 3).

7.4 Chain propagation and inhibition

Unlike TED reformation (DTC· + DTC· $\rightarrow$ TED) and DTC· cross-termination (R· + DTC· $\rightarrow$ R–DTC), methacrylate chain propagation (R· + M $\rightarrow$ M–R·) is slow. Values of k_p taken from the literature vary to some degree, but the measurement of k_p = 274 $M^{-1}{\cdot}s^{-1}$ at 20 °C [24] obtained by Beuermann et al. from pulsed laser polymerization of MMA is used here for reaction-limited kinetic calculations.

Polymerization inhibition with DTC· is more complex than with typical inhibiting species, in part because DTC· is photogenerated and transient. To break the photoinhibition process into simpler components, I will discuss inhibition behavior with a more typical radical scavenger. In radical polymerizations, inhibitors are reactive species that prevent polymerization and must be consumed before polymerization can occur. Persistent radicals

such as TEMPO are efficient inhibitors in typical resins, and are commonly included in formulations for the purpose of stabilization. Little or no polymerization occurs during inhibitor consumption, resulting in the so-called induction period simulated in Fig. 7.4. Retarders are distinct from inhibitors in that they slow polymerization but do not prevent it outright, and are not associated with an induction period. Non-patterned simulations of polymerization inhibition and retardation are based on a set of finite difference coupled equations:

$$\frac{d}{dt}[\mathrm{R}\cdot] = Ik_{\mathrm{PI}}[\mathrm{PI}] - k_{\mathrm{t}}[\mathrm{R}\cdot][\mathrm{S}\cdot] - 2k_{\mathrm{t}}[\mathrm{R}\cdot][\mathrm{R}\cdot] \tag{7.10}$$

$$\frac{d}{dt}[\mathrm{S}\cdot] = -k_{\mathrm{t}}[\mathrm{R}\cdot][\mathrm{S}\cdot] \tag{7.11}$$

$$\frac{d}{dt}[\mathrm{PI}] = -Ik_{\mathrm{PI}}[\mathrm{PI}] \tag{7.12}$$

$$\frac{d}{dt}[\mathrm{M}] = -k_{\mathrm{p}}[\mathrm{M}][\mathrm{R}\cdot] \tag{7.13}$$

$$\frac{d}{dt}[\mathrm{P}] = k_{\mathrm{p}}[\mathrm{M}][\mathrm{R}\cdot], \tag{7.14}$$

where I is optical irradiance, k_{PI} is the lumped photoinitiation rate constant, k_{t} is a diffusion-limited termination constant, k_{p} is a reaction-limited propagation constant, PI is photoinitiator, $R\cdot$ is the primary / propagating radical, $S\cdot$ is radical scavenger, M is monomer and P is polymer.

Interestingly, TEMPO may act as either a polymerization inhibitor or a retarder, depending on mobility. This is due to the ratio of the diffusion-controlled termination rate constant k_{t} to the propagation rate constant k_{p}, which is reaction-controlled in typical formulations. In low-viscosity methacrylate resins, inhibitor $k_{\mathrm{t}} \sim 10^7$ $\mathrm{M}^{-1}\cdot\mathrm{s}^{-1}$ while monomer addition $k_{\mathrm{p}} \sim 10^3$ $\mathrm{M}^{-1}\cdot\mathrm{s}^{-1}$. The ratio $k_{\mathrm{t}}/k_{\mathrm{p}} \sim 10^4$, meaning that primary radicals terminate into inhibitor with extreme specificity (instead of adding into monomer) until the inhibitor is eliminated, as shown in Fig. 7.4. In extremely viscous media such as undiluted bisGMA, both k_{t} and k_{p} are diffusion-controlled and the ratio $k_{\mathrm{t}}/k_{\mathrm{p}}$ is reduced to unity. The result is no preference for one reaction over the other, where the scavenging species reacts concurrently with polymerization. A small amount of inhibitor in highly viscous media does

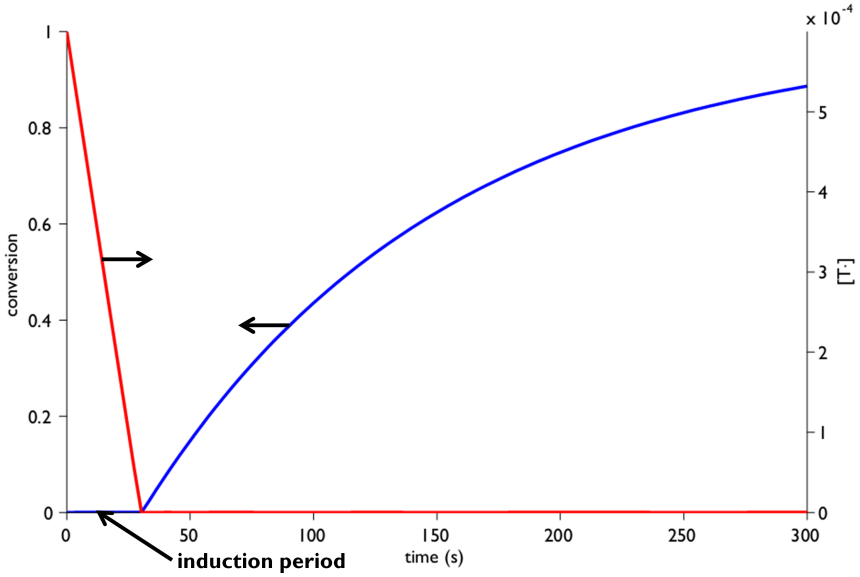

Figure 7.4: Simulated polymer conversion vs. time from Eq. 7.10 - 7.14 for a non-viscous methacrylate resin with a small amount of inhibitor, $D = 30\ \mu\text{m}^2\cdot\text{s}^{-1}$, $k_\text{p} = 270\ \text{M}^{-1}\cdot\text{s}^{-1}$, $k_\text{t} = 2.3 \times 10^8\ \text{M}^{-1}\cdot\text{s}^{-1}$, $[T]_0 = 0.6$ mM. Conversion is in blue and inhibitor concentration in red.

not significantly retard polymerization, as shown in Fig. 7.5. However, a large amount of scavenger can effectively control even low-mobility systems as shown in Fig. 7.6. Thus it is possible to inhibit polymerization even in the highly viscous resins needed for minimal pattern-blurring, as long as scavenger concentration is sufficiently high.

7.5 Spatial confinement of reactive species

As shown earlier, diffusional blurring is an effect of fundamental importance to high-resolution patterning. Unlike photoacid generators (PAGs) used in standard commercial photoresists, which can be converted in a glassy matrix, conventional radical photopolymerization patterning requires mobility and thus diffusion. Figure 7.7 illustrates the speed of diffusion-induced blurring at the nanoscale. For the faster-diffusivity situation, the pattern in species R essentially collapses before $t = 1/k_\text{p}$. For the slower diffusivity system, pattern collapse is delayed for an interval corresponding to many propagation events.

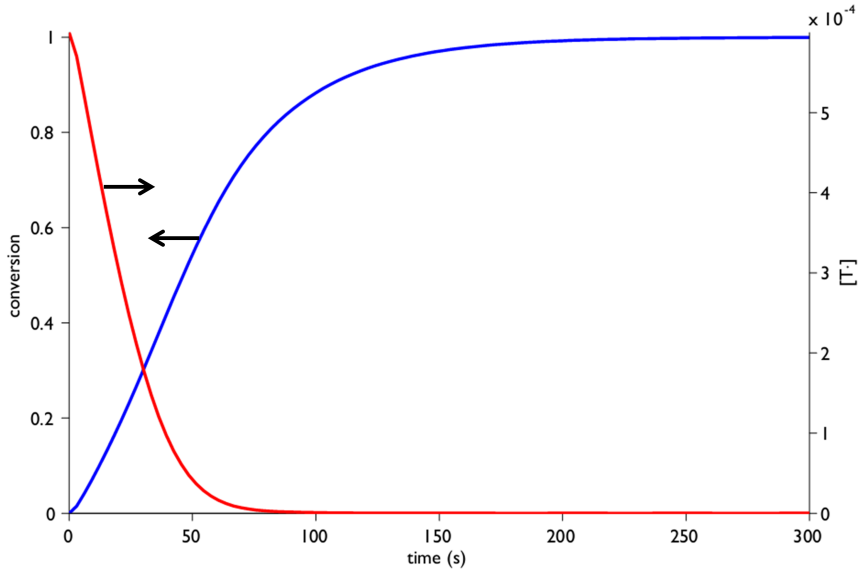

Figure 7.5: Simulated polymer conversion vs. time from Eq. 7.10 - 7.14 for an extremely viscous methacrylate resin with a small amount of inhibitor, $D = 1 \times 10^{-4}$ μm^2·s^{-1}, $k_\mathrm{p} = 270$ M^{-1}·s^{-1}, $k_\mathrm{t} = 900$ M^{-1}·s^{-1}, $[T]_0 = 0.6$ mM. Conversion is in blue and inhibitor concentration in red. There is no apparent induction period; the inhibitor instead acts as a retarder and is consumed during polymerization.

Earlier work showed that optically-generated inhibitor underwent significant blurring, ruining the donut-shaped pattern necessary for enhanced polymerization confinement [75]. This result implies that, to a significant extent, DTC radicals diffuse past both carbon-centered radicals and one-another. This is a perplexing situation, since these radicals are known to be so highly reactive; one might be tempted to assume that diffusion lengths are negligible, but this assumption is of course ill-advised in the context of submicron patterning. To study the problem, I created a model in which two distinct radical species are generated on either side of a binary interface. From an equilibrium concentration of zero, radicals are generated at source rates S, S' and eliminated by combination. The excitation profile for this simulation is shown in Fig. 7.8. The radicals R· and R′· are allowed to diffuse with diffusivity D, and undergo homo- and heterogeneous termination at the diffusion-limited rate k. The spatial domain of the simulation is +/- 100 nm from the binary interface. Radical generation

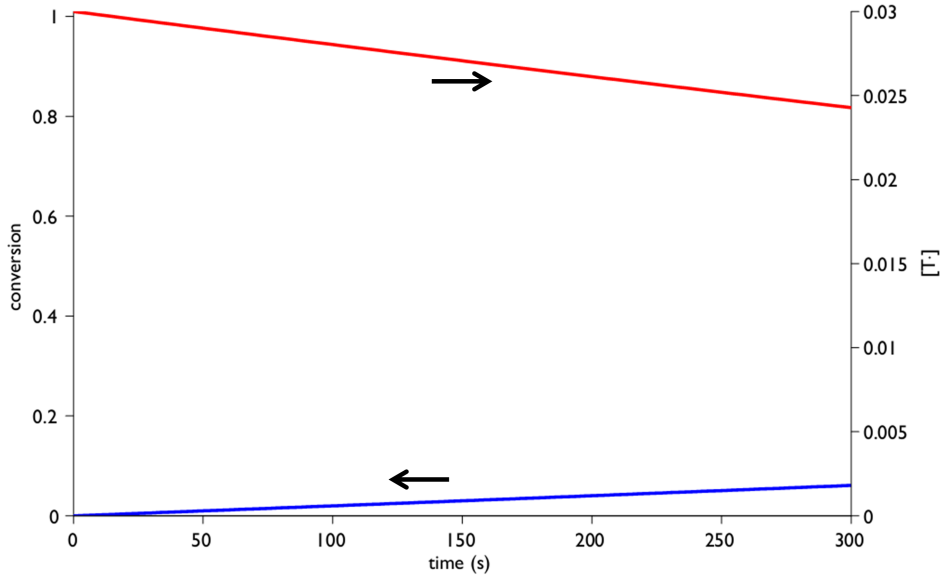

Figure 7.6: Simulated polymer conversion vs. time from Eq. 7.10 - 7.14 for an extremely viscous methacrylate resin with a large amount of inhibitor, $D = 1 \times 10^{-4}$ μm^2·s^{-1}, $k_\mathrm{p} = 270$ M^{-1}·s^{-1}, $k_\mathrm{t} = 900$ M^{-1}·s^{-1}, $[T]_0 = 30$ mM. Conversion is in blue and inhibitor concentration in red. Again, there is no apparent induction period; the inhibitor instead acts as a retarder and is consumed during polymerization.

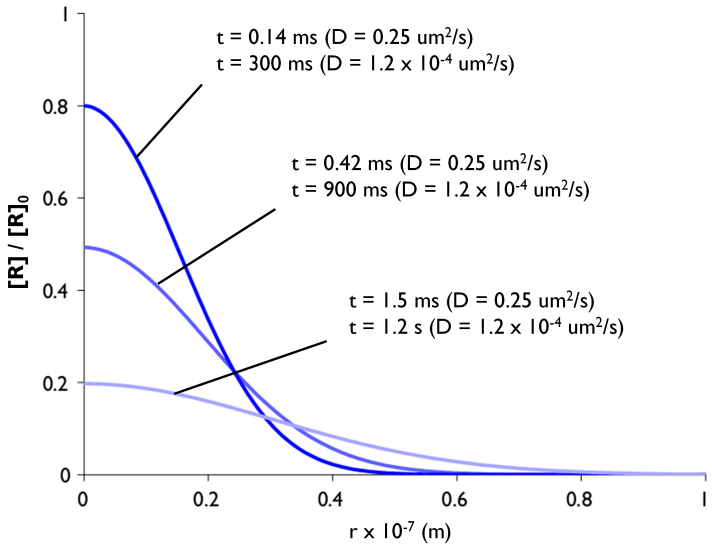

Figure 7.7: Illustration of diffusional relaxation speed for a Gaussian spot of diameter 50 nm.

starts at t = 0 and stops at t = 0.05 s. This model is implemented in the following coupled differential equations:

$$\frac{d}{dt}[\mathrm{R}\cdot] = S - k[\mathrm{R}\cdot][\mathrm{R}\cdot] - k[\mathrm{R}\cdot][\mathrm{R}'\cdot] + (\nabla \cdot D)\nabla[\mathrm{R}\cdot] \tag{7.15}$$

$$\frac{d}{dt}[\mathrm{R}'\cdot] = S' - k[\mathrm{R}'\cdot][\mathrm{R}'\cdot] - k[\mathrm{R}\cdot][\mathrm{R}'\cdot] + (\nabla \cdot D)\nabla[\mathrm{R}'\cdot]. \tag{7.16}$$

Fig. 7.9, 7.10 and 7.11 show the interesting result that the thickness of the interfacial region is concentration-dependent. When the rate of radical generation is comparatively slow, culminating in $\sim\mu$M concentrations, the R radicals do a poor job of confining R′ radicals and vice-versa; both radical populations diffuse to the far end of the simulated domain. But as the rate of radical generation is increased, so is confinement. At ∼mM concentrations, R radicals and R′ radicals effectively confine each other to a region within 10 nm of the interface. More fundamentally, they confine themselves; removal of R′ radical generation has only a small effect on the spatial extent of R radical diffusion. Adding a non-zero equilibrium concentration of persistent radicals (such as TEMPO) would tend to sharpen these distributions, but the non-patterned nature of such a distribution would only be useful for improving resolution up to but not beyond the diffraction limit.

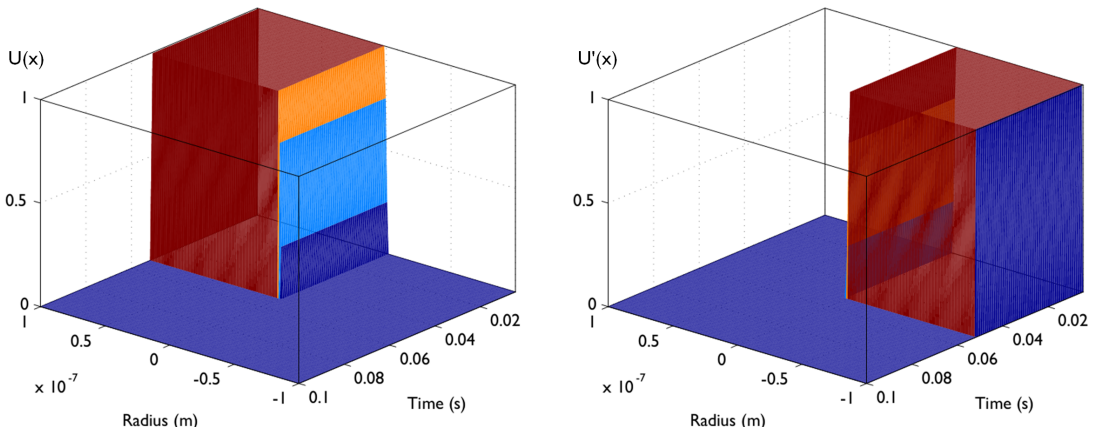

Figure 7.8: Forcing function for generation of radical species $R\cdot$ and $R'\cdot$ with linear, binary interface. The reactions $R\cdot + R\cdot \rightarrow RR$, $R'\cdot + R'\cdot \rightarrow R'R'$ and $R\cdot + R'\cdot \rightarrow RR'$ all proceed at the diffusion-limited rate k.

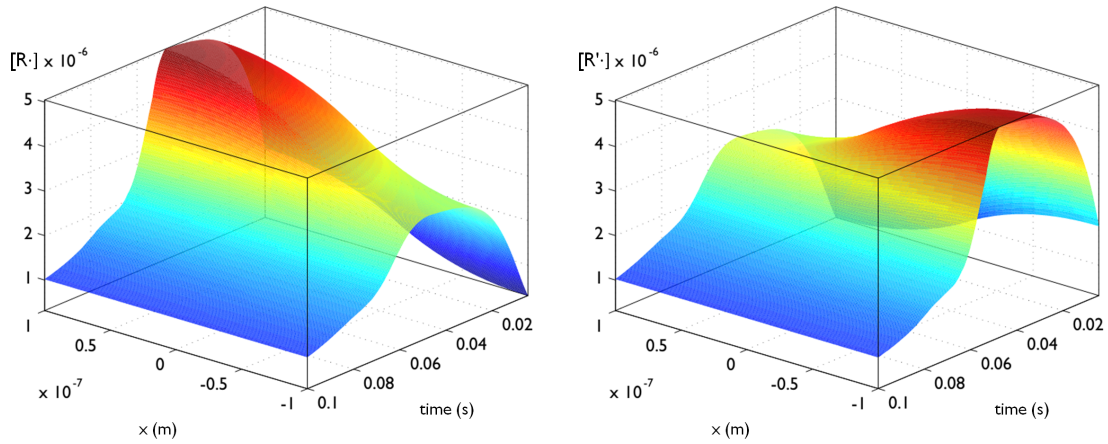

Figure 7.9: Low confinement (300 nm edge width), resulting from a slow rate of radical generation: $S = (0.01)UC$, $S' = (0.01)U'C$.

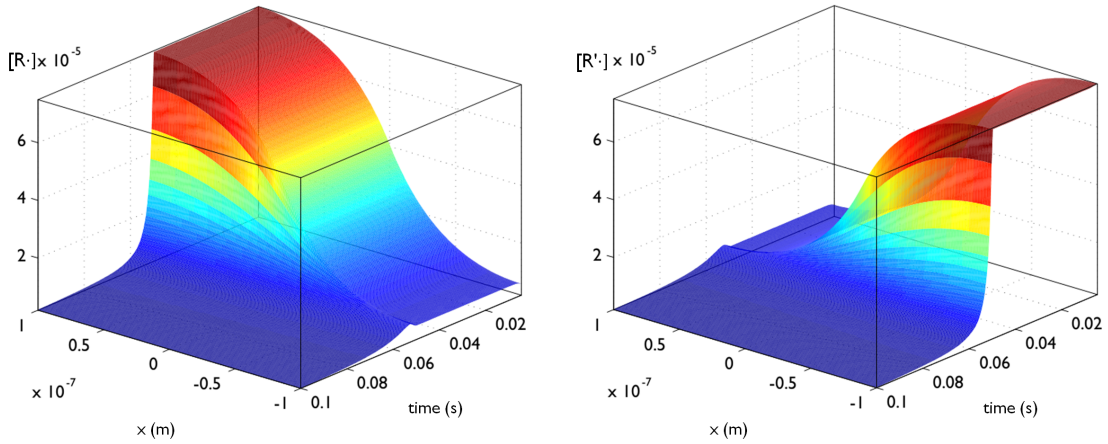

Figure 7.10: Medium confinement (80 nm edge width), resulting from a moderate rate of radical generation: $S = (1)UC$, $S' = (1)U'C$.

Interestingly, this relationship is dependent only on concentration and is independent of diffusion. While at first surprising, it is to be expected since radical-radical combination is explicitly scaled with the diffusion constant D. If the reactions in a real system are diffusion-limited, this has the physical meaning that species react once they come into contact. A uniform change in mobility, which is approximate effect of adjusting viscosity, only alter the amount of time required for this to happen. Differences in mobility between reactants would change the distribution, however, with distribution of the faster-moving reactants

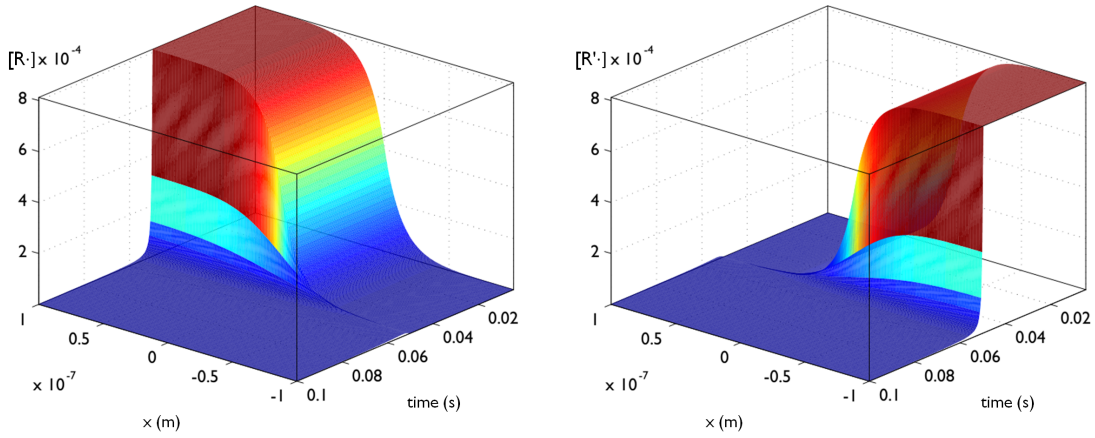

Figure 7.11: High confinement (25 nm edge width), resulting from a fast rate of radical generation: $S = (100)UC$, $S' = (100)U'C$.

asymmetrically controlling the distribution of the slower-moving reactants.

Fig. 7.12 shows the simulated FWHM spatial impulse response of homogeneous radicals generated at a point and along a line, allowed to recombine at the diffusion-limited rate. It implies that for a desired pattern resolution d, a corresponding radical concentration [R·] must be reached. This simulation only applies to distributions of homogeneous radicals that terminate into one another. Heterogeneity in the diffusion constant and cross-termination will change the impulse response.

7.6 PInSR model

Cross-linking photopolymerization of a bulk resin is a complex process, during which rate constants can change by orders of magnitude. In addition, species mobility in the system can also become highly heterogeneous as polydisperse populations of polymer chains are formed alongside small monomer and initiator molecules. Despite the difficulty, these and other factors are successfully dealt with by materials scientists using modern analytical instruments and techniques. When faced with the submicron dimensions and millisecond optical exposures in direct write lithography, however, accurate through-cure modeling is unrealistic and possibly even unnecessary (due to the low degrees of cure required for gel

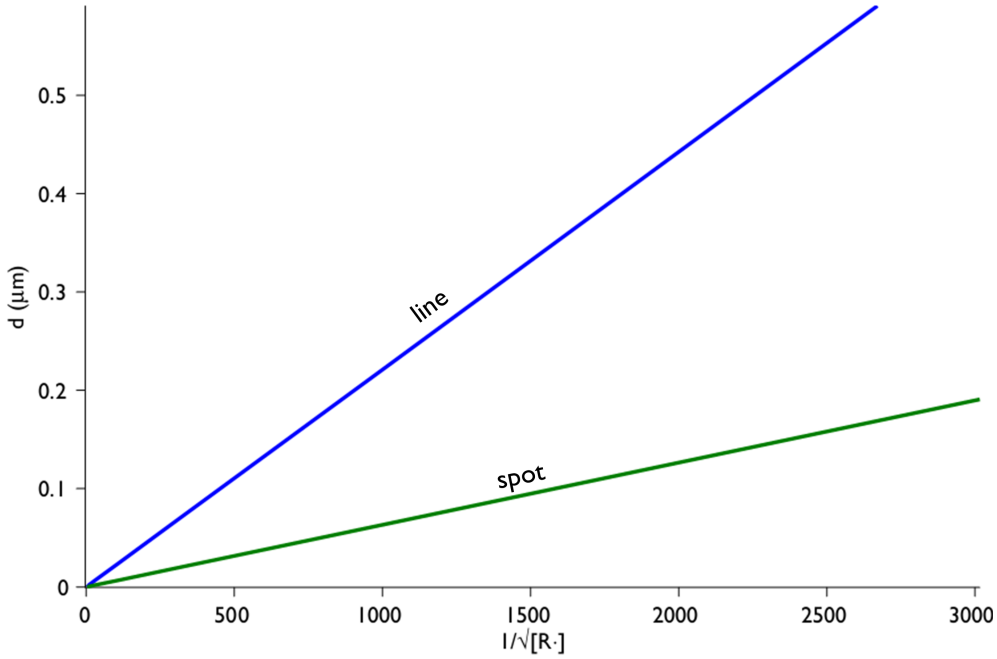

Figure 7.12: Simulated impulse-response of radical confinement (FWHM) vs. molar concentration.

onset).

Instead, the model presented here is limited to the beginning stages of polymerization that precede significant chain-growth and cross-linking. It consists of a system of 6 coupled differential equations with defined initial conditions. For simplicity, primary and propagating radicals are lumped into the term R·. Photoinhibitor (photoscavenger) PS is regenerated by combination of scavenging radicals S·, but photoinitiator PI must be replenished by the diffusion term. R· is consumed by combination with S· and by bimolecular termination resulting in inactive R–R. Monomer M is consumed by R·, creating polymer P. Spatial concentration gradients will be omitted for now. The equation set is:

$$\frac{d}{dt}[\mathrm{R}\cdot] = I_\mathrm{W} k_\mathrm{PI}[\mathrm{PI}] - k_\mathrm{t}[\mathrm{R}\cdot][\mathrm{S}\cdot] - 2k_\mathrm{t}[\mathrm{R}\cdot][\mathrm{R}\cdot] \tag{7.17}$$

$$\frac{d}{dt}[\mathrm{S}\cdot] = 2I_\mathrm{I} k_\mathrm{PS}[\mathrm{PS}] - k_\mathrm{t}[\mathrm{R}\cdot][\mathrm{S}\cdot] - 2k_\mathrm{t}[\mathrm{S}\cdot][\mathrm{S}\cdot] \tag{7.18}$$

$$\frac{d}{dt}[\mathrm{PI}] = -I_\mathrm{W} k_\mathrm{PI}[\mathrm{PI}] \tag{7.19}$$

$$\frac{d}{dt}[\mathrm{PS}] = -I_\mathrm{I} k_\mathrm{PS}[\mathrm{PS}] + k_\mathrm{t}[\mathrm{S}\cdot][\mathrm{S}\cdot] \tag{7.20}$$

$$\frac{d}{dt}[\mathrm{M}] = -k_\mathrm{p}[\mathrm{M}][\mathrm{R}\cdot] \tag{7.21}$$

$$\frac{d}{dt}[\mathrm{P}] = k_\mathrm{p}[\mathrm{M}][\mathrm{R}\cdot], \tag{7.22}$$

with the rate constants to be defined shortly. To provide initial validation of this model, reliable experimental data is needed. For this I turn to the original PInSR publication by Scott et al. [202], specifically the demonstration of two-color polymerization control by broad-area illumination in a series of time-resolved FTIR methacrylate conversion studies. The resin consists of monomer with 1.0 wt% photoinitiator, 0.5 wt% co-initiator and 3.0 wt% photoinhibitor. An LED dental lamp provides the sample with an irradiance of 15 $\mathrm{mW{\cdot}cm^{-2}}$ in a narrow spectrum centered on $\lambda = 469$ nm, while a mercury-arc lamp, operating with a $\lambda = 365$ nm bandpass filter, independently delivers an irradiance of 64 $\mathrm{mW{\cdot}cm^{-2}}$. Returning to the model, the rate constant for blue-light CQ photoinitiation $k_\mathrm{PI} = 1/38$ $\mathrm{cm^2{\cdot}J^{-1}}$, which is calculated from molar absorptivity and quantum yield in section 7.1. The diffusion-controlled termination rate constant $k_\mathrm{t} = 1.89 \times 10^8$ $\mathrm{M^{-1}{\cdot}s^{-1}}$, also used for S· recombination, is set by monomer viscosity $\eta = 10$ cP with Eq. 7.8 and 7.9. The propagation rate constant $k_\mathrm{p} = 274$ $\mathrm{M^{-1}{\cdot}s^{-1}}$, as discussed in section 7.4. Intensities $I_\mathrm{W} = 15$ $\mathrm{mW{\cdot}cm^{-2}}$ and $I_\mathrm{I} = 0$. Initial concentrations are converted to molarity to give $[\mathrm{PI}]_0 = 0.0602$ M and $[\mathrm{M}]_0 = 3.642$ M. As shown in Fig. 7.13, the model compares favorably with experiment for the initial stage of polymerization.

As discussed in section 7.2, the literature on TED quantum yield Φ contains large discrepancies and may be particularly unreliable at $\lambda = 365$ nm. With the blue-light re-

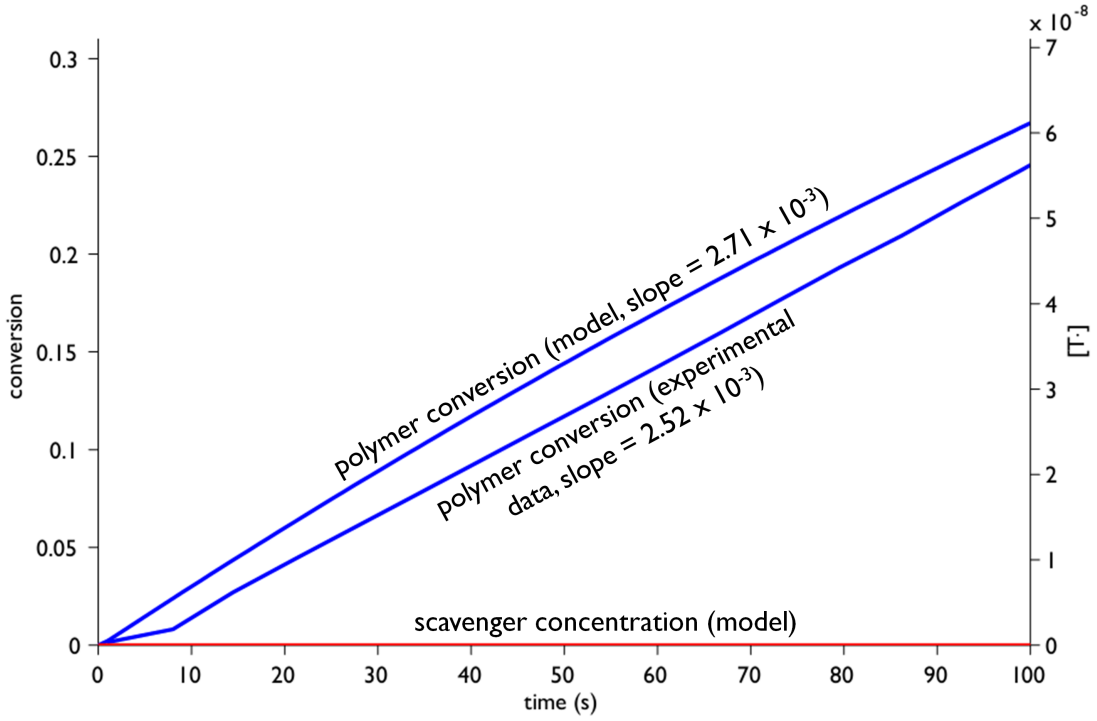

Figure 7.13: Evaluation of the model defined in Eq. 7.17 – 7.22. Model output is validated against data from the blue-light photopolymerization described in [202]. All parameter values are obtained from independent measurements, or calculated ab initio.

sponse of the model validated, I will now use it to independently obtain TED quantum yield. Modifying the model to reflect the two-color photoinhibited polymerization experiment described in [202], two parameters are set: $[\mathrm{PS}]_0 = 0.101$ and $I_\mathrm{I} = 64$ mW·cm^{-2}. The only remaining parameter is k_PS, set by Eq. 7.4 with $\varepsilon_\mathrm{PS} = 250$ M^{-1}·cm^{-1} and Φ_PS to be fit. Here I determine fit in the interval $30 < \mathrm{t} < 50$ s by ratio of polymer conversion slopes, or photoinhibition contrast (PIC), with experimental PIC = 4.83. As shown in Fig. 7.14, a slope of 5.63×10^{-4} ($1/4.83 \times$ model slope from Fig. 7.13) is obtained from the photoinhibited model with $\Phi_\mathrm{PS} = 1.29 \times 10^{-3}$. This value agrees extremely well with the revised dissociation quantum yield $\Phi_\mathrm{TED} = 1.25 \times 10^{-3}$ obtained in section 7.2 from [224] at $\lambda = 280$ nm. Model sensitivity to this range of Φ_PS is high, with a 1% pertubation in Φ_PS resulting

in a 5% change in conversion slope, providing additional confidence in the value precision.

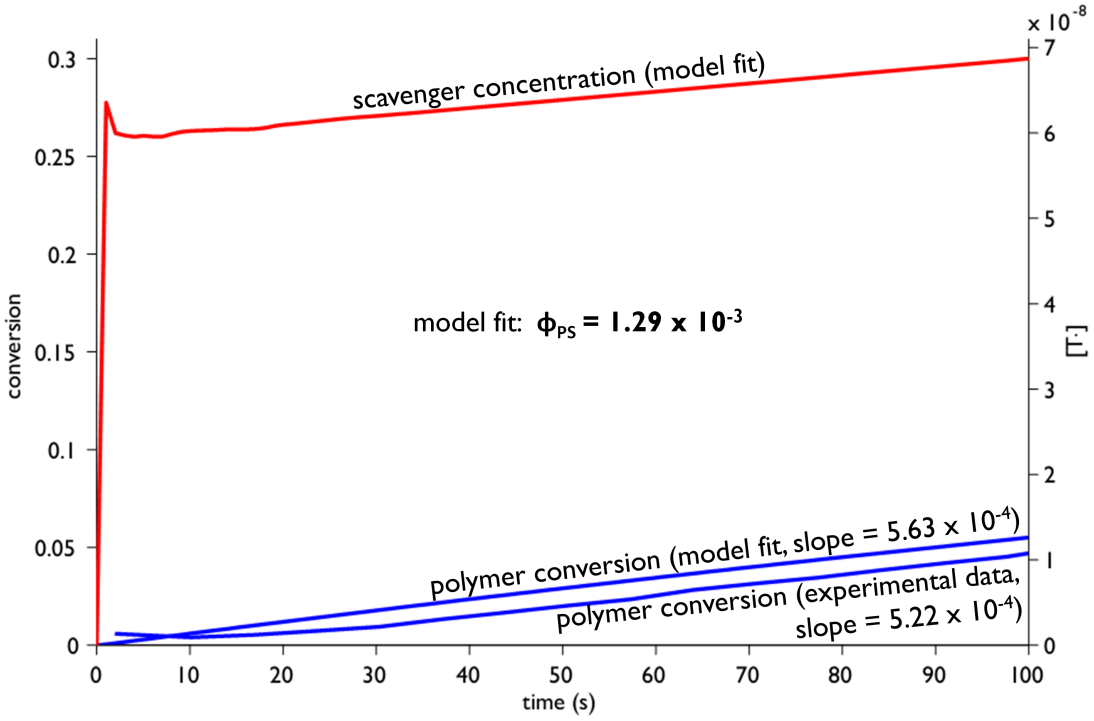

Figure 7.14: Independent determination of photoinhibitor (photoscavenger) quantum yield Φ_{PS}, by measurement of photoinhibition. Curing data shown here was collected during simultaneous blue and UV irradiation, under conditions otherwise identical to the blue-only data shown in Fig. 7.13. Polymer conversion slope data from the two experiments is used to obtain a fitted-value for Φ_{PS}, from the model described in Eq. 7.17 – 7.22.

After achieving some degree of validation of the unpatterned model and obtaining a reasonable value for photoinhibitor quantum yield, I finally turn to the patterned PInSR model. It is identical to the model in Eq. 7.17 – 7.22, with the addition of spatial concentration gradients that are induced by reaction and relaxed by diffusion:

$$\frac{d}{dt}[\mathrm{R}\cdot] = I_\mathrm{W} k_\mathrm{PI}[\mathrm{PI}] - k_\mathrm{t}[\mathrm{R}\cdot][\mathrm{S}\cdot] - 2k_\mathrm{t}[\mathrm{R}\cdot][\mathrm{R}\cdot] + (\nabla \cdot D)\nabla[\mathrm{R}\cdot] \tag{7.23}$$

$$\frac{d}{dt}[\mathrm{S}\cdot] = 2I_\mathrm{I} k_\mathrm{PS}[\mathrm{PS}] - k_\mathrm{t}[\mathrm{R}\cdot][\mathrm{S}\cdot] - 2k_\mathrm{t}[\mathrm{S}\cdot][\mathrm{S}\cdot] + (\nabla \cdot D)\nabla[\mathrm{S}\cdot] \tag{7.24}$$

$$\frac{d}{dt}[\mathrm{PI}] = -I_\mathrm{W} k_\mathrm{PI}[\mathrm{PI}] + (\nabla \cdot D)\nabla[\mathrm{PI}] \tag{7.25}$$

$$\frac{d}{dt}[\mathrm{PS}] = -I_\mathrm{I} k_\mathrm{PS}[\mathrm{PS}] + k_\mathrm{t}[\mathrm{S}\cdot][\mathrm{S}\cdot] + (\nabla \cdot D)\nabla[\mathrm{PS}] \tag{7.26}$$

$$\frac{d}{dt}[\mathrm{M}] = -k_\mathrm{p}[\mathrm{M}][\mathrm{R}\cdot] + (\nabla \cdot D)\nabla[\mathrm{M}] \tag{7.27}$$

$$\frac{d}{dt}[\mathrm{P}] = k_\mathrm{p}[\mathrm{M}][\mathrm{R}\cdot], \tag{7.28}$$

with kinetic constants modified from before to describe the high-viscosity UDMA-IPDI resin used in Chap. 6. Here $D = 1.2 \times 10^{-4}$, $k_\mathrm{I} = 1/443$ cm^2·J^{-1} (using the value $\Phi_\mathrm{TED} = 1.29 \times 10^{-3}$) and $k_\mathrm{t} = 908$ M^{-1}·s^{-1}. Irradiances I_W and I_I are obtained by assuming Gaussian beams to obtain the spot radius

$$w_0 = \frac{\lambda}{\pi N A}, \tag{7.29}$$

and calculating area $A = \pi w_0^2$ to obtain average irradiance $I = P/A$. Without any inhibiting beam, feature size is defined by the diffraction limit of the focused blue beam as shown in Fig. 7.15. Low power in the GL inhibiting beam causes scavenger concentration to slowly build to a moderate level, resulting in moderate super-confinement of polymerization as shown in Fig. 7.16. Significantly increasing the GL beam power leads to scavenger concentration quickly building to a higher steady-state level, resulting in additional super-confinement as shown in Fig. 7.17.

The model output provides spatially-resolved polymer conversion, from which a gel threshold can be subtracted to calculate isolated feature size. Additional analysis on the the model output can provide an evaluation of pattern resolution. Taking the final cure

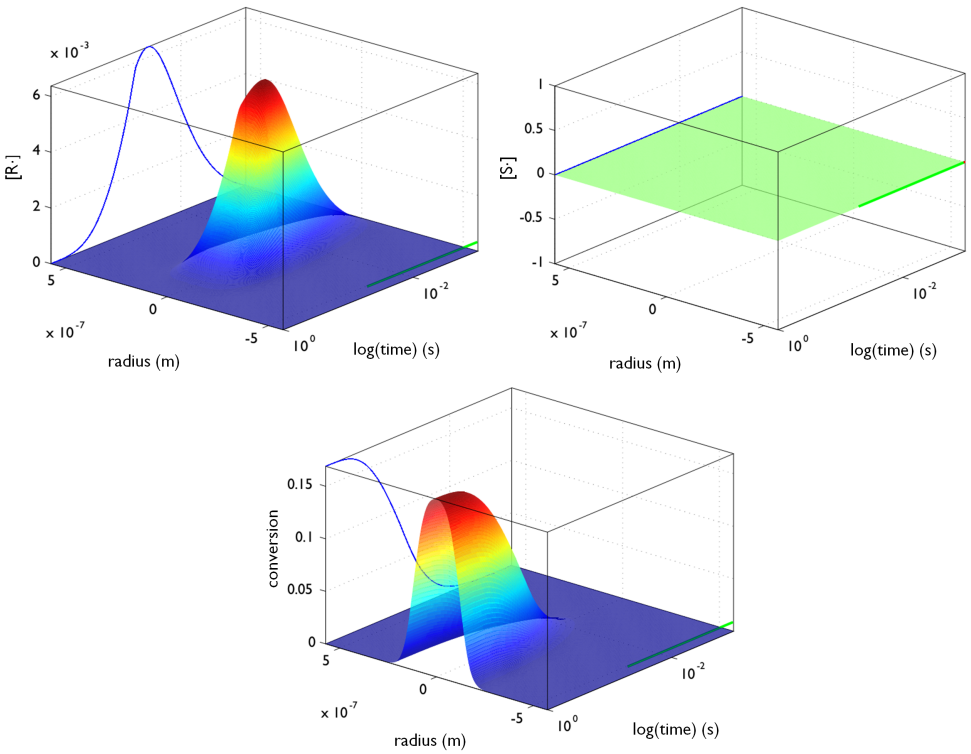

Figure 7.15: No inhibiting beam. Resolution is defined by diffraction-limited profile of the writing beam. $P_{\mathrm{W}} = 1\ \mu\mathrm{W}$, $t_{\mathrm{on}} = 0$, $t_{\mathrm{off}} = 50$ ms. $P_{\mathrm{I}} = 0$. NA = 1.2.

profile from the diffraction-limited case shown in Fig. 7.15, a row of spot exposures may be simulated by taking the sum of arbitrarily shifted, stamped profile copies as shown in Fig. 7.18. The Sparrow limit is reached in polymer conversion at a spacing of 233 nm, 26% larger than the optical Sparrow limit at 1.2 NA for $\lambda = 473$ nm light assuming twin Airy disks offset by $d = 0.47\lambda/\mathrm{NA}$. A somewhat wider profile is to be expected from the sublinear kinetics of single-photon photopolymerization. With the addition of the inhibition spot, modulation depth is improved at the intermediate dot spacing and is still near 50% at the non-photoinhibited Sparrow limit as shown in Fig. 7.19. When photoinhibited, subdiffraction exposures are packed tightly enough, the thick "tails" of the spatial cure profile (see Fig. 7.16 and 7.17) add together and give rise to undesirable final-pattern cure profiles. This is addressed in Fig. 7.20 with non-uniform exposures, calibrated to compensate

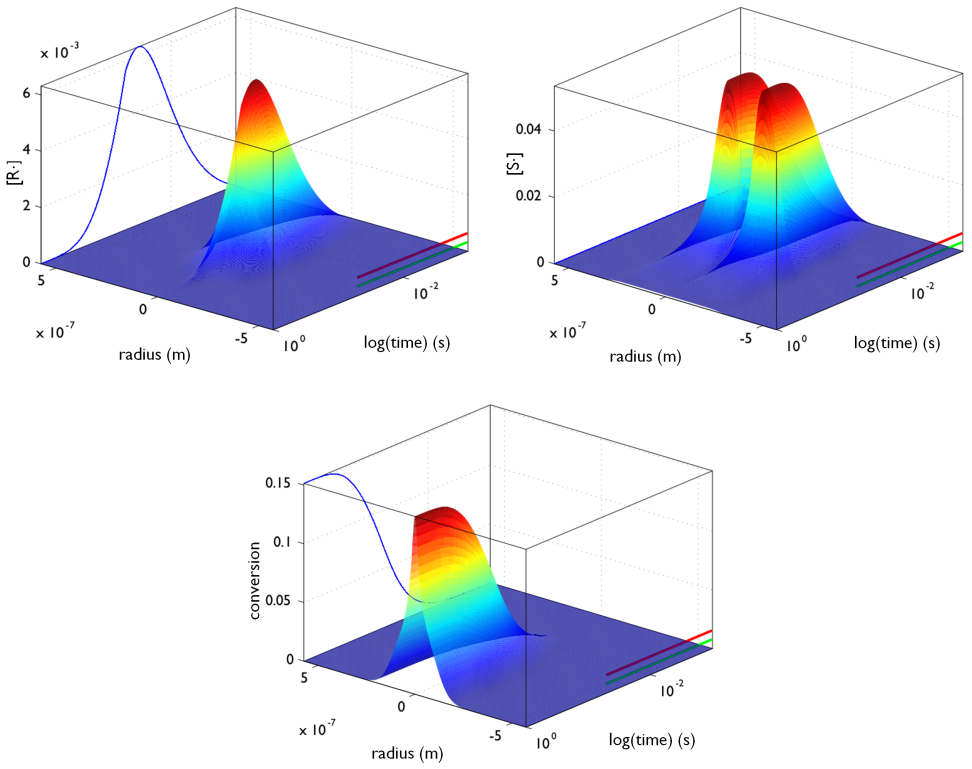

Figure 7.16: A less intense inhibiting beam achieves steady-state [S·] more slowly. Moderate [S·] allows moderate super-confinement of polymerization. $P_{\mathrm{W}} = 1$ μW, $t_{\mathrm{on}} = 0$, $t_{\mathrm{off}} = 50$ ms. $P_{\mathrm{I}} = 6.0$ μW, $t_{\mathrm{on}} = 0$, $t_{\mathrm{off}} = 50$ ms. NA = 1.2.

for the thick-tail profile modeled in Fig. 7.16.

In this chapter I have quantitatively analyzed the kinetics of individual portions of the PInSR system, leading-up to a full model and simple lithographic simulations. The differential equation describing photoinitiator consumption was solved, yielding the expression for required optical exposure for 1/e initiator conversion. Using literature values for CQ molar absorptivity and quantum efficiency, I predict a value that is consistent with the experimental optical exposures given in chapter 6. Photodissociation of TED is treated similarly and the result is roughly consistent with experiment, although DTC· recombination and the large variation in quantum yield reported in the literature precludes a direct comparison. While the empirical observation of dramatically-reduced photoinhibition efficacy with increased vis-

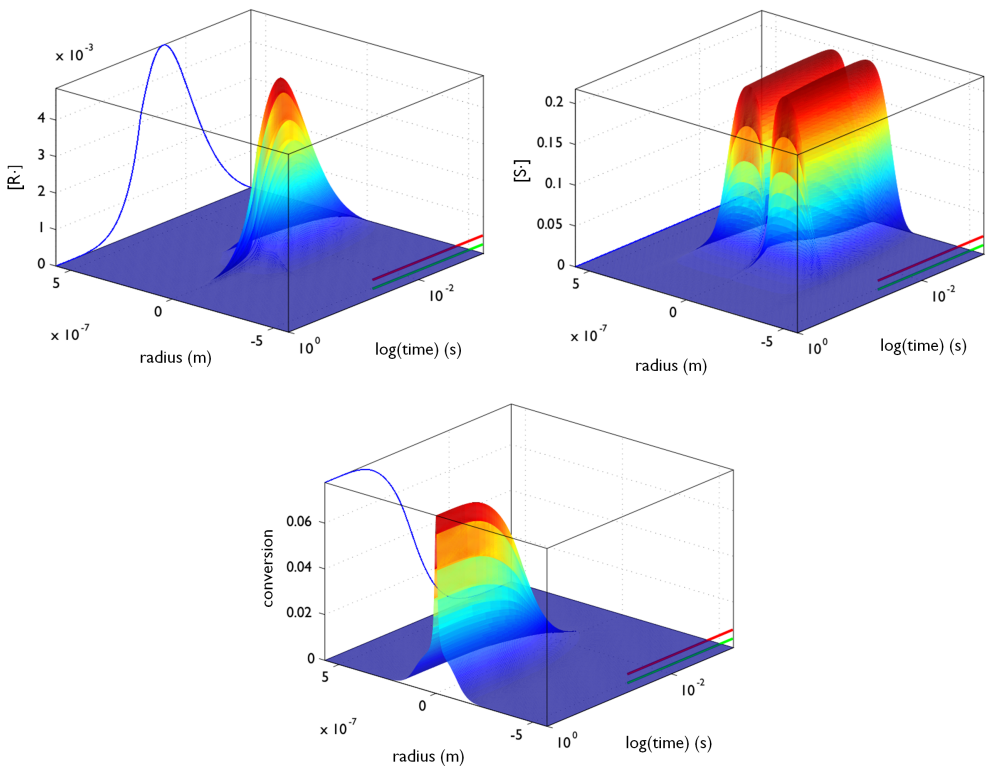

Figure 7.17: A more intense inhibiting beam achieves steady-state [S·] more quickly. High [S·] allows strong super-confinement of polymerization. $P_{\mathrm{W}} = 1\ \mu\mathrm{W}$, $t_{\mathrm{on}} = 0$, $t_{\mathrm{off}} = 50$ ms. $P_{\mathrm{I}} = 600\ \mu\mathrm{W}$, $t_{\mathrm{on}} = 0$, $t_{\mathrm{off}} = 50$ ms. NA = 1.2. Since the model does not account for polymerization from high inhibition beam exposure (which has been observed experimentally), this particular result may be difficult to achieve in practice.

cosity (as observed via FTIR during two-color curing experiments) is consistent with findings from a literature survey on geminate recombination, I show that the largest reductions in photoinhibition efficacy are to be expected in highly viscous media from an independent effect: strong attenuation of the diffusion-controlled termination rate constant k_{t}. This effect may be overcome with high scavenger concentration, which is also necessary for another reason: spatial confinement of fine, photo-generated patterns of reactive species. Evaluation of a simple, coupled differential equation model shows that reactants must be present at ~ 1 mM concentrations to reduce diffusion lengths adequately for < 100 nm patterning. Further development of this mass-transfer theory will prescribe the optical and material conditions

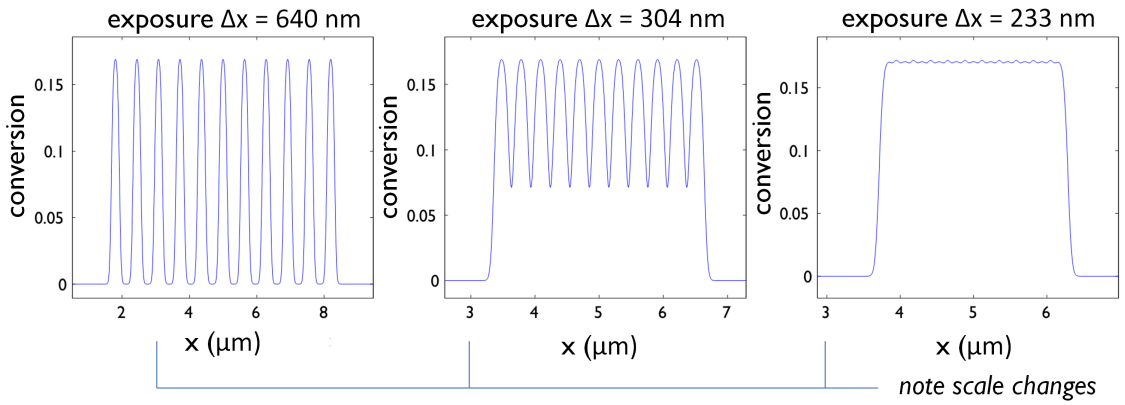

Figure 7.18: Polymer conversion profile from multiple spot exposures along a line, without photoinhibition. As exposures become more tightly spaced, the conversion profiles from individual exposures begin to add at the periphery thus reducing the total modulation. At right, the Sparrow diffraction limit (zero modulation across the pattern) is met with sufficiently tight spacing. Individual conversion profiles are taken the final time-step in Fig. 7.15.

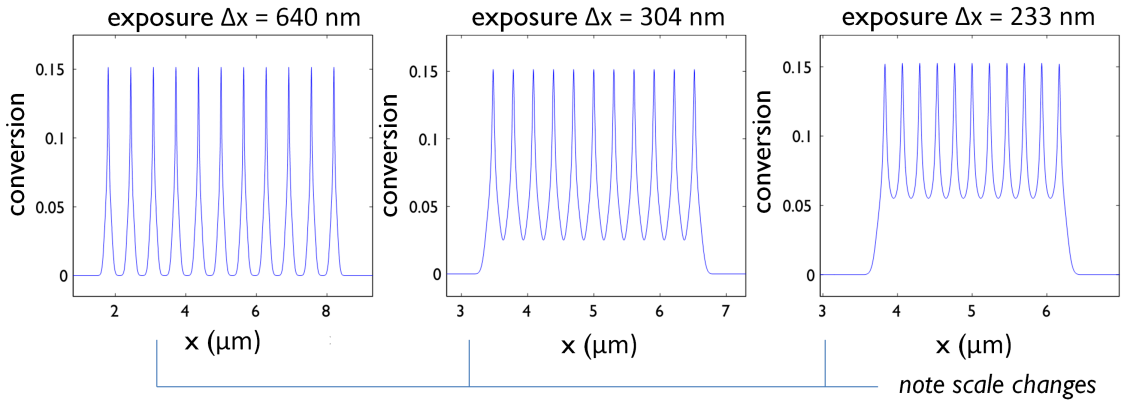

Figure 7.19: Polymer conversion profile from multiple spot exposures along a line, with photoinhibition. In contrast to the non-photoinhibited case, individual spots are still clearly resolved for $\Delta x = 233$ nm. Individual conversion profiles are taken from the final time-step in Fig. 7.16.

required for photopatterning at the smallest length scales. I develop a system model, starting with the photoinitiation component which is validated against experimental data. Using additional data from the same experiment, I estimate photoinhibitor quantum yield through

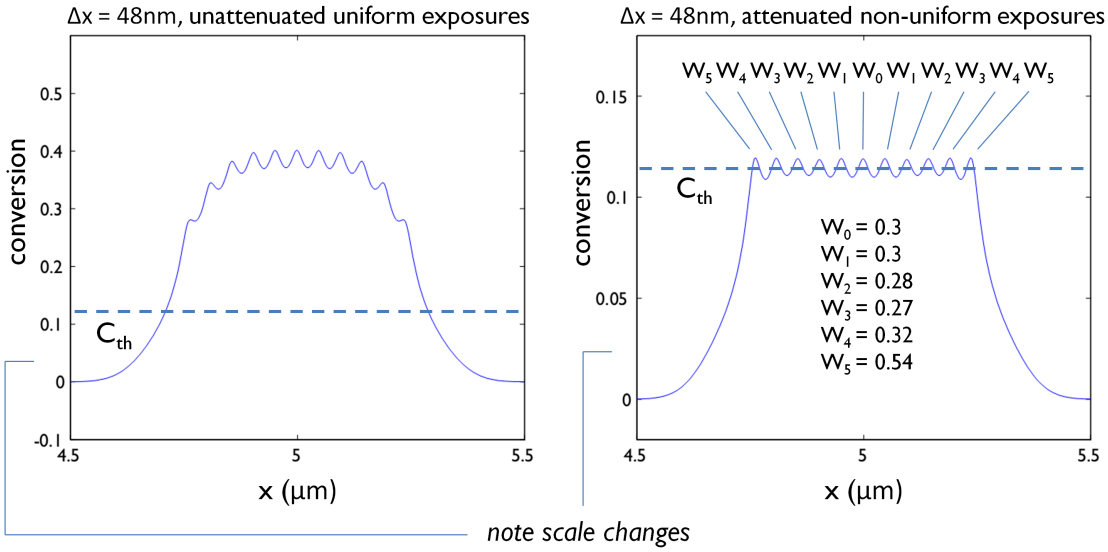

Figure 7.20: Near the zero-modulation limit from tight subdiffraction spacing and assuming the benefit of a sharp gel threshold, the LHS profile suffers from two problems. The first is excess polymer conversion accumulated from the tightly-spaced exposures, causing a single large feature to develop instead of several small features. See Fig. 7.19 for max conversion values at diffraction-limited spacing; identical photoinhibited cure profiles from Fig. 7.16 are used here. The second problem is drooping at the pattern-edge. To improve this situation, attenutated, non-uniform exposures are employed. Each of the weights scales the individual conversion profile taken from the final time-step in Fig. 7.16, so that the stamped copy $C'_n(x) = C(x)W_n$. Since spatial concentration gradients are induced by each exposure, this analysis assumes gradients have been given sufficient time to relax before additional exposures are adjacently placed at subdiffraction distances. An arbitrary conversion threshold C_{th} is shown to illustrate the level adjustment and spot-uniformity enhancement.

a photoinitiation / photoinhibition model. The full PInSR model generates as output the spatial cure profiles result from photoinhibited and non-photoinhibited exposures. Finally, I assemble individual spot-cure profiles together to simulate actual lithographic resolution performance for a simple subdiffraction pattern.

Chapter 8

Surface patterning and interference lithography

As I have shown, two-color, single-photon superresolved lithography via patterned inhibition requires simultaneous management of optical alignment, resin wetting, oxygen removal, species evaporation, chemistry and mobility-dependent photoinhibition efficacy and, fundamentally, resolution limits that are dependent on reactant concentration. This situation spurred my interest in finding a nanopatterning technique where the various physical processes are decoupled and sequenced in time. In this chapter I describe a scheme for achieving deep-subwavelength superresolution with a single monochromatic source, inspired by (and a variation of) multiple patterning techniques used in CD $< \lambda(4\mathrm{NA})$ electronic device fabrication. It utilizes a surface-tethered photochemistry that requires no films or gas-management, and essentially eliminates diffusion of active species. Preliminary results are shown.

8.1 Photopatterning of surface-tethered molecules

In 1991, Fodor et al. published the landmark paper "Light-directed, spatially addressable parallel chemical synthesis." It demonstrated polypeptide arrays grown from a rigid substrate, patterned into designed sequences by a combination of optical exposures and coupling reactions as illustrated in Fig. 8.1. Significantly, this work enabled sequence-characterization of biopolymers on mass-produced chips with surface-tethered $m \times n$ polypeptide arrays on planar substrates, each array cell containing a specific peptide sequence. When the pat-

terned surface is treated with a solution of unknown and fluorescently-tagged polypeptides, the freely-diffusing fluorescent polypeptides bind preferentially to the tethered polypeptides with complementary sequences. After rinsing away mobile species, fluorescent microscopy reveals the sites where binding occurred. Mapping these sites back to the tethered polypeptide sequences reveals the complimentary sequence of polypeptides in the test solution.

The Affymax (Fodor et al.) system used low resolution contact-mask exposure and was designed for fluorescent-readout instead of pattern transfer, but two features of this work are interesting for superresolution lithography: diffusion of active species is eliminated by surface-tethering, and the photosensitivity of a molecular site can be controlled by the preceding reaction sequence.

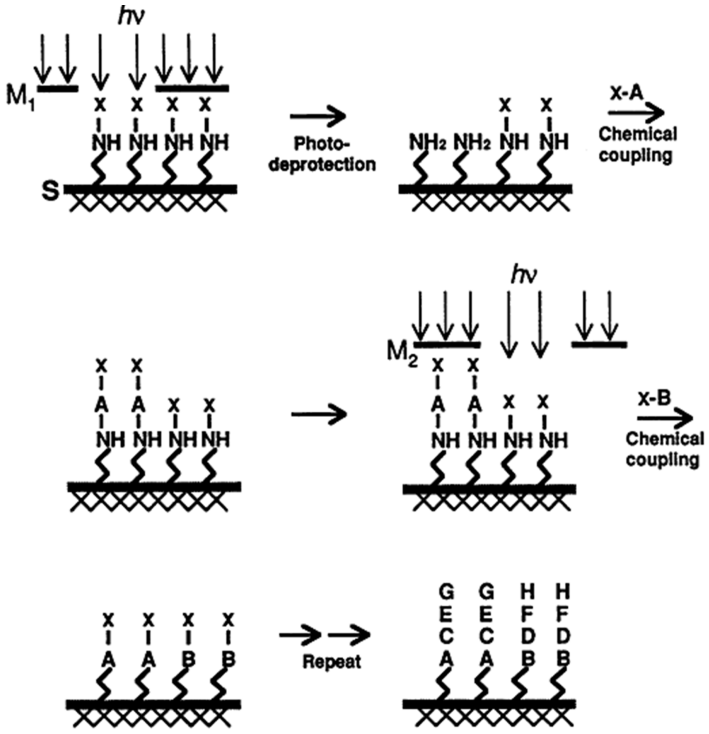

Figure 8.1: Figure reproduced from [74]. A combination of light patterning and reaction sequencing allows the spatially-resolved, sequential assembling of immobilized polypeptides on a single substrate. In this process, each deprotection / coupling cycle necessarily increases chain length because only a portion of each coupled group is photolabile.

8.2 Surface-tethered molecular lithography

Instead of requiring two species with orthogonal absorption spectra to react in competition with one another, under the control of a specialized two-color exposure system, sequential control surface patterning suggests enhanced feature confinement via a single photosensitive species and a more conventional single-color exposure system. If the surface can be refreshed to restore the region surrounding a super-confined feature, repeating the process with a small spatial offset allows superresolution.

Figure 8.2 shows a proposed scheme for superresolved molecular lithography, utilizing three orthogonal protection chemistries: a photo-labile group for patterning, an acid-labile group for temporary blocking and a base-labile group for quasi-terminal blocking. Ordering of the acid and base-labile protecting groups could be reversed, and either or both replaced by other protection / deprotection strategies. Other examples of amine protecting chemistries are carbobenzyloxy and p-methoxybenzyl carbonyl groups, removed with hydrogenolysis, or the nosyl group, removed with thiophenol [82].

Although surface-patterned lithography has mostly been used for applications requiring detection of probe-target hybridization, such as DNA microarrays, it has also been used for structure fabrication. Vossmeyer et al. [225] demonstrated combinatorial patterning of different nanoparticle species on a single Si surface. Unable to couple NVOC directly onto the substrate-bound 3-aminopropylmethyldiethoxysilane, they first coupled NVOC to glycine, which they were then able to react onto the surface amine. Two cycles of pattern exposure followed by nanoparticle coupling yielded co-planar features with different functionality.

The sequence used by the Fodor and Vossmeyer teams is typical in the surface photo-deprotection literature, in that a photo-labile protecting group is first coupled to another surface-reactive compound while still in solution. This type of process invariably leaves behind a molecular fragment with every protection / photo-deprotection cycle. An alternative approach used by Piehler [189] and Waichman [231] is to incorporate a PEG spacer

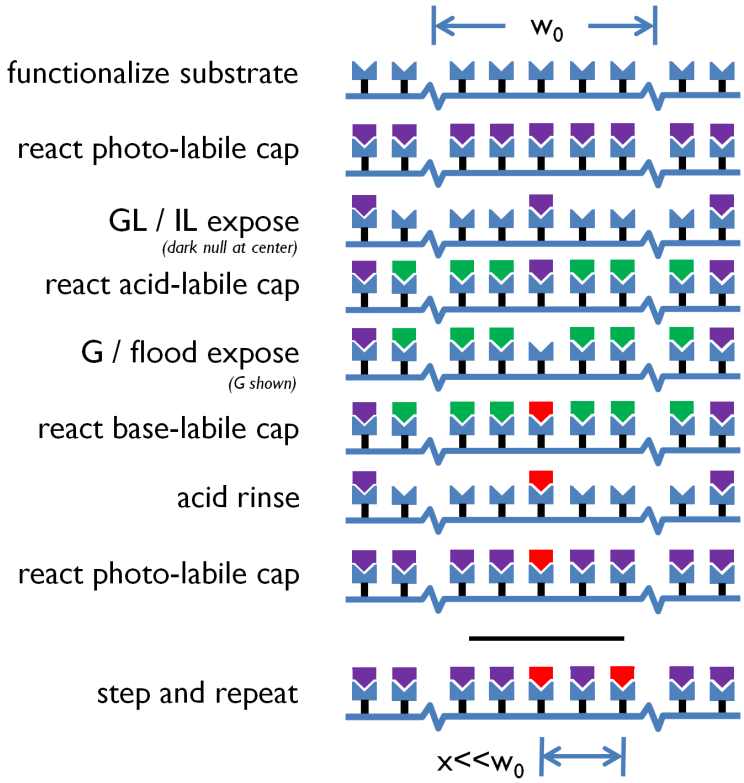

Figure 8.2: Proposed scheme for near-UV molecular lithography, with w_0 indicating extent of the diffraction limited spot across transverse length x. Three orthogonal protecting groups are used, but only one is photolabile. G and GL beams are used for the first and second optical exposures, respectively. Alternatively, interference lithography (IL) may be used for the first exposure and followed by uniform illumination for the second exposure. The purpose of the pH-labile cap (green) is to temporarily mask the region exposed by the 1st pattern. Once the deprotected regions have been masked, subdiffraction photosensitive areas that remain may be photo-deprotected and terminated by irreversible coupling with acetic anhydride (red). After acetylation, the pH-labile groups (green) are removed with in-situ wet processing and replaced with the original photo-labile groups (purple) to restore the original surface everywhere except the subdiffraction terminated areas (red). The process is repeated with a transverse spatial shift to achieve superresolution of the acetylated groups. After patterning is complete, the non-acetylated areas may be reacted with a useful functionality such as nanoparticles or precursor to an epitaxially-grown resist.

between the substrate and amine, forming an end-functionalized polymer brush. Presumably similar to solution reaction, NVOC-Cl was reacted directly onto the surface-tethered amine groups. Further reactions involving fluorescent probes confirmed successful protection / photo-deprotection of the brush. While convenient for assay readout with an optical micro-

scope, fluorophores are inappropriate for general use as nanolithographic probes. Reactive nanoparticles, on the other hand, should be visible with SEM or AFM imaging.

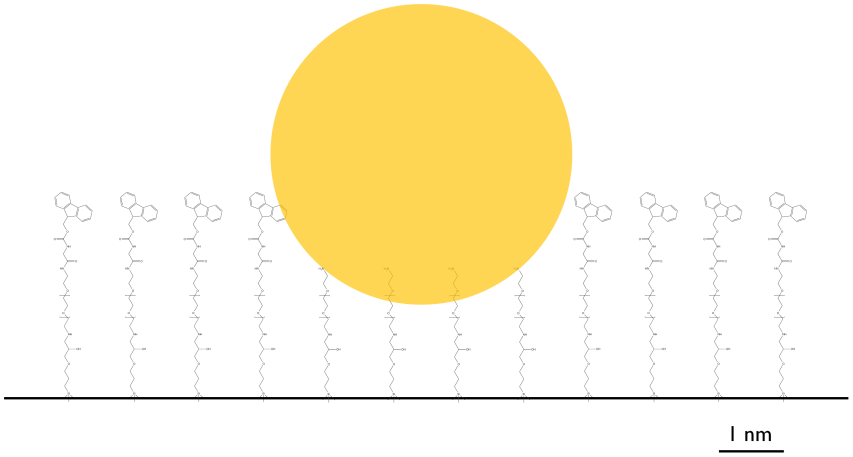

Figure 8.3: Cartoon comparing a 5-nm gold nanoparticle to the PEG-amine brush surface packing density. Individual polymer chains are not to scale. The 3,000 Da (n ≈ 70) PEG-diamine used here in these preliminary surface patterning studies was chosen for convenience; resolution optimization would likely require shorter spacers to provide a shorter radius-of-gyration.

8.3 Methods and preliminary results

Instead, I have sought to combine aspects of the Vossmeyer [225] and Waichman [231] approaches that are advantageous for multi-step nanolithography. Figures 8.4 and 8.5 show preliminary results from a new approach: The surface is prepared by treating Nanostrip-cleaned slides first with 3-glycidoxypropyltrimethoxysilane, then with melted 3000-MW diamine-PEG. Both treatments are done with neat liquids, using only a few droplets between slides mounted face-to-face (to conserve material and prevent contamination). After preparation of the brush, slides are incubated in a solution of NVOC-Cl saturated chloroform at 60 °C for 30 min. To prevent evaporation, a sealed Mason jar may be used for immediate

containment inside an oven. Lid replacement should be done with each cycle, as chloroform vapor may attack the narrow rubber gasket at the lid edge. This sequence of processing steps should result in an NVOC-protected, surface-tethered amine brush.

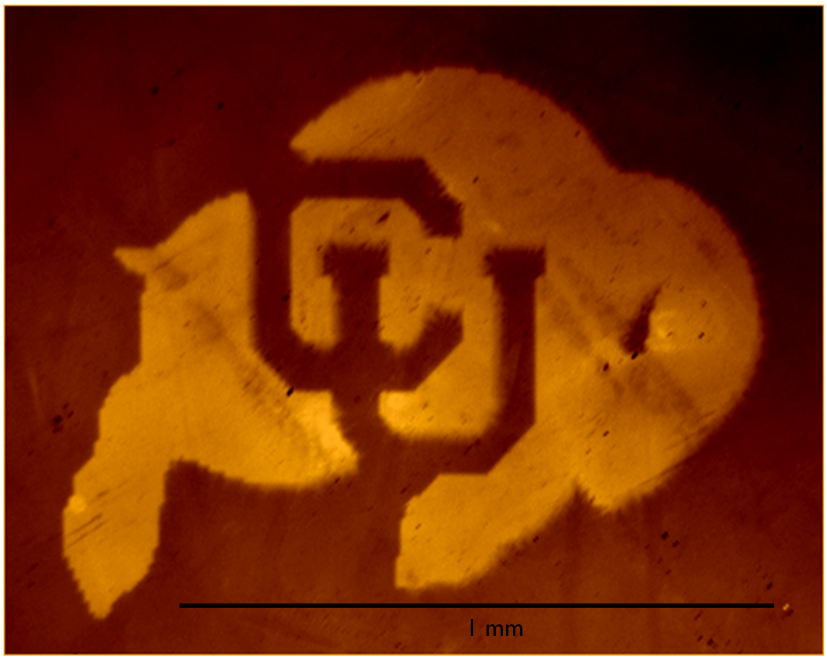

Figure 8.4: Optical micrograph of preliminary amine test-pattern, decorated with gold nanoparticles.

To test photodeprotection of the amine groups, NVOC-treated slides were exposed to a 50 mW, 1.5 mm diameter Ar+ laser beam ($\lambda = 364$ nm) for 10 s. Patterned deprotection was tested with the same exposure against a chrome mask. To prevent an aldehyde-forming back-reaction, the surface was covered in methanol with 30 mM semicarbazide during exposure. Afterwards, samples were washed in DI water and placed in colloidal gold (Bio-rad colloidal gold total protein stain). After incubation at 5 °C for 4 h, samples were removed, rinsed in DI water and dried in N_2. Inspection by optical microscope in DIC mode, as shown in Fig. 8.5, revealed well-defined patterns with uniform gold coverage in exposed areas and low gold coverage in unexposed areas. High frequency edge-ringing is clearly visible at high

magnification, promising potential for high-resolution patterning.

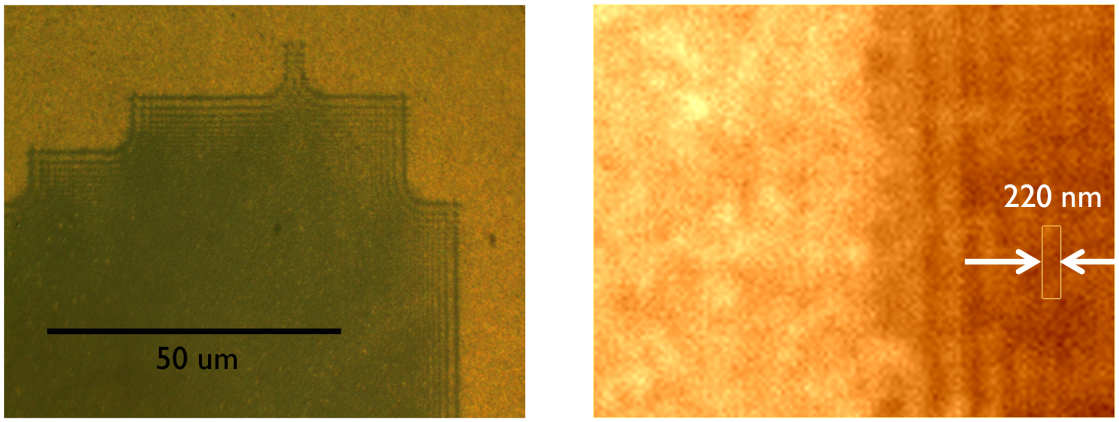

Figure 8.5: Increased-magnification DIC optical micrograph of nanoparticle-decorated, patterned amine brush. Edge diffraction across the small mask / sample gap creates a finely-spaced intensity ringing, which is optically resolvable in the gold nanoparticle pattern.

Direct SEM imaging of gold nanoparticles on glass is made difficult by charge accumulation, but the effect is significantly reduced by using Si wafers for substrates. SEM images are shown in Fig. 8.6. Although similar to the optical micrographs, the SEM images contain details that may suggest a small amount of nanoparticle agglomeration. Such effects are commonly described in the nanoparticle literature, and in this case it may be possible to use agglomeration to enhance surface coverage.

8.4 Resolution scaling analysis

Interference lithography is well-suited for submicron patterning across large areas, typically applied to photoresist-coated wafers. Given that the point-wise discrete nature of surface-tethered patterning is a significant departure from typical resist patterning, a set of simulations was undertaken to learn about patterning behavior. Figure 8.8 shows sur-

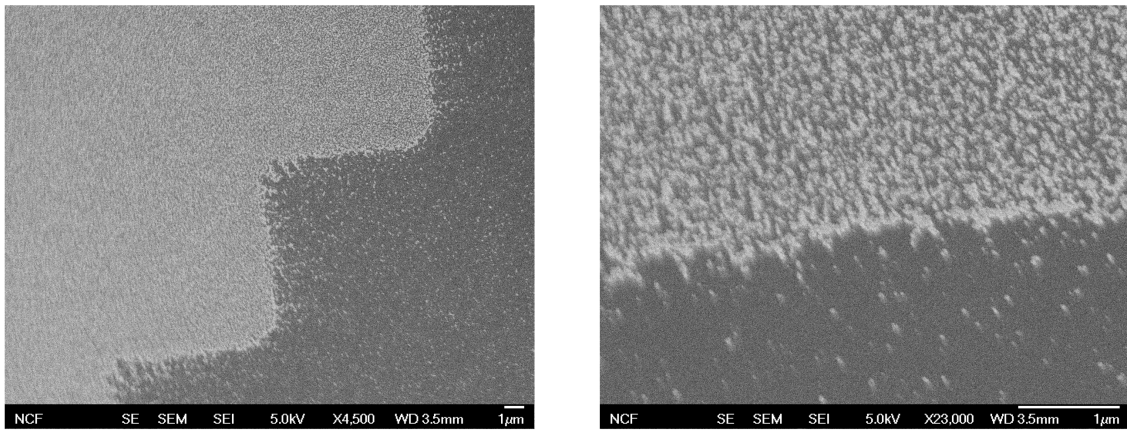

Figure 8.6: SEM photo of amine / gold pattern. Electron microscope imaging of nanoparticle-decorated PEG-diamine patterns is made possible by the use of a semiconducting substrate, which provides enough conductivity to prevent surface charging. Here, the epoxide silane brush precursor has been coupled onto a silicon wafer. Granularity or roughness in these preliminary patterns may indicate nanoparticle aggregation effects.

face maps of deprotection probability P(x,y), following the specified optical energy dose. Dose units are chosen so that the fraction 1/e of original protecting groups remain after an exposure of dose = 1. Feature size reduction is observed to go by d $\sim 1/\sqrt{\text{dose}}$.

Similarly, a Monte-Carlo analysis shown in Fig. 8.10 simulates an actual outcome of particle-site attachment. Surface modification with photolabile groups is represented adding small circles to random locations across an initially empty square, without overlap, until no more can be added. Next, optical exposure is simulated by randomly removing circles according to the removal probability P(x,y) shown in Fig. 8.8. Pattern definition is rough at the edges, as expected, though it may be possible to sharpen the edge response with coordinative-bonding or multiple-processing strategies.

The interference simulations show the potential for large-area patterning with highly enhanced confinement, by the combination of surface patterning with interference lithog-

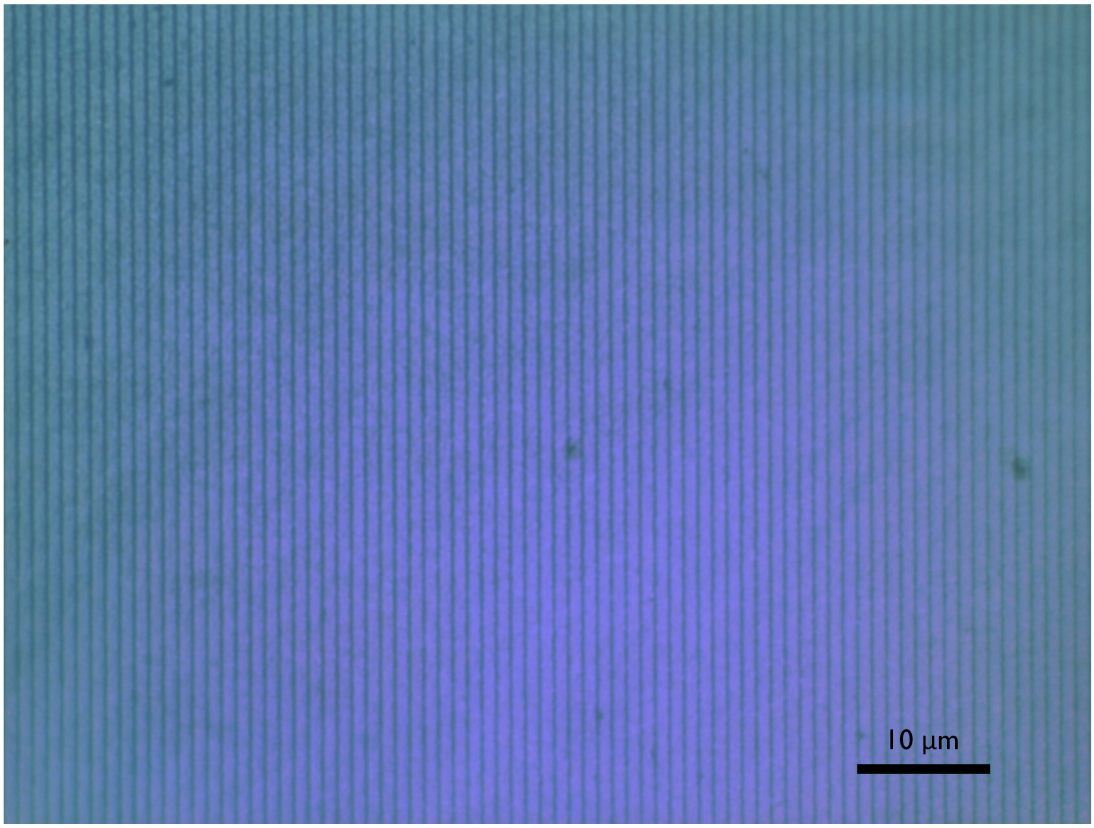

Figure 8.7: Preliminary single exposure interference-patterned results. Exposure to two interfering $\lambda = 364$ nm beams creates a fringe pattern at the sample, inducing deprotection of surface-tethered, amine-functionalized PEG chains. Subsequent incubation in a solution of 25-nm gold particles results in attachment to deprotected site.

raphy. With additional processing steps shown in 8.2, unexposed features are transferred to a non-photosensitive functionality and the remaining surface is refreshed to the original state. Further exposures and processing may be used to incrementally add fine-detail until the pattern is complete.

Although multiple exposures and increased doses are required, this superresolution scheme has a number of advantages: Confinement and writing are decoupled into separate process steps, allowing them to be independently optimized. For instance, there is no limit on the amount of enhanced confinement that one exposure cycle can impose on another exposure cycle. While multiple protection and deprotection reactions are necessary, the success of

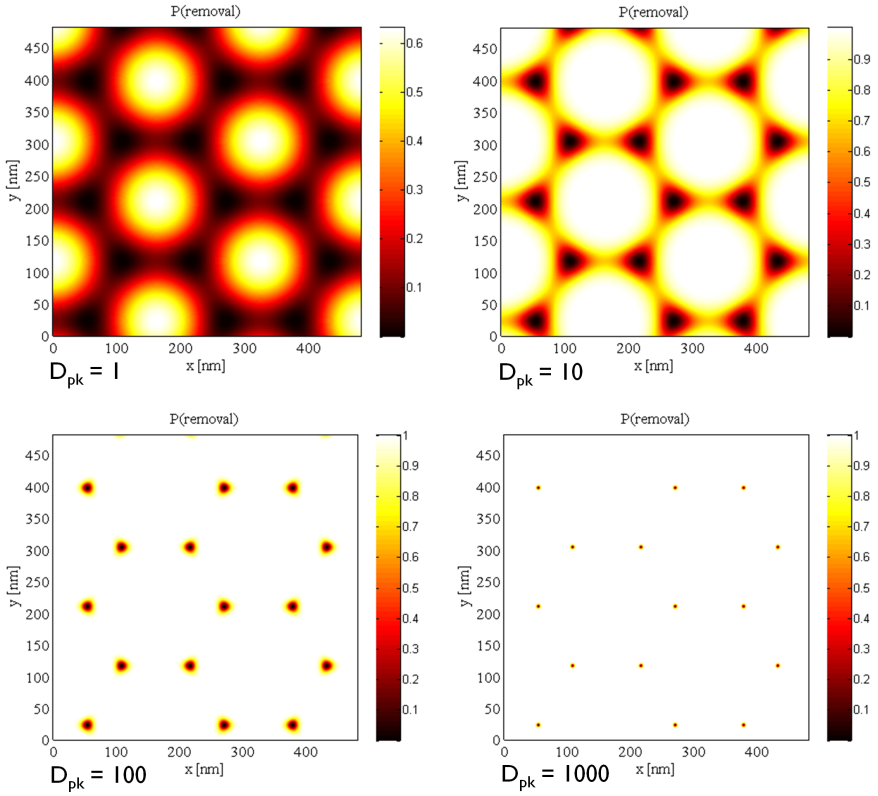

Figure 8.8: Probability of deprotection for various exposures to a 3-beam interference pattern, $\lambda = 365$ nm, NA = 1.3.

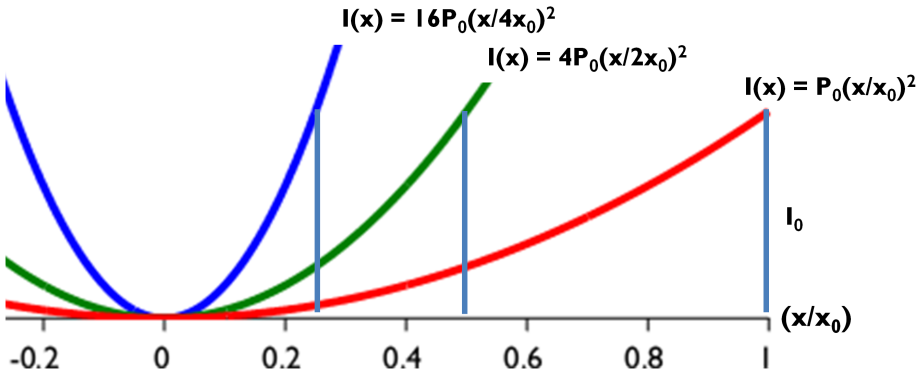

Figure 8.9: Inverse square-root confinement scaling with exposure. Assuming a fixed interfering-beam exposure interval and assigning I_0 as the threshold local intensity to reach an arbitrary degree of average deprotection, feature-width of the remaining protected group is $d \sim 1/\sqrt{P}$. This scaling is evident in the very large doses required for high confinement as shown in Fig. 8.8 and 8.10. If confinement is induced by photogenerated radical scavengers that regenerate by fast recombination, as discussed in Chap. 7, $d \sim 1/\sqrt[4]{P}$.

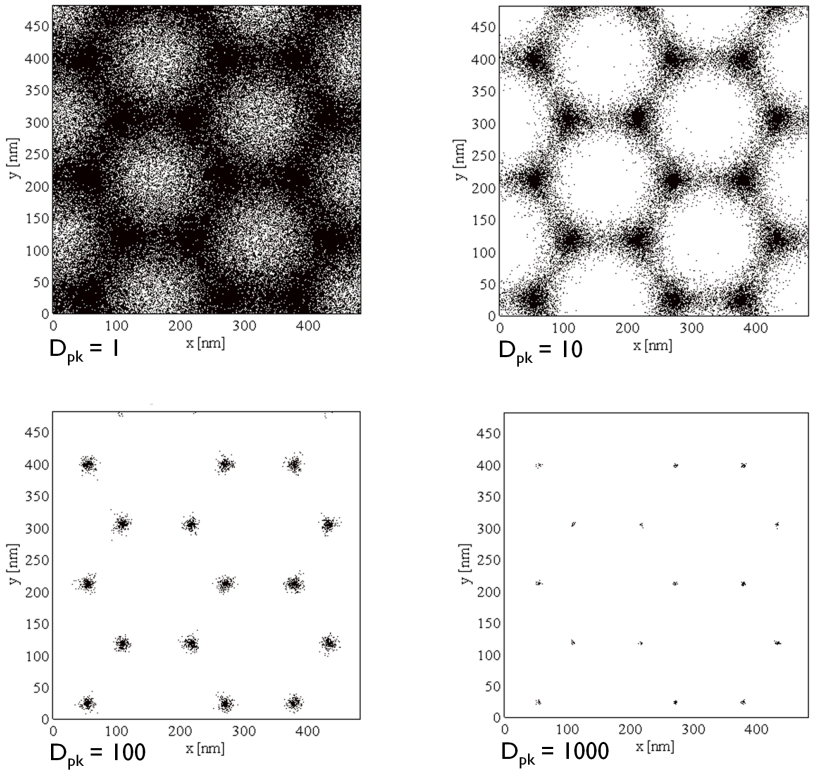

Figure 8.10: Monte-Carlo simulation of discrete deprotection events, for various exposures to a 3-beam interference pattern, $\lambda = 365$ nm, NA = 1.3. The stochastic nature of molecular photo-deprotection leaves functional patterns without well-defined edges. Subsequent reactions requiring multiple adjacent reactive groups, such as cooperative binding, may allow pattern "clean-up" by a thresholding effect.

maskless array synthesizers (see, for example [169]) suggests the intriguing possibility of performing these reactions in-place and thus eliminating the need for pattern registration with each cycle. With typical photo-deprotection mechanisms [187], oxygen elimination during exposure is not required. This allows much more flexibility in system design, including the use of conventional front-side illumination and high-index immersion fluids. Finally, the surface-tethered nature of the patterning restricts diffusion to molecular radius-of-gyration. This is perhaps most important of all, potentially enabling lithography at resolutions even finer than allowed in e-beam writing.

Bibliography

[1] C. Agbavwe, C. Kim, D. Hong, K. Heinrich, T. Wang, and M. M. Somoza. Efficiency, error and yield in light-directed maskless synthesis of dna microarrays. Journal of Nanobiotechnology, 9(1):1–17, 2011.

[2] S. A. Ahmad, L. S. Wong, J. Hobbs, G. Leggett, and J. Micklefield. Micrometer- and nanometer-scale photopatterning using 2-nitrophenylpropyloxycarbonyl-protected aminosiloxane monolayers. Journal of the American Chemical Society, 131(4):1513–1522, 2009.

[3] C.-N. Ahn, K.-H. Baik, Y.-S. Lee, H.-E. Kim, I. Hur, Y. Kim, J.-H. Kim, and S.-H. Choi. Study of optical proximity effects using off-axis illumination with attenuated phase shift mask. In SPIE's 1995 Symposium on Microlithography, pages 222–239. International Society for Optics and Photonics, 1995.

[4] M. lvarez, J. M. Alonso, O. Filevich, M. Bhagawati, R. Etchenique, J. Piehler, and A. del Campo. Modulating surface density of proteins via caged surfaces and controlled light exposure. Langmuir, 27(6):2789–2795, 2011.

[5] M. lvarez, A. Best, S. PradhanKadam, K. Koynov, U. Jonas, and M. Kreiter. Single photon and twophoton induced photocleavage for monolayers of an alkyltriethoxysilane with a photoprotected carboxylic ester. Advanced Materials, 20(23):4563–4567, 2008.

[6] R. P. Andres, J. D. Bielefeld, J. I. Henderson, D. B. Janes, V. R. Kolagunta, C. P. Kubiak, W. J. Mahoney, and R. G. Osifchin. Self-assembly of a two-dimensional superlattice of molecularly linked metal clusters. Science, 273(5282):1690–1693, 1996.

[7] T. L. Andrew, H.-Y. Tsai, and R. Menon. Confining light to deep subwavelength dimensions to enable optical nanopatterning. Science, 324(5929):917–921, 2009.

[8] K. S. Anseth, C. M. Wang, and C. N. Bowman. Kinetic evidence of reaction diffusion during the polymerization of multi(meth)acrylate monomers. Macromolecules, 27(3):650–655, 1994.

[9] E. M. Arnold and C. B. Subwavelength direct-write nanopatterning using optically trapped microspheres. Nature Nanotechnology, 3:5, 2008.

[10] K. Aslan and V. H. Prez-Luna. Surface modification of colloidal gold by chemisorption of alkanethiols in the presence of a nonionic surfactant. Langmuir, 18(16):6059–6065, 2002.

[11] S. Asmusen, G. Arenas, W. D. Cook, and C. Vallo. Photobleaching of camphorquinone during polymerization of dimethacrylate-based resins. Dental Materials, 25(12):1603–1611, 2009.

[12] M. Atai, M. Ahmadi, S. Babanzadeh, and D. C. Watts. Synthesis, characterization, shrinkage and curing kinetics of a new low-shrinkage urethane dimethacrylate monomer for dental applications. Dental Materials, 23(8):1030–1041, 2007.

[13] P. Avouris, W. D. Hopewell, and M. A. Elsayed. Energy-dependence of nonradiative electronic relaxation in camphorquinone vapor. Journal of Chemical Physics, 66(3):1376–1377, 1977.

[14] D. Axelrod, D. Koppel, J. Schlessinger, E. Elson, and W. Webb. Mobility measurement by analysis of fluorescence photobleaching recovery kinetics. Biophysical journal, 16(9):1055, 1976.

[15] R. Barbey, L. Lavanant, D. Paripovic, N. Schuwer, C. Sugnaux, S. Tugulu, and H.-A. Klok. Polymer brushes via surface-initiated controlled radical polymerization: synthesis, characterization, properties, and applications. Chemical reviews, 109(11):5437–5527, 2009.

[16] R. J. Barsotti Jr. Chemically directed assembly of monolayer protected gold nanoparticles on lithographically generated patterns. Journal of Materials Chemistry, 16(10):962–965, 2006.

[17] M. Beier and J. D. Hoheisel. Production by quantitative photolithographic synthesis of individually quality checked dna microarrays. Nucleic Acids Research, 28(4):e11–e11, 2000.

[18] J. L. Belletire, R. J. Rauh, and Y. L. Hurou. Semicarbazide. e-EROS Encyclopedia of Reagents for Organic Synthesis, 2006.

[19] M. G. Bellino, E. J. Calvo, and G. Gordillo. Adsorption kinetics of charged thiols on gold nanoparticles. Physical Chemistry Chemical Physics, 6(2):424–428, 2004.

[20] H. E. Bennett. Scattering characteristics of optical materials. Optical Engineering, 17(5):175480–175480–, 1978.

[21] J. E. Bennett, H. Sieper, and P. Tavs. 2,2,6,6-tetramethylpiperidyl-1-thiyl - a stable new radical. Tetrahedron, 23(4):1697–&, 1967.

[22] D. Berk, F. Yuan, M. Leunig, and R. Jain. Fluorescence photobleaching with spatial fourier analysis: measurement of diffusion in light-scattering media. Biophysical journal, 65(6):2428–2436, 1993.

[23] D. Bethell, M. Brust, D. Schiffrin, and C. Kiely. From monolayers to nanostructured materials: an organic chemist's view of self-assembly. Journal of Electroanalytical Chemistry, 409(1):137–143, 1996.

[24] S. Beuermann, M. Buback, T. P. Davis, R. G. Gilbert, R. A. Hutchinson, O. F. Olaj, G. T. Russell, J. Schweer, and A. M. van Herk. Critically evaluated rate coefficients for free-radical polymerization, 2.. propagation rate coefficients for methyl methacrylate. Macromolecular Chemistry and Physics, 198(5):1545–1560, 1997.

[25] S. Beun, C. Bailly, A. Dabin, J. Vreven, J. Devaux, and G. Leloup. Rheological properties of experimental bis-gma/tegdma flowable resin composites with various macrofiller/microfiller ratio. Dental Materials, 25(2):198–205, 2009.

[26] K. Y. Bliokh, E. A. Ostrovskaya, M. A. Alonso, O. G. Rodriguez-Herrera, D. Lara, and C. Dainty. Spin-to-orbital angular momentum conversion in focusing, scattering, and imaging systems. Optics Express, 19(27):26132–26149, 2011.

[27] D. Bonn, J. Eggers, J. Indekeu, J. Meunier, and E. Rolley. Wetting and spreading. Reviews of Modern Physics, 81(2):739, 2009.

[28] A. N. Boto, P. Kok, D. S. Abrams, S. L. Braunstein, C. P. Williams, and J. P. Dowling. Quantum interferometric optical lithography: Exploiting entanglement to beat the diffraction limit. Physical Review Letters, 85(13):2733–2736, 2000.

[29] C. N. Bowman and C. J. Kloxin. Toward an enhanced understanding and implementation of photopolymerization reactions. AIChE Journal, 54(11):2775–2795, 2008.

[30] D. A. Braden, E. E. Parrack, and D. R. Tyler. Photochemical studies as a function of solvent viscosity. a new photochemical pathway in the reaction of (5-c5h4me) 2mo2 (co) 6 with ccl4. Photochemical & Photobiological Sciences, 1(6):418–420, 2002.

[31] R. Bradley, M. Evans, and R. Whytlaw-Gray. The rate of evaporation of droplets. evaporation and diffusion coefficients, and vapour pressures of dibutyl phthalate and butyl stearate. Proceedings of the Royal Society of London. Series A. Mathematical and Physical Sciences, 186(1006):368–390, 1946.

[32] N. Bricklebank and A. Pryke. 2,2,6,6-tetramethylpiperidin-1-ylthiyl, the sulfur analogue of tempo, as an initiator for the controlled radical polymerisation of styrene. Journal of the Chemical Society-Perkin Transactions 1, (18):2048–2051, 2002.

[33] A. H. Broderick, M. R. Lockett, M. E. Buck, Y. Yuan, L. M. Smith, and D. M. Lynn. In situ synthesis of oligonucleotide arrays on surfaces coated with crosslinked polymer multilayers. Chemistry of Materials, 24(5):938–945, 2011.

[34] A. Broers. Resolution limits for electron-beam lithography. IBM Journal of Research and Development, 32(4):502–513, 1988.

[35] T. Brunner, Z. Chen, K.-J. Chen, and S. Scheer. A new long range proximity effect in chemically amplified photoresist processes: chemical flare. In Microlithography 2005, pages 261–268. International Society for Optics and Photonics, 2005.

[36] M. Brust, D. Bethell, C. J. Kiely, and D. J. Schiffrin. Self-assembled gold nanoparticle thin films with nonmetallic optical and electronic properties. Langmuir, 14(19):5425–5429, 1998.

[37] S. Buhler, I. Lagoja, H. Giegrich, K. P. Stengele, and W. Pfleiderer. New types of very efficient photolabile protecting groups based upon the [2 (2-nitrophenyl) propoxy] carbonyl (nppoc) moiety. Helvetica Chimica Acta, 87(3):620–659, 2004.

[38] Y. Y. Cao, Z. S. Gan, B. H. Jia, R. A. Evans, and M. Gu. High-photosensitive resin for super-resolution direct-laser-writing based on photoinhibited polymerization. Optics Express, 19(20):19486–19494, 2011.

[39] A. Carre, W. Birch, and V. Lacarriere. Glass substrates modified with organosilanes for dna immobilization. Silanes and Other Couping Agents, 4:113, 2007.

[40] K. Chan and K. K. Gleason. Initiated chemical vapor deposition of linear and cross-linked poly (2-hydroxyethyl methacrylate) for use as thin-film hydrogels. Langmuir, 21(19):8930–8939, 2005.

[41] J.-K. Chen and A.-L. Zhuang. Fabrication of a highly dense line patterned polystyrene brush on silicon surfaces using very large scale integration processing. The Journal of Physical Chemistry C, 114(27):11801–11809, 2010.

[42] S. Chen and L. M. Smith. Photopatterned thiol surfaces for biomolecule immobilization. Langmuir, 25(20):12275–12282, 2009.

[43] Y.-C. Chen, J. L. Ferracane, and S. A. Prahl. Quantum yield of conversion of the photoinitiator camphorquinone. dental materials, 23(6):655–664, 2007.

[44] X. Chevalier, C. Nicolet, R. Tiron, A. Gharbi, M. Argoud, J. Pradelles, M. Delalande, G. Cunge, G. Fleury, and G. Hadziioannou. Scaling-down lithographic dimensions with block-copolymer materials: 10nmsized features with ps-b-pmma. In SPIE Advanced Lithography, pages 868006–868006–10. International Society for Optics and Photonics, 2013.

[45] S. R. Chhabra, A. N. Khan, and B. W. Bycroft. Versatile dde-based primary amine linkers for solid phase synthesis. Tetrahedron letters, 39(21):3585–3588, 1998.

[46] S.-D. Cho, H.-K. Kim, H.-s. Yim, M.-R. Kim, J.-K. Lee, J.-J. Kim, and Y.-J. Yoon. Suzukimiyaura coupling reaction of aryl chlorides using di (2, 6-dimethylmorpholino) phenylphosphine as ligand. Tetrahedron, 63(6):1345–1352, 2007.

[47] S. Y. Chou, P. R. Krauss, and P. J. Renstrom. Imprint of sub-25 nm vias and trenches in polymers. Applied physics letters, 67:3114, 1995.

[48] K. L. Christman, M. V. Requa, V. D. Enriquez-Rios, S. C. Ward, K. A. Bradley, K. L. Turner, and H. D. Maynard. Submicron streptavidin patterns for protein assembly. Langmuir, 22(17):7444–7450, 2006.

[49] G. Chumanov, K. Sokolov, B. W. Gregory, and T. M. Cotton. Colloidal metal films as a substrate for surface-enhanced spectroscopy. The Journal of Physical Chemistry, 99(23):9466–9471, 1995.

[50] W. D. Cook. Photopolymerization kinetics of dimethacrylates using the camphorquinone/amine initiator system. Polymer, 33(3):600–609, 1992.

[51] J. Crank. The Mathematics of Diffusion: 2d Ed. Clarendon Press, 1975.

[52] R. Craster and O. Matar. Dynamics and stability of thin liquid films. Reviews of modern physics, 81(3):1131, 2009.

[53] J. Cui, V. S. Miguel, and A. del Campo. Light triggered multifunctionality at surfaces mediated by photolabile protecting groups. Macromolecular Rapid Communications, 2012.

[54] B. H. Cumpston, S. P. Ananthavel, S. Barlow, D. L. Dyer, J. E. Ehrlich, L. L. Erskine, A. A. Heikal, S. M. Kuebler, I.-Y. S. Lee, and D. McCord-Maughon. Two-photon polymerization initiators for three-dimensional optical data storage and microfabrication. Nature, 398(6722):51–54, 1999.

[55] G. P. Cunningham, G. A. Vidulich, and R. L. Kay. Several properties of acetonitrile-water, acetonitrile-methanol, and ethylene carbonate-water systems. Journal of Chemical and Engineering Data, 12(3):336–337, 1967.

[56] J. Cusido, S. Impellizzeri, and F. M. Raymo. Molecular strategies to read and write at the nanoscale with far-field optics. Nanoscale, 3(1):59–70, 2011.

[57] P.-G. De Gennes. Wetting: statics and dynamics. Reviews of Modern Physics, 57(3):827, 1985.

[58] P. De Heen. La vitesse de vaporisation de liquides [vaporization rates of liquids]. J Chimie Physique, 11:205–213, 1913.

[59] P. Debye. Reaction rates in ionic solutions. Transactions of the Electrochemical Society, 82(1):265–272, 1942.

[60] C. Decker and K. Moussa. Real-time kinetic study of laser-induced polymerization. Macromolecules, 22(12):4455–4462, 1989.

[61] P. R. Delgadillo, M. Suri, S. Durant, A. Cross, V. R. Nagaswami, D. Van Den Heuvel, R. Gronheid, and P. Nealey. Defect source analysis of directed self-assembly process. Journal of Micro/Nanolithography, MEMS, and MOEMS, 12(3):031112–031112, 2013.

[62] R. M. Diebold and D. R. Clarke. Lithographic patterning on polydimethylsiloxane surfaces using polydimethylglutarimide. Lab on a Chip, 11(9):1694–1697, 2011.

[63] J. Drelich and E. Chibowski. Superhydrophilic and superwetting surfaces: definition and mechanisms of control. Langmuir, 26(24):18621–18623, 2010.

[64] M. Dufva. Fabrication of high quality microarrays. Biomolecular engineering, 22(5):173–184, 2005.

[65] Y. Y. Durmaz, N. Moszner, and Y. Yagci. Visible light initiated free radical promoted cationic polymerization using acylgermane based photoinitiator in the presence of onium salts. Macromolecules, 41(18):6714–6718, 2008.

[66] D. Ennis, H. Betz, and H. Ade. Direct spincasting of polystyrene thin films onto poly (methyl methacrylate). Journal of Polymer Science Part B: Polymer Physics, 44(22):3234–3244, 2006.

[67] Esstech Inc. Product info sheet, urethane dimethacrylate. Electronic resource, retrieved from http://www.esstechinc.com, 2014.

[68] N. Fang, C. Sun, and X. Zhang. Diffusion-limited photopolymerization in scanning micro-stereolithography. Applied Physics A, 79(8):1839–1842, 2004.

[69] R. P. Feynman. There's plenty of room at the bottom. Engineering and science, 23(5):22–36, 1960.

[70] J. Fischer, G. von Freymann, and M. Wegener. The materials challenge in diffraction-unlimited direct-laser-writing optical lithography. Advanced Materials, 22(32):3578–3582, 2010.

[71] J. Fischer and M. Wegener. Three-dimensional direct laser writing inspired by stimulated-emission-depletion microscopy [invited]. Optical Materials Express, 1(4):614–624, 2011.

[72] J. Fischer and M. Wegener. Ultrafast polymerization inhibition by stimulated emission depletion for threedimensional nanolithography. Advanced Materials, 24(10):OP65–OP69, 2012.

[73] P. J. Flory. The configuration of real polymer chains. The Journal of Chemical Physics, 17:303, 1949.

[74] S. Fodor, J. Read, M. Pirrung, L. Stryer, A. Lu, and D. Solas. Light-directed, spatially addressable parallel chemical synthesis. Science, 251(4995):767–773, 1991.

[75] D. L. Forman, M. C. Cole, and R. R. McLeod. Radical diffusion limits to photoinhibited superresolution lithography. Physical Chemistry Chemical Physics, 15(36):14862–14867, 2013.

[76] D. L. Forman, G. L. Heuvelman, and R. R. McLeod. Materials development for photo-inhibited super-resolution (pinsr) lithography. In SPIE MOEMS-MEMS, pages 824904–824904–9. International Society for Optics and Photonics, 2012.

[77] H. Fouckhardt, I. Steingoetter, M. Brinkmann, M. Hagemann, H. Zarschizky, and L. Zschiedrich. nm-and m-scale surface roughness on glass with specific optical scattering characteristics on demand. Advances in OptoElectronics, 2007, 2007.

[78] J. T. Fourkas and J. S. Petersen. 2-colour photolithography. Physical Chemistry Chemical Physics, 16(19):8731–8750, 2014.

[79] R. Frings and W. Schnabel. Photoreactions of trans-poly (vinyl cinnamate) and low molecular weight model compoundspart i. Polymer Photochemistry, 3(5):325–339, 1983.

[80] Z. Gan, Y. Cao, R. A. Evans, and M. Gu. Three-dimensional deep sub-diffraction optical beam lithography with 9 nm feature size. Nature communications, 4, 2013.

[81] Z. S. Gan, Y. Y. Cao, B. H. Jia, and M. Gu. Dynamic modeling of superresolution photoinduced-inhibition nanolithography. Optics Express, 20(15):16871–16879, 2012.

[82] T. Garrett, J. Umbenhaucr, G. Romberg, A. Smith, M. Goulden, J. Engle, and M. Harris. Nosyl as an efficient protecting group for the synthesis of bipyridine aza-crown ether macrocycles. Journal of Undergraduate Chemistry Research, 2008.

[83] M. Gauthier, I. Stangel, T. Ellis, and X. Zhu. Oxygen inhibition in dental resins. Journal of dental research, 84(8):725–729, 2005.

[84] P. Geelen. Light switchable coatings. Thesis, Technische Universiteit Eindhoven, 2008.

[85] I. Gelest, B. C. Arkles, and G. L. Larson. Silicon Compounds: Silanes and Silicones: a Survey of Properties and Chemistry. Gelest, Incorporated, 2004.

[86] S. M. George, B. Yoon, and A. A. Dameron. Surface chemistry for molecular layer deposition of organic and hybrid organic inorganic polymers. Accounts of chemical research, 42(4):498–508, 2009.

[87] H. F. Gibbard and J. L. Creek. Vapor pressure of methanol from 288.15 to 337.65. deg. k. Journal of Chemical and Engineering Data, 19(4):308–310, 1974.

[88] F. Goncalves, Y. Kawano, C. Pfeifer, J. W. Stansbury, and R. R. Braga. Influence of bisgma, tegdma, and bisema contents on viscosity, conversion, and flexural strength of experimental resins and composites. European journal of oral sciences, 117(4):442–446, 2009.

[89] C. A. Goss, D. H. Charych, and M. Majda. Application of (3-mercaptopropyl) trimethoxysilane as a molecular adhesive in the fabrication of vapor-deposited gold electrodes on glass substrates. Analytical chemistry, 63(1):85–88, 1991.

[90] G. Gotesman and R. Naaman. Selective surface patterning for the coadsorption of self-assembled gold and semiconductor nanoparticles. Langmuir, 24(12):5981–5983, 2008.

[91] T. W. Greene, P. G. Wuts, and J. Wiley. Protective groups in organic synthesis, volume 168. Wiley New York, 1999.

[92] S. Grill and E. Stelzer. Method to calculate lateral and axial gain factors of optical setups with a large solid angle. JOSA A, 16(11):2658–2665, 1999.

[93] W. Haiss, N. T. Thanh, J. Aveyard, and D. G. Fernig. Determination of size and concentration of gold nanoparticles from uv-vis spectra. Analytical Chemistry, 79(11):4215–4221, 2007.

[94] B. Harke, P. Bianchini, F. Brandi, and A. Diaspro. Photopolymerization inhibition dynamics for sub-diffraction direct laser writing lithography. Chemphyschem, 13(6):1429–1434, 2012.

[95] W. Haske, V. W. Chen, J. M. Hales, W. Dong, S. Barlow, S. R. Marder, and J. W. Perry. 65 nm feature sizes using visible wavelength 3-d multiphoton lithography. Optics Express, 15:3426–3436, 2007.

[96] H.-X. He, H. Zhang, Q. G. Li, T. Zhu, S. Li, and Z.-F. Liu. Fabrication of designed architectures of au nanoparticles on solid substrate with printed self-assembled monolayers as templates. Langmuir, 16(8):3846–3851, 2000.

[97] S. W. Hell and J. Wichmann. Breaking the diffraction resolution limit by stimulated emission: stimulated-emission-depletion fluorescence microscopy. Opt. Lett., 19(11):780–782, 1994.

[98] R. H. Henchman. Diffusion of Small Molecules in Amorphous Glassy Polymers. Thesis, University of Sydney, 1995.

[99] N. Herzer, C. Haensch, S. Hoeppener, and U. S. Schubert. Orthogonal functionalization of silicon substrates using self-assembled monolayers. Langmuir, 26(11):8358–8365, 2010.

[100] K. Hickman, J. Heckler, and N. Embree. Direct determination of low vapor pressures. Industrial & Engineering Chemistry Analytical Edition, 9(6):264–267, 1937.

[101] H. Hirai and H. Aizawa. Preparation of stable dispersions of colloidal gold in hexanes by phase transfer. Journal of colloid and interface science, 161(2):471–474, 1993.

[102] H. E. Hofmann. Evaporation rates of organic liquids. Industrial & Engineering Chemistry, 24(2):135–140, 1932.

[103] C. R. Hogg, Y. N. Picard, A. Narasimhan, J. A. Bain, and S. A. Majetich. Pattern transfer with stabilized nanoparticle etch masks. Nanotechnology, 24(8):085303, 2013.

[104] L. Huang, A. B. Braunschweig, W. Shim, L. D. Qin, J. K. Lim, S. J. Hurst, F. W. Huo, C. Xue, J. W. Jong, and C. A. Mirkin. Matrix-assisted dip-pen nanolithography and polymer pen lithography. Small, pages 1077–1081, 2010.

[105] A. M. Hung, C. M. Micheel, L. D. Bozano, L. W. Osterbur, G. M. Wallraff, and J. N. Cha. Large-area spatially ordered arrays of gold nanoparticles directed by lithographically confined dna origami. Nature nanotechnology, 5(2):121–126, 2009.

[106] Y. Iketaki, T. Watanabe, N. Bokor, and M. Fujii. Investigation of the center intensity of first- and second-order laguerre-gaussian beams with linear and circular polarization. Optics Letters, 32(16):2357–2359, 2007.

[107] H. Ishizaki. On the large deflections of rectangular glass panes under uniform pressure. Bulletin of the Disaster Prevention Research Institute, Kyoto University, 22(197 Part 1), 1972.

[108] H. Jacobsen and S. W. Hell. Effect of the specimen refractive index on the imaging of a confocal fluorescence microscope employing high aperture oil immersion lenses. Bioimaging, 3(1):39–47, 1995.

[109] J. Jakubiak, X. Allonas, J. P. Fouassier, A. Sionkowska, E. Andrzejewska, L. A. Linden, and J. F. Rabek. Camphorquinone-amines photoinitating systems for the initiation of free radical polymerization. Polymer, 44(18):5219–5226, 2003.

[110] B. Jia, J. Li, and M. Gu. Two-photon polymerization for three-dimensional photonic devices in polymers and nanocomposites. Australian journal of chemistry, 60(7):484–495, 2007.

[111] U. Jonas, A. del Campo, C. Krger, G. Glasser, and D. Boos. Colloidal assemblies on patterned silane layers. Proceedings of the National Academy of Sciences, 99(8):5034–5039, 2002.

[112] R. Jukaitis. Characterizing high numerical aperture microscope objective lenses, pages 21–43. Springer, 2003.

[113] T. Kamins. Metal-catalyzed silicon nanowires: Growth and devices. Presented at Stanford University Apr. 13, 2006.

[114] A. R. Kannurpatti, S. Lu, G. M. Bunker, and C. N. Bowman. Kinetic and mechanistic studies of iniferter photopolymerizations. Macromolecules, 29(23):7310–7315, 1996.

[115] O. Karlsson, J. Stubbs, L. Karlsson, and D. Sundberg. Estimating diffusion coefficients for small molecules in polymers and polymer solutions. Polymer, 42(11):4915–4923, 2001.

[116] S. Kawata, H.-B. Sun, T. Tanaka, and K. Takada. Finer features for functional microdevices. Nature, 412:2, 2001.

[117] J. Keizer. Nonequilibrium statistical thermodynamics and the effect of diffusion on chemical reaction rates. The Journal of Physical Chemistry, 86(26):5052–5067, 1982.

[118] S. Kenzhetaeva and L. Abulyaissova. Synthesis of 2-amino-4-phenylthiazole-derived thiuram disulfide. Russian Journal of General Chemistry, 83(11):2115–2116, 2013.

[119] I. Khudyakov, Y. I. Kiryukhin, and A. Yasmenko. Kinetics of geminate recombination of aromatic free radicals. Chemical Physics Letters, 74(3):462–466, 1980.

[120] I. Khudyakov, P. Levin, and V. Kuzmin. Kinetics of geminate recombination of organic free radicals in viscous solvents. Photochemical & Photobiological Sciences, 7(12):1540–1543, 2008.

[121] I. V. Khudyakov and N. J. Turro. Cage effect dynamics under photolysis of photoinitiators. Designed Monomers and Polymers, 13(5):487–496, 2010.

[122] H. Kilambi, S. K. Reddy, and C. N. Bowman. Kinetic and mechanistic studies of photopolymerizations of acrylates in the presence of iniferters. Macromolecules, 40(17):6131–6135, 2007.

[123] J. Kim. The precursor approach to patterned fluorescence images in polymer films. Macromolecular rapid communications, 28(11):1191–1212, 2007.

[124] G. R. Kinsley. Properly purge and inert storage vessels. Natural gas (Pittsburgh), 12:14.5, 2001.

[125] S. Kodama. Studies of the cage effect of solvent. iii. photolysis of azomethane in frozen solutions. Bulletin of the Chemical Society of Japan, 35(5):824–827, 1962.

[126] C. M. Kolodziej and H. D. Maynard. Electron-beam lithography for patterning biomolecules at the micron and nanometer scale. Chemistry of Materials, 24(5):774–780, 2012.

[127] I. Z. Kozma, P. Krok, and E. Riedle. Direct measurement of the group-velocity mismatch and derivation of the refractive-index dispersion for a variety of solvents in the ultraviolet. JOSA B, 22(7):1479–1485, 2005.

[128] P. M. Kunik. Surface percolation and growth. an alternative scheme for breaking the diffraction limit in optical patterning. Papers in Physics, 2009.

[129] C.-H. Kuo, T.-F. Chiang, L.-J. Chen, and M. H. Huang. Synthesis of highly faceted pentagonal-and hexagonal-shaped gold nanoparticles with controlled sizes by sodium dodecyl sulfate. Langmuir, 20(18):7820–7824, 2004.

[130] J. H. Lai. An investigation of spin coating of electron resists. Polymer Engineering & Science, 19(15):1117–1121, 1979.

[131] C. H. Lalander, Y. Zheng, S. Dhuey, S. Cabrini, and U. Bach. Dna-directed self-assembly of gold nanoparticles onto nanopatterned surfaces: controlled placement of individual nanoparticles into regular arrays. ACS nano, 4(10):6153–6161, 2010.

[132] J. Lalevee, X. Allonas, and J.-P. Fouassier. A new efficient photoiniferter for living radical photopolymerization. Macromolecules, 39(24):8216–8218, 2006.

[133] W. M. Lamanna, C. R. Kessel, P. M. Savu, Y. Cheburkov, S. Brinduse, T. A. Kestner, G. J. Lillquist, M. J. Parent, K. S. Moorhouse, and Y. Zhang. New ionic photo-acid generators (pags) incorporating novel perfluorinated anions. In Proceedings-SPIE The International Society for Optical Engineering, pages 817–828, 2002.

[134] R. Lvy, N. T. Thanh, R. C. Doty, I. Hussain, R. J. Nichols, D. J. Schiffrin, M. Brust, and D. G. Fernig. Rational and combinatorial design of peptide capping ligands for gold nanoparticles. Journal of the American Chemical Society, 126(32):10076–10084, 2004.

[135] C. J. Lawrence. The mechanics of spin coating of polymer-films. Physics of Fluids, 31(10):2786–2795, 1988.

[136] M.-H. Lee, H.-M. Kim, S.-Y. Cho, K. Lim, S.-Y. Park, J. Jong Lee, and K.-B. Kim. Fabrication of ultra-high-density nanodot array patterns (3 tbits/in. 2) using electron-beam lithography. Journal of Vacuum Science & Technology B: Microelectronics and Nanometer Structures, 29(6):061602–061602–5, 2011.

[137] S. Lee, H. S. Kang, and J. K. Park. High-resolution patterning of various large-area, highly ordered structural motifs by directional photofluidization lithography: Sub-30-nm line, ellipsoid, rectangle, and circle arrays. Advanced Functional Materials, 21(10):1770–1778, 2011.

[138] Y. Leterrier, B. Singh, J. Bouchet, J. A. E. Manson, G. Rochat, and P. Fayet. Super-tough uv-curable silane/silica gas barrier coatings on polymers. Surface & Coatings Technology, 203(22):3398–3404, 2009.

[139] P. P. Levin, I. V. Khudyakov, and V. A. Kuzmin. Geminate recombination kinetics of triplet radical pairs in glycerol: magnetic field effect. The Journal of Physical Chemistry, 93(1):208–214, 1989.

[140] H. Li, J. Zhang, X. Zhou, G. Lu, Z. Yin, G. Li, T. Wu, F. Boey, S. S. Venkatraman, and H. Zhang. Aminosilane micropatterns on hydroxyl-terminated substrates: fabrication and applications. Langmuir, 26(8):5603–5609, 2009.

[141] J.-R. Li, K. L. Lusker, J.-J. Yu, and J. C. Garno. Engineering the spatial selectivity of surfaces at the nanoscale using particle lithography combined with vapor deposition of organosilanes. ACS nano, 3(7):2023–2035, 2009.

[142] L. Li, R. R. Gattass, E. Gershgoren, H. Hwang, and J. T. Fourkas. Achieving lambda/20 resolution by one-color initiation and deactivation of polymerization. Science, 324(5929):3, 2009.

[143] S. Li, N. Marthandan, D. Bowerman, H. R. Garner, and T. Kodadek. Photolithographic synthesis of cyclic peptide arrays using a differential deprotection strategy. Chem. Commun., (5):581–583, 2005.

[144] Z. Li, M. Siklos, N. Pucher, K. Cicha, A. Ajami, W. Husinsky, A. Rosspeintner, E. Vauthey, G. Gescheidt, and J. Stampfl. Synthesis and structure activity relationship of several aromatic ketone based two photon initiators. Journal of Polymer Science Part A: Polymer Chemistry, 49(17):3688–3699, 2011.

[145] M. Lieder. Calculation of the standard potentials of the dithiocarbamate/thiuram disulfide redox system via thermochemical cycles and computational electrochemistry. Phosphorus Sulfur and Silicon and the Related Elements, 178(1):179–189, 2003.

[146] S.-Y. Lin, Y.-T. Tsai, C.-C. Chen, C.-M. Lin, and C.-h. Chen. Two-step functionalization of neutral and positively charged thiols onto citrate-stabilized au nanoparticles. The Journal of Physical Chemistry B, 108(7):2134–2139, 2004.

[147] S. Liu, R. Maoz, and J. Sagiv. Planned nanostructures of colloidal gold via self-assembly on hierarchically assembled organic bilayer template patterns with in-situ generated terminal amino functionality. Nano Letters, 4(5):845–851, 2004.

[148] D. J. Lougnot, P. Jost, and L. Lavielle. Polymers for holographic recording .6. some basic ideas for modelling the kinetics of the recording process. Pure and Applied Optics, 6(2):225–245, 1997.

[149] L. Lovell, B. Elliott, J. Brown, and C. Bowman. The effect of wavelength on the polymerization of multi (meth) acrylates with disulfide/benzilketal combinations. Polymer, 42(2):421–429, 2001.

[150] T. M. Lowry and J. O. Cutter. The rotatory dispersive power of organic compounds borneol, camphor, and camphorquinone. Journal of the Chemical Society, Transactions, 127:604–615, 1925.

[151] C. K. Luk and F. Richardson. Circularly polarized luminescence spectrum of camphorquinone. Journal of the American Chemical Society, 96(7):2006–2009, 1974.

[152] X. Q. Ma and J. S. Wei. Nanoscale lithography with visible light: optical nonlinear saturable absorption effect induced nanobump pattern structures. Nanoscale, 3(4):1489–1492, 2011.

[153] I. S. Maeng and J. W. Park. Patterning on self-assembled monolayers by low-energy electron-beam irradiation and its vertical amplification with atom transfer radical polymerization. Langmuir, 19(10):4519, 2003.

[154] U. Mansfeld, C. Pietsch, R. Hoogenboom, C. R. Becer, and U. S. Schubert. Clickable initiators, monomers and polymers in controlled radical polymerizationsa prospective combination in polymer science. Polymer Chemistry, 1(10):1560–1598, 2010.

[155] A. Maria Chong and X. Zhao. Functionalization of sba-15 with aptes and characterization of functionalized materials. The Journal of Physical Chemistry B, 107(46):12650–12657, 2003.

[156] G. Marriott. Caged protein conjugates and light-directed generation of protein activity: preparation, photoactivation, and spectroscopic characterization of caged g-actin conjugates. Biochemistry, 33(31):9092–9097, 1994.

[157] M. N. Martin, J. I. Basham, P. Chando, and S.-K. Eah. Charged gold nanoparticles in non-polar solvents: 10-min synthesis and 2d self-assembly. Langmuir, 26(10):7410–7417, 2010.

[158] T. A. Martin, C. T. Herman, F. T. Limpoco, M. C. Michael, G. K. Potts, and R. C. Bailey. Quantitative photochemical immobilization of biomolecules on planar and corrugated substrates: a versatile strategy for creating functional biointerfaces. ACS applied materials & interfaces, 3(9):3762–3771, 2011.

[159] L. Masaro and X. Zhu. Physical models of diffusion for polymer solutions, gels and solids. Progress in Polymer Science, 24(5):731–775, 1999.

[160] K. McCoy, C. Gumieny, D. W. Hess, L. M. Tolbert, and C. L. Henderson. Novel surface imaging method using surface monolayer initiated polymerization. In SPIE's 27th Annual International Symposium on Microlithography, pages 1025–1033. International Society for Optics and Photonics, 2002.

[161] G. Mehta, J. Lee, W. Cha, Y. C. Tung, J. J. Linderman, and S. Takayama. Hard top soft bottom microfluidic devices for cell culture and chemical analysis. Analytical Chemistry, 81(10):3714–3722, 2009.

[162] S. Min, K. Ahn, and J. Kim. Patterned fluorescence images using a photocleavable nvoc-protected quinizarin. Bulletin - Korean Chemical Society, 26(9):1437, 2005.

[163] G. Moad and D. H. Solomon. The chemistry of radical polymerization. Elsevier, 2005.

[164] M. J. Moorcroft, W. R. Meuleman, S. G. Latham, T. J. Nicholls, R. D. Egeland, and E. M. Southern. In situ oligonucleotide synthesis on poly (dimethylsiloxane): a flexible substrate for microarray fabrication. Nucleic acids research, 33(8):e75–e75, 2005.

[165] V. Moreau, Y. Renotte, and Y. Lion. Characterization of dupont photopolymer: determination of kinetic parameters in a diffusion model. Applied optics, 41(17):3427–3435, 2002.

[166] N. Moszner, U. Salz, and J. Zimmermann. Chemical aspects of self-etching enamel–dentin adhesives: a systematic review. Dental Materials, 21(10):895–910, 2005.

[167] N. Murphy-DuBay, L. Wang, E. C. Kinzel, S. Uppuluri, and X. Xu. Nanopatterning using nsom probes integrated with high transmission nanoscale bowtie aperture. Optics express, 16(4):2584–2589, 2008.

[168] D. C. Neckers, A. V. Fedorov, and A. A. Ermoshkin. Remote curing of polymer coating by gaseous, vaporous or aerosol initiating agent. US Patent Application US7682663 B2, 2010.

[169] O. D. Negrete and F. Cerrina. Step-and-scan maskless lithography for ultra large scale dna chips. Microelectronic Engineering, 85(5):834–837, 2008.

[170] P. G. Nelson. An analysis of scattered light in reflecting and refracting primary objectives for coronagraphs. Coronal Solar Magnetism Observatory Technical Note, 4, 2006.

[171] P. Neogi. Anomalous diffusion of vapors through solid polymers. part ii: Anomalous sorption. AIChE journal, 29(5):833–839, 1983.

[172] M. G. Neumann, W. G. Miranda Jr, C. C. Schmitt, F. A. Rueggeberg, and I. C. Correa. Molar extinction coefficients and the photon absorption efficiency of dental photoinitiators and light curing units. Journal of dentistry, 33(6):525–532, 2005.

[173] P. J. Nichols and M. W. Grant. Thermal-dissociation of thiuram disulfides in solution - an electron-spin resonance and kinetic-study. Australian Journal of Chemistry, 36(7):1379–1386, 1983.

[174] E. Niki and Y. Kamiya. Cage reactions of tert-butoxy radicals. effects of solvent and viscosity. Journal of the American Chemical Society, 96(7):2129–2133, 1974.

[175] A. North and G. Reed. Diffusion-controlled termination during the initial stages of free radical polymerization of methyl methacrylate. Transactions of the Faraday Society, 57:859–870, 1961.

[176] A. B. Oelkers, L. F. Scatena, and D. R. Tyler. Femtosecond pump-probe transient absorption study of the photolysis of [cp'mo (co) 3] 2 (cp'= 5-c5h4ch3): Role of translational and rotational diffusion in the radical cage effect. The Journal of Physical Chemistry A, 111(25):5353–5360, 2007.

[177] M. Ohring. Materials science of thin films. Academic press, 2001.

[178] S. Orlic, E. Dietz, T. Feid, S. Frohmann, and C. Mueller. Optical investigation of photopolymer systems for microholographic storage. J. Optics A, 11(2), 2009.

[179] A. Oron, S. H. Davis, and S. G. Bankoff. Long-scale evolution of thin liquid films. Reviews of modern physics, 69(3):931, 1997.

[180] A. Osborne and G. Porter. Diffusion studies in viscous media. Proceedings of the Royal Society of London. Series A. Mathematical and Physical Sciences, 284(1396):9–16, 1965.

[181] T. Otsu, A. Matsumoto, and T. Tazaki. Radical polymerization of methyl methacrylate with some 1, 2-disubstituted tetraphenylethanes as thermal iniferters. Polymer Bulletin, 17(4):323–330, 1987.

[182] C. Padilla, F. Magaa-Sandoval, E. Muniz, J. R. Smith, P. Fritschel, and L. Zhang. Low scatter and ultra-low reflectivity measured in a fused silica window. arXiv preprint arXiv:1312.1569, 2013.

[183] L. Pan, Y. Park, Y. Xiong, E. Ulin-Avila, Y. Wang, L. Zeng, S. M. Xiong, J. Rho, C. Sun, D. B. Bogy, and X. Zhang. Maskless plasmonic lithography at 22 nm resolution. Scientific Reports, 1, 2011.

[184] A. Patchornik, B. Amit, and R. Woodward. Photosensitive protecting groups. Journal of the American Chemical Society, 92(21):6333–6335, 1970.

[185] K. A. Patkar, W. E. Highsmith, and J. V. Aldrich. Solid phase and solution synthesis of nvoclys (co (ch2) 5nhnbd) och2cn, a trifunctional fluorescent lysine derivative. Amino acids, 36(2):203–207, 2009.

[186] R. F. Pease and S. Y. Chou. Lithography and other patterning techniques for future electronics. Proceedings of the IEEE, 96(2):248–270, 2008.

[187] A. P. Pelliccioli and J. Wirz. Photoremovable protecting groups: reaction mechanisms and applications. Photochemical & Photobiological Sciences, 1(7):441–458, 2002.

[188] F. Pfeiffer. Development of Molecular Glasses for Solvent-Free Photolithography utilizing Combinatorial Vapor Deposition. PhD thesis, Universitt Bayreuth, 2007.

[189] J. Piehler, A. Brecht, R. Valiokas, B. Liedberg, and G. Gauglitz. A high-density poly (ethylene glycol) polymer brush for immobilization on glass-type surfaces. Biosensors and Bioelectronics, 15(9):473–481, 2000.

[190] R. Piestun, Y. Y. Schechner, and J. Shamir. Propagation-invariant wave fields with finite energy. JOSA A, 17(2):294–303, 2000.

[191] V. Plyusnin, E. Kuznetzova, G. Bogdanchikov, V. Grivin, V. Kirichenko, and S. Larionov. Dithiocarbamate radicals in laser flash photolysis of thiuram disulphide and dithiocarbamate anion: calculation of optical spectra. Journal of Photochemistry and Photobiology A: Chemistry, 68(3):299–308, 1992.

[192] S. Quabis, R. Dorn, M. Eberler, O. Glckl, and G. Leuchs. Focusing light to a tighter spot. Optics Communications, 179(1):1–7, 2000.

[193] D. Rehm and A. Weller. Kinetics of fluorescence quenching by electron and h-atom transfer. Israel Journal of Chemistry, 8(2):259–271, 1970.

[194] E. Rittweger, K. Y. Han, S. E. Irvine, C. Eggeling, and S. W. Hell. Sted microscopy reveals crystal colour centres with nanometric resolution. Nature Photonics, 3(3):144–147, 2009.

[195] J. Robertus, W. R. Browne, and B. L. Feringa. Dynamic control over cell adhesive properties using molecular-based surface engineering strategies. Chemical Society Reviews, 39(1):354–378, 2010.

[196] P. Roy, Z. Rajfur, D. Jones, G. Marriott, L. Loew, and K. Jacobson. Local photorelease of caged thymosin 4 in locomoting keratocytes causes cell turning. The Journal of cell biology, 153(5):1035–1048, 2001.

[197] V. K. Rusiecki and S. A. Warne. Synthesis of nvoc-lysine and use in the preparation of selectively functionalized peptides. Bioorganic & Medicinal Chemistry Letters, 3(4):707–710, 1993.

[198] San Esters Inc. Industrial and specialty monomers guide. Electronic resource, retrieved from http://www.sanesters.com, 2014.

[199] Sartomer (Arkema Inc.). Product info sheet, sr348. Electronic resource, retrieved from http://americas.sartomer.com, 2014.

[200] K.-H. Schuster. Objective with crystal lenses and projection exposure equipment for microlithography. US Patent Application US7682663 B2.

[201] T. F. Scott, C. J. Kloxin, D. L. Forman, R. R. McLeod, and C. N. Bowman. Principles of voxel refinement in optical direct write lithography. Journal of Materials Chemistry, 21(37):14150–14155, 2011.

[202] T. F. Scott, B. A. Kowalski, A. C. Sullivan, C. N. Bowman, and R. R. McLeod. Two-color single-photon photoinitiation and photoinhibition for subdiffraction photolithography. Science, 324(5929):913–917, 2009.

[203] O. Seitz, M. M. Chehimi, E. Cabet-Deliry, S. Truong, N. Felidj, C. Perruchot, S. J. Greaves, and J. F. Watts. Preparation and characterisation of gold nanoparticle assemblies on silanised glass plates. Colloids and Surfaces A: Physicochemical and Engineering Aspects, 218(1):225–239, 2003.

[204] W. Shim, A. B. Braunschweig, X. Liao, J. N. Chai, J. K. Lim, G. F. Zheng, and C. A. Mirkin. Hard-tip, soft-spring lithography. Nature, pages 516–521, 2011.

[205] A. N. Shipway, E. Katz, and I. Willner. Nanoparticle arrays on surfaces for electronic, optical, and sensor applications. ChemPhysChem, 1(1):18–52, 2000.

[206] A. Singh, A. R. Scott, and Sopchysh.F. Flash photolysis of camphorquinone and biacetyl. Journal of Physical Chemistry, 73(8):2633, 1969.

[207] S. Singh-Gasson, R. D. Green, Y. Yue, C. Nelson, F. Blattner, M. R. Sussman, and F. Cerrina. Maskless fabrication of light-directed oligonucleotide microarrays using a digital micromirror array. Nature biotechnology, 17(10):974–978, 1999.

[208] G. S. Smith, C. B. Skidmore, P. M. Howe, and J. Majewski. Diffusion, evaporation, and surface enrichment of a plasticizing additive in an annealed polymer thin film. Journal of Polymer Science Part B: Polymer Physics, 42(17):3258–3266, 2004.

[209] M. v. Smoluchowski. Versuch einer mathematischen theorie der koagulationskinetik kolloider losungen. Z. phys. Chem, 92:129–168, 1917.

[210] M. S. Soh and A. U. J. Yap. Influence of curing modes on crosslink density in polymer structures. Journal of Dentistry, 32(4):321–326, 2004.

[211] C. M. Sparrow. On spectroscopic resolving power. The Astrophysical Journal, 44:76, 1916.

[212] R. Steudel, Y. Steudel, A. M. Mak, and M. W. Wong. Homolytic dissociation of the vulcanization accelerator tetramethylthiuram disulfide (tmtd) and structures and stabilities of the related radicals me2ncsn center dot (n=1-4). Journal of Organic Chemistry, 71(25):9302–9311, 2006.

[213] M. P. Stocker and J. T. Fourkas. Elucidating the kinetics and mechanism of rapid lithography. In SPIE MOEMS-MEMS, pages 824902–824902–7. International Society for Optics and Photonics, 2012.

[214] H.-B. Sun and S. Kawata. Two-photon photopolymerization and 3D lithographic microfabrication, pages 169–273. Springer, 2004.

[215] H. B. Sun, K. Takada, M. S. Kim, K. S. Lee, and S. Kawata. Scaling laws of voxels in two-photon photopolymerization nanofabrication. Applied Physics Letters, 83(6):1104–1106, 2003.

[216] L. Sun, R. M. Crooks, and V. Chechik. Preparation of polycyclodextrin hollow spheres by templating gold nanoparticles. Chemical Communications, (4):359–360, 2001.

[217] K. Tharanikkarasu and G. Radhakrishnan. Tetraphenylethane iniferters: Polyurethane-polystyrene multiblock copolymers through living radical polymerization. Journal of applied polymer science, 66(8):1551–1560, 1997.

[218] P. Torok and P. Munro. The use of gauss-laguerre vector beams in sted microscopy. Optics Express, 12(15):3605–3617, 2004.

[219] C. P. Toumey. Reading feynman into nanotechnology. Techn: Research in Philosophy and Technology, 12(3):133–168, 2008.

[220] I. Trenkmann, D. Tuber, M. Bauer, J. Schuster, S. Bok, S. Gangopadhyay, and C. von Borczyskowski. Investigations of solid liquid interfaces in ultra-thin liquid films via single particle tracking of silica particles. diffusion-fundamentals.org, 11:1–12, 2009.

[221] H. Truckenbrodt, A. Duparre, and U. Schuhmann. Roughness and defect characterization of optical surfaces by light-scattering measurements. In Optical Systems Design'92, pages 139–151. International Society for Optics and Photonics, 1992.

[222] J. Tsao and D. Ehrlich. Uv laser photopolymerization of volatile surface-adsorbed methyl methacrylate. Applied Physics Letters, 42(12):997–999, 1983.

[223] S. Tzeng, K. Lin, J.-C. Hu, L. Chen, and S. Gwo. Templated self-assembly of colloidal nanoparticles controlled by electrostatic nanopatterning on a si3n4/sio2/si electret. Advanced Materials, 18(9):1147–1151, 2006.

[224] C. Van Kerckhoven, H. Van den Broeck, G. Smets, and J. Huybrechts. Dithiocarbamate telechelic polymers: Synthesis and block copolymerization. Die Makromolekulare Chemie, 192(1):101–114, 1991.

[225] T. Vossmeyer, S. Jia, E. DeIonno, M. Diehl, S.-H. Kim, X. Peng, A. Alivisatos, and J. Heath. Combinatorial approaches toward patterning nanocrystals. Journal of Applied Physics, 84(7):3664–3670, 1998.

[226] J. Vrentas and J. Duda. Diffusion in polymersolvent systems. ii. a predictive theory for the dependence of diffusion coefficients on temperature, concentration, and molecular weight. Journal of Polymer Science: Polymer Physics Edition, 15(3):417–439, 1977.

[227] J. Vrentas and J. Duda. Molecular diffusion in polymer solutions. AIChE Journal, 25(1):1–24, 1979.

[228] J. Vrentas, J. Duda, and A. Hou. Anomalous sorption in poly(ethylmethacrylate). Journal of applied polymer science, 29(1):399–406, 1984.

[229] J. Vrentas, C. Jarzebski, and J. Duda. A deborah number for diffusion in polymer solvent systems. AIChE Journal, 21(5):894–901, 1975.

[230] P. J. Wagner and I. Kochevar. Triplet energy transfer. iii. how efficient is diffusion-controlled triplet energy transfer. Journal of the American Chemical Society, 90(9):2232–2238, 1968.

[231] S. Waichman, M. Bhagawati, Y. Podoplelova, A. Reichel, A. Brunk, D. Paterok, and J. Piehler. Functional immobilization and patterning of proteins by an enzymatic transfer reaction. Analytical chemistry, 82(4):1478–1485, 2010.

[232] Y. Wei and R. L. Brainard. Advanced processes for 193-nm immersion lithography. In SPIE Advanced Lithography. SPIE Bellingham, Washington, 2009.

[233] M. H. Werts, M. Lambert, J.-P. Bourgoin, and M. Brust. Nanometer scale patterning of langmuir-blodgett films of gold nanoparticles by electron beam lithography. Nano Letters, 2(1):43–47, 2002.

[234] B. Williamson and V. K. L. Mer. The kinetics of activationdiffusion controlled reactions in solution. the temperature dependence of the quenching of fluorescence1, 2. Journal of the American Chemical Society, 70(2):717–721, 1948.

[235] K. I. Willig, S. O. Rizzoli, V. Westphal, R. Jahn, and S. W. Hell. Sted microscopy reveals that synaptotagmin remains clustered after synaptic vesicle exocytosis. Nature, 440(7086):935–939, 2006.

[236] T. J. A. Wolf, J. Fischer, M. Wegener, and A. N. Unterreiner. Pump-probe spectroscopy on photoinitiators for stimulated-emission-depletion optical lithography. Optics Letters, 36(16):3188–3190, 2011.

[237] D. Woll, S. Walbert, K. Stengele, T. J. Albert, T. Richmond, J. Norton, M. Singer, R. D. Green, W. Pfleiderer, and U. E. Steiner. Triplet-sensitized photodeprotection of oligonucleotides in solution and on microarray chips. Helvetica chimica acta, 87(1):28–45, 2004.

[238] D. Woll, S. Walbert, K.-P. Stengele, R. Green, T. Albert, W. Pfleiderer, and U. Steiner. More efficient photolithographic synthesis of dna-chips by photosensitization. Nucleosides, Nucleotides and Nucleic Acids, 22(5-8):1395–1398, 2003.

[239] G. Wypych. Handbook of plasticizers. ChemTec Publishing, 2004.

[240] L. Xue and Y. Han. Inhibition of dewetting of thin polymer films. Progress in Materials Science, 57(6):947–979, 2012.

[241] Z. Yang, W. Frey, T. Oliver, and A. Chilkoti. Light-activated affinity micropatterning of proteins on self-assembled monolayers on gold. Langmuir, 16(4):1751–1758, 2000.

[242] R. Yerushalmirozen, J. Klein, and L. J. Fetters. Suppression of rupture in thin, nonwetting liquid-films. Science, 263(5148):793–795, 1994.

[243] Y. Yi, M. J. Farrow, E. Korblova, D. M. Walba, and T. E. Furtak. High-sensitivity aminoazobenzene chemisorbed monolayers for photoalignment of liquid crystals. Langmuir, 25(2):997–1003, 2008.

[244] H. Zhou and S. F. Bent. Molecular layer deposition of functional thin films for advanced lithographic patterning. ACS Applied Materials & Interfaces, 3(2):505–511, 2011.

[245] M. Zhu, M. Z. Lerum, and W. Chen. How to prepare reproducible, homogeneous, and hydrolytically stable aminosilane-derived layers on silica. Langmuir, 28(1):416–423, 2011.

[246] T. Zhu, X. Fu, T. Mu, J. Wang, and Z. Liu. ph-dependent adsorption of gold nanoparticles on p-aminothiophenol-modified gold substrates. Langmuir, 15(16):5197–5199, 1999.

[247] H. Ziani-Cherif, Y. Abe, K. Imachi, and T. Matsuda. Visible-light-induced surface graft polymerization via camphorquinone impregnation technique. Journal of Biomedical Materials Research, 59(2):386–389, 2002.